Theory and Computational Method for the Stability Analysis of External MHD Modes in Toroidal Plasmas

Nobuyuki Aiba

DOCTOR OF PHILOSOPHY

Department of Fusion Science School of Physical Sciences
The Graduate University for Advanced Studies

2004 (School Year)

Abstract

The theory and analytical model for the stability analysis of magnetohydrodynamic (MHD) modes based on the two-dimensional Newcomb equation are extended for the analysis of external MHD modes both with low-n and with high-n toroidal mode numbers. In this model, since the appropriate weight function and the boundary conditions at rational surfaces are introduced to solve the eigenvalue problem associated with the Newcomb equation, the spectrum of this eigenvalue problem contains only discrete eigenvalues. This feature enables us to reveal explicitly whether plasma is stable or unstable.

In this dissertation, the analytical model is first applied to the development of a new method that analyzes the stability of a low-n external MHD mode in a matrix form, and hence this new method is called the stability matrix method. A numerical code (MARG2D-SM) is developed according to the stability matrix method, and the validity of the code is confirmed by several benchmark tests. The code clarifies the spectral structure of $n = 1$ ideal external kink modes, which are stable or unstable. The spectral gaps induced by the poloidal coupling are also investigated. The stability matrix method reveals the effect of stable ideal internal modes (fixed boundary modes) on the stability of ideal external modes (free boundary modes). With this effect, the mode structure of an ideal external mode changes from a surface mode structure to a global mode structure as a beta value increases, and an external mode destabilizes when an internal mode approaches to their marginal stability; a beta value is a ratio of the plasma pressure to the magnetic pressure. This effect explains how a safety factor profile in the core region of high beta tokamak plasma affects the stability of an ideal external mode.

The model based on the Newcomb equation has an advantage that the marginal stability can be identified with a short computation time. Such an advantage is demonstrated to be powerful in the study on the aspect ratio dependence of the $n = 1$ ideal external MHD mode stability.

For high-n external MHD modes, the analytical method based on the Newcomb equation is extended in the vacuum region; the vacuum energy integral is calculated by using the vector potential method. The MARG2D code, which solves numerically the eigenvalue problem associated with the two-dimensional Newcomb equation, is adapted to this new model, and

the validity of this extension is confirmed by benchmark tests. This extended MARG2D code is developed as a parallel computing code, and enables the fast stability analysis of high-n modes like a peeling mode, an edge ballooning mode, and a couple of them called a peeling-ballooning mode.

Acknowledgment

First of all, I would like to express my sincerest gratitude to Dr. Shinji Tokuda in Japan Atomic Energy Research Institute (JAERI). He inspired me to the field of the plasma physics, particularly the magnetohydrodynamic theory, and introduced beauties of the mathematical physics and the computational physics. During graduate course, he has supervised my doctoral research. Without his appropriate guidance, I have never achieved this thesis.

I would like to thank Prof. Masao Okamoto in Graduate University for Advanced Studies (Grad. Univ. for Advanced Studies) and National Institute for Fusion Science (NIFS). He accepted me to transfer from Kyoto University to his laboratory. He has given me a freedom to continue this work and encouraged me during my doctoral program.

I express my appreciation to Dr. Masaru Furukawa in University of Tokyo for fruitful discussions. I have learned a lot of things, including the plasma physics and the attitude toward research.

I am grateful to Dr. Yasuhiro Idomura in JAERI. He has provided me an opportunity to discuss with researchers in JAERI, which is helpful to achieve this work. He has encouraged me to improve this thesis.

I am also grateful to Dr. Shinsuke Satake in NIFS. He gave me some advices when I transfered to Grad. Univ. for Advanced Studies, and has encouraged me during my doctoral program.

In 2001,2002 and 2004, I stayed at Naka Fusion Research Establishment, JAERI. It was a great experience for me, and most of the present work were accomplished during these stays. I thank to Dr. Yasuaki Kishimoto, Dr. Takashi Tsuda, Dr. Yasutomo Ishii, Dr. Taro Matsumoto, Dr. Naoaki Miyato, Dr. Yasuhiro Kagei, and other members in Department of Fusion Plasma Research for helpful discussions and suggestions. I also thank to Dr. Akio Kitsunezaki, Dr. Hiromasa Ninomiya, and Dr. Mitsuru Kikuchi for giving me an opportunity to study at JAERI.

To Prof. Noriyoshi Nakajima, Prof. Yasushi Todo, Prof. Katsuji Ichiguchi, Prof. Hideo Sugama, Prof. Tomohiko Watanabe, Dr. Akihiro Ishizawa in NIFS, and Dr. Ming S. Chu in General Atomic (GA, U.S.A.), I owe appreciation for useful comments and suggestions.

I have been supported by the intern program of JAERI in 2001, 2002, and 2004, and the

scholarship students from fusion science association of Grad. Univ. for Advanced Studies in 2003.

I am deeply grateful to all the members at Graduate School of Energy Science and Institute of Advanced Energy in Kyoto University, those at Naka Fusion Research Establishment, JAERI, those in NIFS, and those at school of physical science in Grad. Univ. for Advanced Studies.

I am profoundly grateful to my parents, especially to my father raising me alone during my long term studies.

Finally, I would like to express my deep gratitude to the late Prof. Masahiro Wakatani in Kyoto University. He accepted me to his laboratory in my master's and doctoral programs, and led me to the kingdom of theoretical plasma physics. Needless to say, he was a professor learned, especially in the plasma physics and the fusion technology, and he had an enthusiasm for realizing a fusion reactor. His enthusiasm has encouraged me to complete this dissertation, and will support me for all my life. I pray sincerely for the repose of his soul.

Contents

Chapter 1

Introduction

Controlled thermonuclear fusion is expected to be a new and inexhaustible energy resource in this 21-st century. Now the most promising approach to the fusion reactor is the magnetic confinement of a high temperature plasma. A device of the magnetic confinement must be a shape of torus, and various types of toroidal devices have been proposed [1]. The device closest to a reactor among them is tokamak, first developed in the then U.S.S.R. [2]; for example, in JT-60U the equivalent fusion multiplication factor Q has reached to 1.25 [3], where Q is defined as the ratio of fusion output power to input power for plasma heating, and an international project is ongoing for constructing the ITER (International Thermonuclear Experimental Reactor) among Japan, EU, USA, Russia, and other countries [4].

For a fusion reactor to be attractive from the economical point of view, a tokamak has to be able to confine a high temperature, high β plasma with enough long confinement time. Here β is a ratio of the plasma pressure to the magnetic pressure. For establishment of such a stationary high performance operation, there are several key issues to be resolved. One of them is the stability against external magnetohydrodynamic (MHD) perturbations both with low-n and with high-n toroidal mode number.

The low-n ideal external MHD modes, obstacles limiting the tokamak performance, are stabilized by a conducting wall as long as the wall be an ideal conductor. However, the modes can remain still unstable due to the finite resistivity of the wall; such modes are called resistive wall modes (RWMs) [5]. Since RWMs restrict the stationary operation, they are to be stabilized or to be controlled by other methods than the conducting wall. An effective stabilization mechanism is plasma rotation relative to the wall. However, the ration frequency necessary for the stabilization is the Alfvén or the sound transit frequency [6–9], and hence such rotation frequency is not expected in a reactor such as ITER. Another effective method is a feedback control with external coils, which is considered as technologically feasible [10–15]. A numerical method of the feedback stabilization has been reported [13], which involves using both a MHD stability code DCON [16] and the vacuum field code VACUUM code [17].

High-n external modes (a peeling mode [18], an edge-ballooning mode [19], and a mode with the combined structure of the peeling and the ballooning modes) are the trigger for edge localized modes (ELMs) that constrain the maximum achievable pressure gradients in the pedestal at the tokamak edge region; high pressure gradients in the pedestal is a crucial element for the high performance (so called H-mode [20]) operation. Numerical analysis on the stability of high-n external modes have been reported based on the single ideal MHD model with the large-n ordering model [21–23] or on a full MHD model [24,25]. Such analyses claim that high-n external modes explain various ELM phenomena in H-mode [20] tokamak operations. Also, an integrated modeling between the core and pedestal regions is reported, which uses a predictive core transport model and a pedestal model that includes MHD stability analysis of high-n external modes [26].

Another promising approach to the MHD stability analysis for these external MHD modes will be the Newcomb equation, which is the inertia free linear ideal magnetohydrodynamic (MHD) equation [27, 28]. However, the Newcomb equation has regular singular points at rational surfaces that satisfy the resonance condition $m = nq(r)$, where m is the poloidal mode number, $q(r)$ is the safety factor, and r is a poloidal flux label of the MHD equilibrium. This singular nature of the equation can yield continuous spectra in the stable region, and makes it difficult to solve the equation numerically. Tokuda and Watanabe [29] have resolved such difficulties by formulating a new eigenvalue problem associated with the two-dimensional Newcomb equation for internal MHD modes; the proposed eigenvalue problem has only real and denumerable eigenvalues without continuous spectra. At the same time, according to this formulation, a code MARG2D has been developed which solves numerically the two-dimensional Newcomb equation and the associated eigenvalue problem by a finite element method [30].

Although the formulation in Ref. [29] is limited to internal MHD modes, we can expect that the MARG2D formulation also provides a powerful tool for the stability analysis of low-n and high-n external MHD modes. The main purpose of this thesis is to develop an analytical model and a numerical code for stability analysis of a broad n range of external MHD modes in toroidal plasmas, especially in a shaped axisymmetric toroidal plasma by extending the theory of the Newcomb equation to external modes. The code thus developed is also enough fast to be used practically in the stability control as well as transport simulations.

Chapter 2 briefly reviews the ideal MHD model, static MHD equilibrium in an axisymmetric system, and the Energy Principle for the linear ideal MHD stability analysis. Chapter 3 introduces the two-dimensional Newcomb equation and the associated eigenvalue problem, and describes the MARG2D stability code; these are the basis of this dissertation.

When I extend the theory of the Newcomb equation to external mode analyses, I take different approaches for a low-n mode and a high-n mode.

For low-n external mode analysis, I develop in Chapter 3 a matrix method that expresses

the change of the potential energy due to the plasma displacement by a quadratic form with respect to the values of the displacement at the plasma surface [10, 31]. According to this method, a code MARG2D-SM is developed. The code provides a tool essential for the RWM analysis, which is second to, but alternative to the DCON code. Moreover, if this matrix method is combined with the eigenvalue problem associated with the Newcomb equation derived in Chapter 3, we can get deeper insight into the spectral properties of external modes. In Chapter 4, after benchmark tests between the MARG2D-SM code and the conventional stability analysis code (ERATO) [32], I investigate the spectral structure of $n = 1$, stable or unstable, ideal external kink modes, and the property of the spectral gaps induced by the poloidal coupling originated from the finite aspect ratio effect. Although toroidal effects on the spectral gaps were analytically predicted in Ref. [33], this thesis numerically confirms these predictions. Furthermore I investigate, analytically and numerically, the destabilizing effect of stable internal MHD modes on the stability and the mode structure of external MHD modes when internal modes approach to their marginal stability. This effect of the stable internal modes clarifies the difference between the external mode stability in a normal shear tokamak and that in a reversed shear tokamak. The stability of ideal external modes is further investigated from the view point of the aspect ratio dependence, which gets attention in the research on small aspect ratio tokamak [34].

For high-n external mode analysis I adopt in Chapter 5, the vector potential method [35] in order to write the vacuum magnetic field contribution (vacuum energy integral) in the same integral form as the plasma contribution. Consequently, we can apply the MARG2D formulation directly to the vacuum energy integral and can analytically reduce the potential energy for a high-n external MHD mode without using the large n ordering. This extension therefore realizes a broad n range of external mode analysis on the basis of the single physical model.

The eigenvalues computed by the MARG2D code correspond neither to growth rates nor frequencies of MHD perturbations. However, the sign of the minimum eigenvalue tells us whether an MHD equilibrium is stable or unstable against ideal MHD perturbations since the eigenvalue problem solved by MARG2D does not contain continuous spectra. This property is especially useful when we have to analyze the stability of a series of equilibria generated from the time evolution of a discharge, either by an experiment or by a transport simulation, since we are mainly interested in whether each equilibrium is stable or unstable. To facilitate such stability analysis I adapt MARG2D for parallel computing by using the message passing interface (MPI) [36] and the ScaLAPACK library [37]. And also we study in Chapter 5 the performance of this code, discussing the possibility of the stability analysis between the interval of experiments, and the possibility of the real-time stability analysis by using a future, advanced parallel computer.

Finally, I summarize in Chapter 6 the achievements in this thesis, discussing the outlook

for further developments and applications to analyze and to control external MHD modes in a toroidal plasma.

Chapter 2

Ideal MHD model

2.1 Ideal MHD equations

We first introduce the single-fluid, ideal magnethydrodynamic (MHD) equations. In the kinetic theory, the behavior of the plasma composed of N particles is described by the Klimontovich equation [38] coupled with Maxwell's equations [39]. However, we are usually not interested in the exact motion of all of the particles in a plasma, but rather in certain average or approximate characteristics. We adopt the distribution function of the species s, $f_s(\boldsymbol{x}, \boldsymbol{v}, t)$, as the ensemble averaged number of point particles per unit six-dimensional phase space; $\boldsymbol{x}$ is the three-dimensional configuration space, $\boldsymbol{v}$ is the three-dimensional velocity space, and t is the time. By using f_s, the Vlasov equation arises naturally from the Klimontovich equation when the effects of collisions are ignored as [40, 41]

$$\frac{\partial f_s(\boldsymbol{x}, \boldsymbol{v}, t)}{\partial t} + \boldsymbol{v} \cdot \nabla_{\boldsymbol{x}} f_s + \frac{q_s}{m_s} (\boldsymbol{E} + \boldsymbol{v} \times \boldsymbol{B}) \cdot \nabla_{\boldsymbol{v}} f_s = 0, \tag{2.1}$$

where q_s and m_s are the charge and the mass of a particle of species s, $\boldsymbol{E}$ and $\boldsymbol{B}$ are the electric and the magnetic fields, respectively.

By taking velocity moments of Eq. (2.1) in seven-dimensional $(\boldsymbol{x}, \boldsymbol{v}, t)$ space, an infinite hierarchy of equations in four-dimensional $(\boldsymbol{x}, t)$ space can be derived. The standard two-fluid theory of plasma physics is obtained by truncating this infinite hierarchy with the assumption that f_s is nearly local Maxwellian. The single fluid, ideal MHD equations are derived

from the two-fluid equation as [41, 42]

$$\frac{\partial \rho}{\partial t} + \nabla \cdot (\rho \boldsymbol{v}) = 0, \tag{2.2}$$

$$m_i n \frac{\mathrm{D}\boldsymbol{v}}{\mathrm{D}t} = \boldsymbol{J} \times \boldsymbol{B} - \nabla p, \tag{2.3}$$

$$\boldsymbol{E} + \boldsymbol{v} \times \boldsymbol{B} = 0, \tag{2.4}$$

$$\frac{\mathrm{D}p}{\mathrm{D}t} = -\Gamma p \nabla \cdot \boldsymbol{v}, \tag{2.5}$$

$$\frac{\partial \boldsymbol{B}}{\partial t} = -\nabla \times \boldsymbol{E}, \tag{2.6}$$

$$\nabla \times \boldsymbol{B} = \mu_0 \boldsymbol{J}, \tag{2.7}$$

$$\nabla \cdot \boldsymbol{B} = 0, \tag{2.8}$$

with the assumptions (i) high collisionality, (ii) characteristic dimensions much larger than an ion gyro radius, (iii) characteristic frequency is much smaller than the ion gyro frequency, and (iv) small resistivity. Here, $\mathrm{D}/\mathrm{D}t = \partial/\partial t + \boldsymbol{v} \cdot \nabla$, ρ and p are the density and the pressure of a plasma, m_i is the mass of an ion, $\boldsymbol{v}$ is the fluid velocity, $\boldsymbol{J}$ is the current density, and μ_0 is the vacuum permeability.

For plasmas of fusion interest, the conditions of small gyro radius and small resistivity are well satisfied, and the low frequency condition is valid when we treat such MHD motions. However, the high collisionality assumption is never satisfied. Despite this break, empirical evidence demonstrating that ideal MHD provides a very accurate description of most macroscopic plasma behavior. Therefore, the ideal MHD model is used in this thesis to study equilibrium and stability properties of tokamaks.

2.2 MHD equilibrium

In this section, we derive the equilibrium equations, called Grad-Shafranov equation [43–45]. The basic equations of the ideal MHD equilibrium with scalar pressure and without flow are

$$\nabla p = \boldsymbol{J} \times \boldsymbol{B}, \tag{2.9}$$

$$\nabla \times \boldsymbol{B} = \mu_0 \boldsymbol{J}, \tag{2.10}$$

$$\nabla \cdot \boldsymbol{B} = 0. \tag{2.11}$$

For an axisymmetric system such as a tokamak plasma, we can define the poloidal magnetic flux function ψ from the toroidal component of the vector potential A_ϕ as

$$\psi = -RA_\phi, \tag{2.12}$$

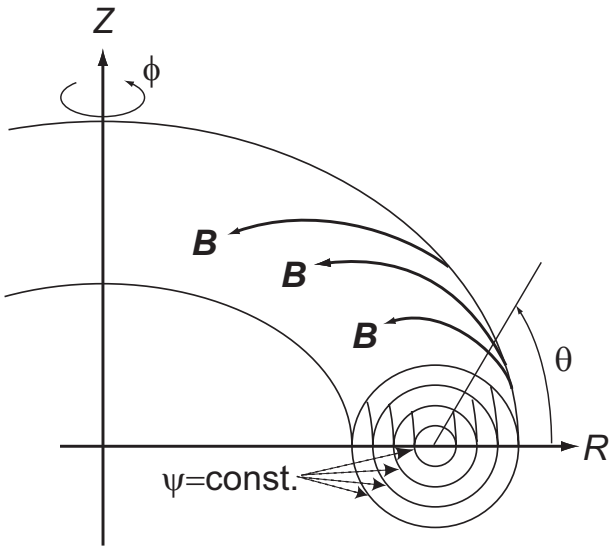

Figure 2.1: Cylindrical and flux coordinate systems.

where R and ϕ are the cylindrical coordinate system (R, ϕ, Z) as shown in Fig. 2.1. By using this scalar function ψ in (R, ϕ, Z), the magnetic field is represented by

$$\boldsymbol{B} = \nabla\phi \times \nabla\psi + F\nabla\phi. \tag{2.13}$$

Here F, called toroidal field function, is expressed by using the toroidal field B_t as

$$F = RB_t. \tag{2.14}$$

Then the set of the equilibrium equations, Eqs. (2.9)-(2.11), is reduced to a second-order partial differential equation, called Grad-Shafranov equation, as

$$\Delta^*\psi \equiv \frac{\partial^2\psi}{\partial R^2} - \frac{1}{R}\frac{\partial\psi}{\partial R} + \frac{\partial^2\psi}{\partial Z^2} = \mu_0 R J_\phi, \tag{2.15}$$

where the toroidal component of the plasma current J_ϕ is given by

$$J_\phi = -R\frac{dp}{d\psi} - \frac{1}{\mu_0}\frac{F}{R}\frac{dF}{d\psi}. \tag{2.16}$$

It is easily seen that the pressure function p and toroidal field function F are functions of only ψ. Since ψ has an ambiguity of a shift of a constant value, we define the ψ value at the plasma surface to be zero; the ψ value inside the surface is negative.

For tokamaks, a toroidal magnetic field is generated by a current in toroidal-field coils, and a poloidal magnetic field is made by a finite toroidal current inside the plasma region and by a current in poloidal-field coils. These magnetic field lines forms nested magnetic surfaces which coincide with the contours of ψ as shown in Fig. 2.1.

Plasma behaviors along the magnetic surfaces and across them are fairly different. Therefore, it is desirable to employ a flux coordinate system based on the contours of ψ to analyze properties of instabilities. In this thesis, we adopt a flux coordinate system (ψ, θ, ϕ), where ϕ is the toroidal angle same as that defined in a cylindrical coordinate system, and θ is an arbitrarily chosen poloidal angle as shown in Fig. 2.1. Because θ is the angular coordinate with modulus of 2π, the following constraint imposed to the Jacobian $\sqrt{g}$,

$$\oint \frac{dl}{\sqrt{g}B_p} = 2\pi, \tag{2.17}$$

where $\sqrt{g} = [(\nabla\psi \times \nabla\theta) \cdot \nabla\phi]^{-1}$ and dl is the line element.

The flux surface average $\langle X \rangle_f$ of a variable X is defined as

$$\langle X \rangle_f \equiv \lim_{\Delta V \to 0} \frac{1}{\Delta V} \int_{\Psi}^{\Psi+\Delta\Psi} X dV = 2\pi \int_0^{2\pi} \frac{X}{dV/d\Psi} \sqrt{g} d\theta = 2\pi \oint \frac{X/B_p}{dV/d\Psi} dl, \tag{2.18}$$

$$\frac{dV}{d\Psi} = 2\pi \int_0^{2\pi} \sqrt{g} d\theta = 2\pi \oint \frac{dl}{B_p}, \tag{2.19}$$

where $V(\Psi)$ is a volume inside a magnetic surface specified by an arbitrarily chosen label Ψ, such as, the poloidal magnetic flux $\psi \equiv \int \boldsymbol{B} \cdot \nabla\theta dV/(2\pi)^2$, the toroidal magnetic flux $\Lambda \equiv \int \boldsymbol{B} \cdot \nabla\phi dV/(2\pi)^2$, and so on. In this thesis, we adopt ψ as the magnetic surface label.

Next, we define several equilibrium quantities. For statistic axisymmetric equilibrium, the perpendicular component of the current is

$$\boldsymbol{J}_\perp = \frac{\boldsymbol{B} \times \nabla p}{B^2}, \tag{2.20}$$

where $\boldsymbol{J}$ is expressed as $\boldsymbol{J} = \boldsymbol{J}_\perp + J_\parallel \boldsymbol{B}/B$. From the quasi-neutral condition

$$\nabla \cdot \boldsymbol{J} = 0, \tag{2.21}$$

we get the relation as

$$\nabla \cdot \left(J_\parallel \frac{\boldsymbol{B}}{B} \right) = -\nabla \cdot \left(\frac{\boldsymbol{B} \times \nabla p}{B^2} \right). \tag{2.22}$$

After some manipulations, $J_\parallel$ is derived as

$$J_\parallel = -\frac{F}{B} \frac{dp}{d\psi} \left(1 - \frac{B^2}{\langle B^2 \rangle_f} \right) + \frac{\langle \boldsymbol{J} \cdot \boldsymbol{B} \rangle_f}{\langle B^2 \rangle_f} B. \tag{2.23}$$

The first term of this equation is the well-known Pfirsch-Schlüter current [46] which maintains the quasi-neutral condition. The divergence-free current of the second term assures the momentum balance along the magnetic lines of force and it is essential for confining the tokamak plasma. Within the framework of the neoclassical transport theory, the surface-average parallel current is expressed by

$$\langle \boldsymbol{J} \cdot \boldsymbol{B} \rangle = \langle \boldsymbol{J} \cdot \boldsymbol{B} \rangle_E + \langle \boldsymbol{J} \cdot \boldsymbol{B} \rangle_B + \langle \boldsymbol{J} \cdot \boldsymbol{B} \rangle_S, \tag{2.24}$$

where $\langle \boldsymbol{J} \cdot \boldsymbol{B} \rangle_E$, $\langle \boldsymbol{J} \cdot \boldsymbol{B} \rangle_B$ are the ohmic current and the bootstrap current given as

$$\langle \boldsymbol{J} \cdot \boldsymbol{B} \rangle_E = \sigma_{NC} \langle \boldsymbol{E} \cdot \boldsymbol{B} \rangle, \tag{2.25}$$

$$\langle \boldsymbol{J} \cdot \boldsymbol{B} \rangle_B = -F \left(L_{31}^e \frac{dp_e}{d\psi} + L_{31}^i \frac{dp_i}{d\psi} + L_{32}^e \frac{dT_e}{d\psi} + L_{32}^i \frac{dT_i}{d\psi} \right), \tag{2.26}$$

and $\langle \boldsymbol{J} \cdot \boldsymbol{B} \rangle_S$ expresses the non-ohmically driven current [47, 48]. The neoclassical transport coefficients, σ_{NC}, L_{31}^e, L_{31}^i, L_{32}^e, and L_{32}^i are given in neoclassical transport theory review papers [49, 50].

The MHD safety factor q, which assume the configurations of a set of nested toroidal flux surfaces, is defined as

$$q(V) \equiv \frac{d\psi/dV}{d\Lambda/dV}. \tag{2.27}$$

When a magnetic field line closes on itself by circulating m times in the poloidal direction and n times in the toroidal direction, the safety factor is represented as $q = n/m$. Such a magnetic surface is called a rational surface.

The magnetic shear is a quantity that measures the change in pitch angle of a magnetic field line from one flux surface to the next, and defined as [42]

$$s(V) \equiv 2 \frac{V}{q} \frac{dq}{dV}. \tag{2.28}$$

The geometrical quantities, the aspect ratio A, the ellipticity κ, and the triangularity δ, are defined as

$$A \equiv \frac{R_{maj}}{a}, \tag{2.29}$$

$$\kappa \equiv \frac{h}{a}, \tag{2.30}$$

$$\delta \equiv \frac{d}{a}. \tag{2.31}$$

Here R_{maj} is the major radius, a is the minor radius, h is the height, and d is the distance between major radius of the highest position from the plasma center, shown in Fig. 2.2.

Finally, we introduce several definitions of beta which is a ratio of the plasma pressure to the magnetic pressure. The toroidal beta β_t and the poloidal beta β_p are defined as

$$\beta_t \equiv \frac{2\mu_0 \langle\langle p \rangle\rangle}{B_{t0}^2}, \tag{2.32}$$

$$\beta_p \equiv \frac{2\mu_0 \langle\langle p \rangle\rangle}{B_{pa}^2}, \tag{2.33}$$

where B_{t0} is the vacuum magnetic field at the plasma center called the magnetic axis, B_{pa} is the average poloidal magnetic field at the plasma edge, defined as

$$B_{pa} \equiv \frac{\mu_0 I_p}{2\pi \langle a \rangle_f}, \tag{2.34}$$

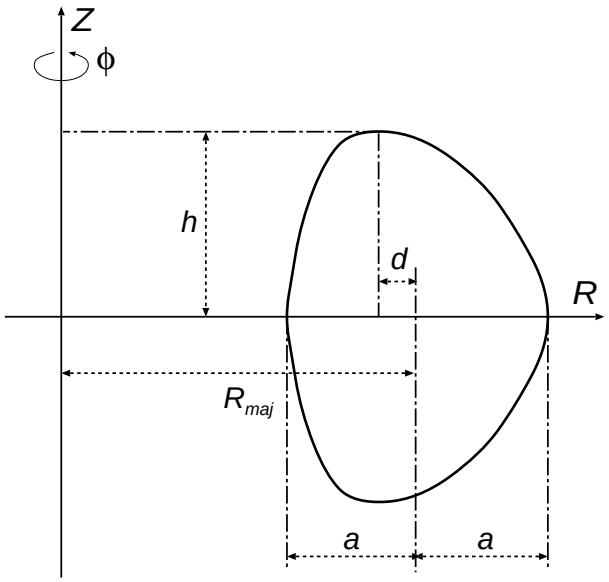

Figure 2.2: Lengths defined in a poloidal cross-section of a tokamak plasma.

and I_p is the toroidal current. The volume average of a variable$X$ $\langle\langle X\rangle\rangle$ is defined as

$$\langle\langle X\rangle\rangle \equiv \frac{\int X dV}{\int dV}. \tag{2.35}$$

The volume averages are taken over the whole volume of the plasma. In addition, the normalized betaβ_N is defined as

$$\beta_N \equiv 100\beta_t \cdot a \cdot \frac{B_t}{I_p/\mu_0 \cdot 10^6}, \tag{2.36}$$

which relates to Troyon scaling of critical beta in tokamaks [51].

2.3 Ideal MHD stability

In this section, we introduce the theory for analyzing the ideal linear MHD stability, called the Energy Principle [52]. We adopt a Lagrangian description of the fluid motion, and all quantities are now considered to be functions of the initial location of a fluid element$\boldsymbol{r}_0$, and of the time$t$. With the displacement vector$\boldsymbol{\xi}$ which is determined by

$$\boldsymbol{r} = \boldsymbol{r}_0 + \boldsymbol{\xi}, \tag{2.37}$$

where $\boldsymbol{r}$ is the location of the fluid element at time t, the linearized MHD equation takes the form

$$\rho_0 \frac{\partial^2 \boldsymbol{\xi}}{\partial t^2} = \boldsymbol{F}(\boldsymbol{\xi}), \tag{2.38}$$

$$\rho_1 = -\nabla \cdot (\rho_0 \boldsymbol{\xi}), \tag{2.39}$$

$$p_1 = -\boldsymbol{\xi} \cdot \nabla p_0 - \gamma p_0 \nabla \cdot \boldsymbol{\xi}, \tag{2.40}$$

$$\boldsymbol{B}_1 = \nabla \times (\boldsymbol{\xi} \times \boldsymbol{B}_0), \tag{2.41}$$

where the force operator

$$\boldsymbol{F}(\boldsymbol{\xi}) = \frac{1}{\mu_0} ((\nabla \times \boldsymbol{B}_0) \times \boldsymbol{Q} + (\nabla \times \boldsymbol{Q}) \times \boldsymbol{B}_0) + \nabla(\boldsymbol{\xi} \cdot \nabla p_0 + \gamma p_0 \nabla \cdot \boldsymbol{\xi}). \tag{2.42}$$

Here X_0 is the equilibrium value of X, X_1 is the perturbed value of X, and $\boldsymbol{Q}$ is the perturbation of $\boldsymbol{B}$ defined as $\boldsymbol{Q} = \boldsymbol{B}_1 \equiv \nabla \times (\boldsymbol{\xi} \times \boldsymbol{B}_0)$. Since the time does not appear explicitly in Eqs. (2.38)-(2.42), a general form of $\boldsymbol{\xi}$ can be written as

$$\boldsymbol{\xi}(\boldsymbol{r}_0, t) = \boldsymbol{\xi}(\boldsymbol{r}_0) \mathrm{e}^{\mathrm{i}\omega t}, \tag{2.43}$$

and the corresponding eigenvalue equation is

$$-\omega^2 \rho \boldsymbol{\xi} = \boldsymbol{F}(\boldsymbol{\xi}). \tag{2.44}$$

Equation (2.44) represents the normal mode formulation of the linearized MHD stability problem for general three-dimensional equilibria. In this approach, only appropriate boundary conditions on $\boldsymbol{\xi}$ are required. For example, when the plasma is surrounded by a conducting wall, the boundary condition is

$$\boldsymbol{n} \cdot \boldsymbol{\xi} = 0, \tag{2.45}$$

where $\boldsymbol{n}$ is the unit normal to the plasma surface.

The force operator $\boldsymbol{F}$ is a self-adjoint operator [42, 53, 54], and this self-adjointness has a major impact on both the analytic and the numerical formulation of linearized MHD stability. Then we demonstrate this property with two arbitrary vectors $\boldsymbol{\xi}$ and $\boldsymbol{\eta}$ satisfying appropriate boundary conditions in Appendix A.

Because of the self-adjointness of $\boldsymbol{F}$, the linearized ideal MHD stability problem can be easily cast in the form of a variational principle. The dot product of Eqs. (2.38) and (2.42) with $\boldsymbol{\xi}$ is formed and then integrated over the plasma volume, yielding

$$\omega^2 = \frac{\delta W(\boldsymbol{\xi}, \boldsymbol{\xi})}{K(\boldsymbol{\xi}, \boldsymbol{\xi})}, \tag{2.46}$$

where

$$\delta W(\boldsymbol{\xi}^*, \boldsymbol{\xi}) = -\frac{1}{2} \int \boldsymbol{\xi}^* \cdot \boldsymbol{F}(\boldsymbol{\xi}) d\boldsymbol{r}, \tag{2.47}$$

$$K(\boldsymbol{\xi}^*, \boldsymbol{\xi}) = \frac{1}{2} \int \rho |\boldsymbol{\xi}|^2 d\boldsymbol{r}. \tag{2.48}$$

The quantity δW represents the change of the potential energy associated with the perturbation and is equal to the work done against the force $\boldsymbol{F}(\xi)$ in displacing the plasma by an amount $\boldsymbol{\xi}$. The quantity K is proportional to the kinetic energy.

When we have a primary interest to determine the stability boundary of the given system, the variational formulation can be further simplified; the formulation is known as the Energy Principle [52]. The physical basis of this principle is the fact that energy is exactly conserved in the ideal MHD model. Since the extremum corresponding to the minimum eigenvalue of ω^2 actually represents a minimum in potential energy δW, the Energy Principle states that an equilibrium is stable if and only if

$$\delta W(\boldsymbol{\xi}^*, \boldsymbol{\xi}) \geq 0 \tag{2.49}$$

for all allowable displacements.

In general, a vacuum region surrounds a plasma, and δW is rewritten as the sum of three terms as

$$\delta W = \delta W_F + \delta W_S + \delta W_V, \tag{2.50}$$

where a volume integral δW_F extended over the fluid plasma domain, a surface integral δW_S extended over the fluid-vacuum interface, and a volume integral δW_V extended over the vacuum region. Here we assume that a plasma and a vacuum are surrounded by a perfect conducting wall. Before formulating these terms, we introduce the boundary condition at an interface between a plasma and a vacuum as

$$\left[\left[p + \frac{1}{2}B^2\right]\right]_a = 0, \tag{2.51}$$

$$\boldsymbol{n} \cdot [[\boldsymbol{v}]]_a = 0, \tag{2.52}$$

$$\boldsymbol{n} \times [[\boldsymbol{E}]]_a = 0, \tag{2.53}$$

$$\boldsymbol{n} \cdot [[\boldsymbol{B}]]_a = 0, \tag{2.54}$$

$$\boldsymbol{n} \times [[\boldsymbol{B}]]_a = \boldsymbol{J}_a, \tag{2.55}$$

where the subscript a means the value at the plasma boundary, and $[[X]]_a$ is the increment in any quantity X across the boundary in the direction $\boldsymbol{n}$. These boundary conditions are transcribed to first order $\boldsymbol{\xi}$ with the first-order vacuum vector potential $\acute{\boldsymbol{A}}$, where

$$\acute{\boldsymbol{E}} = -\frac{\partial \acute{\boldsymbol{A}}}{\partial t} + \acute{\boldsymbol{E}}_0, \quad \acute{\boldsymbol{B}} = \nabla \times \acute{\boldsymbol{A}} + \acute{\boldsymbol{B}}_0, \tag{2.56}$$

and vacuum quantities are distinguished when necessary by a accentuation as $\acute{X}$. The gauge has been chosen so that the scalar potential vanishes. From Eq. (2.51), we obtain the boundary condition for the equation of motion as

$$-\gamma p_0 \nabla \cdot \boldsymbol{\xi} + \frac{1}{\mu_0}\boldsymbol{B}_0 \cdot \boldsymbol{Q} = \frac{1}{\mu_0}\acute{\boldsymbol{B}}_0 \cdot \nabla \times \acute{\boldsymbol{A}} + \frac{1}{2\mu_0}(\boldsymbol{\xi} \cdot \nabla)(\acute{\boldsymbol{B}}_0^2 - \boldsymbol{B}_0^2), \tag{2.57}$$

and that for $\boldsymbol{A}$ from Eqs.(2.4), (2.53), and (2.54) as

$$\boldsymbol{n} \times \acute{\boldsymbol{A}} = -(\boldsymbol{n} \cdot \boldsymbol{\xi}) \acute{\boldsymbol{B}}_0. \tag{2.58}$$

Of course, $\acute{\boldsymbol{A}}$ must satisfy the equation

$$\nabla \times \nabla \times \acute{\boldsymbol{A}} = 0. \tag{2.59}$$

To obtain δW_F, δW_S, and δW_V with the boundary conditions Eqs. (2.57) and (2.58), we perform an integration by parts in Eq. (2.47), and as the result,

$$\delta W = \delta W_F - \frac{1}{2} \int (\boldsymbol{n} \cdot \boldsymbol{\xi}) \left(\gamma p_0 \nabla \cdot \boldsymbol{\xi} + \boldsymbol{\xi}_\perp \cdot \nabla p_0 - \frac{\boldsymbol{B}_0 \cdot \boldsymbol{Q}}{\mu_0} \right) dS, \tag{2.60}$$

where

$$\delta W_F = \frac{1}{2} \int \left\{ \frac{|\boldsymbol{Q}|^2}{\mu_0} - \boldsymbol{\xi}_\perp \cdot \boldsymbol{J} \times \boldsymbol{Q} + \gamma p_0 |\nabla \cdot \boldsymbol{\xi}|^2 + (\boldsymbol{\xi}_\perp \cdot \nabla p_0) \nabla \cdot \boldsymbol{\xi}_\perp \right\} d\boldsymbol{r}, \tag{2.61}$$

and $\boldsymbol{\xi}_\perp = \boldsymbol{\xi} - \xi_\parallel \boldsymbol{b}$. With Eqs. (2.57) and (2.58), the boundary term can be expressed as

$$\delta W - \delta W_F = \delta W_S + \delta W_V, \tag{2.62}$$

where

$$\delta W_S = \frac{1}{2} \int |\boldsymbol{n} \cdot \boldsymbol{\xi}|^2 \, \boldsymbol{n} \cdot \left[\left[\nabla \left(p_0 + \frac{\boldsymbol{B}_0^2}{2\mu_0} \right) \right] \right]_a, \tag{2.63}$$

$$\delta W_V = \frac{1}{2} \int \frac{\left| \nabla \times \acute{\boldsymbol{A}} \right|^2}{\mu_0} d\acute{\boldsymbol{r}}. \tag{2.64}$$

The surface integral in Eq. (2.63) is executed on the plasma surface and the volume integral in Eq. (2.64) is extended over the initial vacuum volume. Thus we obtain the final form of δW with Eqs.(2.61), (2.63), and (2.64), and investigate the MHD stability with the sufficient condition Eq. (2.49).

With the eigenvalues and the eigenfunctions of Eq. (2.44),$\boldsymbol{\xi}$ in Eq. (2.43) can be expressed as

$$\boldsymbol{\xi} = \sum_{i=1}^{\infty} \delta_i \boldsymbol{\xi}_i, \tag{2.65}$$

where we define that $\boldsymbol{\xi}_i$ belongs to ω_i and $\omega_1 \leq \omega_2 \leq \cdots$. By using Eq. (2.65), δW and K in Eqs. (2.47) and (2.48) can be written as

$$\delta W(\boldsymbol{\xi}^*, \boldsymbol{\xi}) = \frac{1}{2} \sum_{i=1}^{\infty} \rho \omega_i^2 \delta_i^2 \boldsymbol{\xi}_i^2, \tag{2.66}$$

$$K(\boldsymbol{\xi}^*, \boldsymbol{\xi}) = \frac{1}{2} \sum_{i=1}^{\infty} \rho \delta_i^2 \boldsymbol{\xi}_i^2. \tag{2.67}$$

Now, we introduce the Hessian matrix $\mathbf{Hs}$ [55] at the stationary point $\boldsymbol{s}$ of a function $f(\boldsymbol{x})$ as

$$Hs\left(f(\boldsymbol{s})\right)_{i,j} = \left(\frac{\partial^2 f(\boldsymbol{x})}{\partial x_i \partial x_j}\right)_{\boldsymbol{x}=\boldsymbol{s}}. \tag{2.68}$$

If the Hessian is positive (negative) definite at $\boldsymbol{s}$, then $f(\boldsymbol{x})$ attains a local minimum (maximum) at $\boldsymbol{s}$. If the Hessian has both positive and negative eigenvalues, then $\boldsymbol{s}$ is a saddle point for $f(\boldsymbol{x})$.

We can apply this theorem to the stability analysis. The Hessian matrix of δW in Eq. (2.66) can be calculated as

$$Hs\left(\delta W\right)_{i,j} = \begin{cases} \rho\delta_i^2\omega_i^2 & \text{for } i = j, \\ 0 & \text{for } i \neq j. \end{cases} \tag{2.69}$$

Since this matrix is diagonal and ρ is positive definite, the signs ω_i are identical to the signs of eigenvalues of $\mathbf{Hs}(\delta W)$; if $\omega_1 > 0$, δW attains a local minimum and the system is stable.

However, in the ideal MHD problem, the spectrum of the force operator $\boldsymbol{F}$ in Eq. (2.42) contains both discrete eigenvalues and continua. Moreover, if a rational surface exists in the plasma, the continuous spectrum always reaches the origin $\omega = 0$. This means that we cannot expand $\boldsymbol{\xi}$ with the eigenfunctions as Eq. (2.65) and the Hessian matrix Eq. (2.69) cannot be calculated.

To avoid such a problem, in the next chapter, we introduce the method that solves the eigenvalue problem associated with the Newcomb equation with the appropriate weight function and the boundary conditions at rational surfaces to eliminate the continuous spectra [29, 30]. Here the Newcomb equation is the inertia free linear ideal MHD equation [27]. With this method, the sign of δW_p can be identified, where δW_p expresses the potential energy of a plasma as $\delta W_p = \delta W_F + \delta W_S$, and the stability of a MHD equilibrium against ideal MHD motions can be analyzed.

In addition, for the external mode stability analysis, we need to identify the sign of $\delta W_p + \delta W_V$, and the vacuum magnetic energy integral δW_V must be carefully treated. This is one of the main issues in this dissertation, and two techniques to estimate δW_V are discussed in Chapter 5 and Appendix C.

Chapter 3

Two dimensional Newcomb equation

3.1 Introduction

The marginally stable state against the ideal MHD instability in a plasma is described by the Newcomb equation [27] derived from the linear ideal MHD equations Eqs. (2.38)-(2.41) without inertia. In an axisymmetric toroidal plasma, the Newcomb equation is a two-dimensional homogeneous differential equation for $Y(r,\theta)$, where Y is the radial component of the fluid displacement, r is the poloidal flux label of the equilibrium magnetic configuration (radial coordinate) and θ is the poloidal angle so defined that the equilibrium magnetic field lines are straight on each toroidal surface $r = const.$. In an one-dimensional case, the Newcomb equation and the eigenvalue problem associated with this equation is derived in Ref. [30] and is illustrated briefly in Appendix B. On the basis of this work, in this chapter, I introduce the two-dimensional Newcomb equation, the associated eigenvalue problem and a code MARG2D which solves this eigenvalue problem numerically [29]. Though the eigenvalues obtained by the MARG2D code do not correspond to a growth rate or a frequency of a MHD mode, the sign of them can identify the stability of a MHD equilibrium against ideal MHD motions.

In addition, I present another method for the stability analysis of external modes with the property of the Newcomb equation, called the *stability matrix* method. In this method, the change of the potential energy due to the plasma displacement is expressed by a quadratic form (a matrix form) with respect to the values of the displacement at the plasma surface [10]. The formulation used in this method is indispensable for the analysis of the resistive wall modes (RWMs) and a code DCON has already reported [13]. We adapt the MARG2D code so as to compute the matrix which is called the stability matrix, and the MARG2D-SM code is developed for the stability analysis with this matrix.

In Section 3.2, I introduce the flux coordinate system used in this chapter, and reduce the ideal MHD potential energy for an axisymmetric toroidal plasma to a quadratic form ex-

pressed by the Fourier harmonics in Section 3.3. After obtaining the two-dimensional Newcomb equation and deriving the Frobenius series of the singular solutions in Section 3.4, I formulate the eigenvalue problem associated with the Newcomb equation by introducing the weight function and the boundary conditions in Section 3.5. After these formulations, the outline of a code MARG2D is briefly mentioned in Section 3.6. After completing the explanation about the eigenvalue problem associated with the Newcomb equation, I review the stability matrix method, which is another method for the external mode analysis, and the MARG2D-SM code in Section 3.7.

3.2 Coordinate System

We introduce the usual cylindrical coordinate system(R, Z, ϕ) in which ϕ is the angle around the axis of symmetry as shown in Fig. 2.1. The equilibrium magnetic field$\boldsymbol{B}$ in an axisymmetric configuration can be expressed as Eq. (2.13) and satisfies force balance equations Eqs. (2.9)-(2.11). In the present work, we assume up-down symmetry for$\psi(R, Z)$; $\psi(R, -Z) = \psi(R, Z)$ for simplicity.

As in Ref. [56], we define the flux coordinate system(r, θ, ϕ) by

$$r^2(\psi) = 2R_0 \int_0^{\psi} \frac{q}{F} d\psi, \tag{3.1}$$

and

$$q(\psi) = \frac{\boldsymbol{B} \cdot \nabla\theta}{\boldsymbol{B} \cdot \nabla\phi}, \tag{3.2}$$

where R_0 is the R coordinate at the magnetic axis and$q$ is the safety factor already defined in Eq. (2.27). The radial coordinate$r$ has the dimension of length, whose value at the edge is same as the plasma minor radius,

$$r(\psi_a) = a. \tag{3.3}$$

The Jacobian $\sqrt{g(r,\theta)}$ is

$$\sqrt{g(r,\theta)} = \frac{R^2}{R_0} r, \tag{3.4}$$

and the quantity defined by

$$\beta_{r,\theta}(r,\theta) = \frac{\nabla r \cdot \nabla\theta}{|\nabla r|^2}, \tag{3.5}$$

provides a measure of nonorthogonality of this coordinate system. We also define the operator $\partial_\perp$ by

$$\partial_\perp \equiv \frac{\nabla r \cdot \nabla}{|\nabla r|^2} = \frac{\partial}{\partial r} + \beta_{r,\theta}(r,\theta)\frac{\partial}{\partial\theta}. \tag{3.6}$$

The equilibrium relation, Eq. (2.15), in the(r, θ, ϕ) coordinates system is expressed as

$$\frac{1}{r}\frac{\partial}{\partial r}\left[r\frac{d\psi}{dr}|\nabla r|^2\right] + \frac{d\psi}{dr}\frac{\partial}{\partial\theta}\left(|\nabla r|^2\beta_{r,\theta}\right) = -R^2\frac{dp}{d\psi} - F\frac{dF}{d\psi}. \tag{3.7}$$

3.3 Reduction of potential energy integral

We derive the reduced form of the ideal MHD potential energy integral expressed by the Fourier harmonics of the radial displacement. Subsequently, we use some notations on vector operation. We express by $\mathrm{Diag}(d_j)$ a diagonal matrix with diagonal elements d_j ($j = 1, 2, ...$). When $f(\theta)$ is an operator periodic in the θ-direction, we define

$$f_{l,m} \equiv \frac{1}{2\pi}\int_0^{2\pi} \exp(-\mathrm{i}l\theta)\hat{f}(\theta)\exp(\mathrm{i}m\theta)d\theta, \tag{3.8}$$

and we express by $\mathbf{f}$ the matrix made from $f_{l,m}$. Let $\boldsymbol{X}, \boldsymbol{Y}$ be arbitrary vectors and $\mathbf{A}$ be a real matrix, then the bracket $\langle \boldsymbol{X}|\mathbf{A}|\boldsymbol{Y}\rangle$ is defined as

$$\langle \boldsymbol{X}|\mathbf{A}|\boldsymbol{Y}\rangle \equiv \boldsymbol{X}^t\mathbf{A}\,\boldsymbol{Y} = \sum_{j,k} X_j A_{j,k} Y_k, \tag{3.9}$$

where the symbol t denotes transpose of a vector or a matrix.

3.3.1 Ideal MHD potential energy integral

In the axisymmetric configuration, the displacement vector $\boldsymbol{\xi}$ can be assumed to the $\boldsymbol{\xi} \propto \exp(-\mathrm{i}n\phi)$, where the integer n is the toroidal mode number. Since we are interested in the marginal ideal MHD stability, we impose the incompressibility condition, $\nabla\cdot\boldsymbol{\xi} = 0$.

By introducing variables

$$X = \boldsymbol{\xi}\cdot\nabla r, \tag{3.10}$$

$$V = r\left(\boldsymbol{\xi}\cdot\nabla\theta - \frac{1}{q}\boldsymbol{\xi}\cdot\nabla\phi\right), \tag{3.11}$$

we obtain the potential energy integral of a plasma δW_p expressed by X, V as

$$\delta W_p = \delta W_F + \delta W_S \tag{3.12}$$

$$= \pi\int_0^a dr\int_0^{2\pi} d\theta\mathcal{L}, \tag{3.13}$$

where the potential energy density $\mathcal{L}$ and the operator $\mathcal{D}_\theta(X)$ are defined as

$$\mathcal{L} = a\,|D_\theta(X)|^2 + b\left|\mathrm{i}nV + \frac{1}{q}\frac{\partial}{\partial r}(rX) + hX + r\beta_{r,\theta}D_\theta(X)\right|^2 + c\left|\frac{\partial V}{\partial\theta} + \frac{\partial}{\partial r}(rX)\right|^2 + e\,|X|^2, \tag{3.14}$$

$$\mathcal{D}_\theta(X) = \frac{1}{q}\frac{\partial X}{\partial\theta} - \mathrm{i}nX, \tag{3.15}$$

and the coefficients a, b, c, h, and e are given by

$$a(r,\theta) = \left(\frac{F}{R}\right)^2 \frac{1}{|\nabla r|^2}\frac{r}{R_0}, \tag{3.16}$$

$$b(r,\theta) = \left(\frac{F}{R_0}\right)^2 |\nabla r|^2 \frac{r}{R_0}, \tag{3.17}$$

$$c(r) = \left(\frac{F}{R_0}\right)^2 \frac{R_0}{r}, \tag{3.18}$$

$$h(r,\theta) = -\frac{1}{q}\left(2 + \frac{r}{|\nabla r|^2}\partial_\perp |\nabla r|^2 + r\frac{\partial}{\partial\theta}\beta_{r,\theta}\right), \tag{3.19}$$

and

$$e(r,\theta) = \frac{r}{R_0}\frac{dp}{dr}\partial_\perp R^2 + \frac{1}{R_0}\left(R^2\frac{dp}{dr} + F\frac{dF}{dr}\right)\left(2 + \frac{r}{|\nabla r|^2}\partial_\perp |\nabla r|^2 + 2r\frac{\partial}{\partial\theta}\beta_{r,\theta}\right). \tag{3.20}$$

The operator $\partial_\perp$ is already defined by Eq. (3.6).

3.3.2 Elimination of V

We first minimize δW_p for $V(r,\theta)$. The resultant Euler equation for $V(r,\theta)$ is

$$\frac{\partial}{\partial\theta}\left(\frac{\partial V}{\partial\theta} + \frac{\partial}{\partial r}(rX)\right) = -\mathrm{i}n\left(\frac{r}{R_0}\right)^2 |\nabla r|^2 \left[\mathrm{i}nV + \frac{1}{q}\frac{\partial}{\partial r}(rX) + \hat{H}X\right], \tag{3.21}$$

where the operator $\hat{H}$ is defined as

$$\hat{H}X \equiv hX + r\beta_{r,\theta}\mathcal{D}_\theta(X). \tag{3.22}$$

By substituting Eq. (3.21) into Eq. (3.14), we have the reduced form of the potential energy density given by

$$\mathcal{L} = a\,|\mathcal{D}_\theta(X)|^2 + \hat{b}\left|\frac{\partial}{\partial\theta}\left(\frac{\partial V}{\partial\theta} + \frac{\partial}{\partial r}(rX)\right)\right|^2 + c\left|\frac{\partial V}{\partial\theta} + \frac{\partial}{\partial r}(rX)\right|^2 + e\,|X|^2\,, \tag{3.23}$$

where

$$\hat{b} = \left(\frac{F}{R_0}\right)^2\left(\frac{R_0}{r}\right)^3 \frac{1}{n^2\,|\nabla r|^2}. \tag{3.24}$$

To solve Eq. (3.21) for $V(r,\theta)$, we express X, V by their Fourier harmonics in the poloidal direction

$$X(r,\theta) = X_0(r) + \sum_{m\neq 0} X_m \exp(\mathrm{i}m\theta), \tag{3.25}$$

$$V(r,\theta) = -\mathrm{i}\left(V_0(r) + \sum_{m\neq 0} V_m \exp(\mathrm{i}m\theta)\right). \tag{3.26}$$

From the solubility condition for Eq. (3.21)

$$\int_0^{2\pi} |\nabla r|^2 \left[inV + \frac{1}{q}\frac{\partial}{\partial r}(rX) + \hat{H}X \right] d\theta = 0, \tag{3.27}$$

we have

$$nV_0 + \frac{1}{q}\frac{\partial}{\partial r}(rX) = -\frac{1}{\langle |\nabla r|^2 \rangle}\boldsymbol{b} \cdot \left[n\bar{\boldsymbol{V}} + \frac{1}{q}\frac{\partial}{\partial r}(r\bar{\boldsymbol{X}}) \right] - \frac{1}{\langle |\nabla r|^2 \rangle}\boldsymbol{h} \cdot \boldsymbol{X}, \tag{3.28}$$

where

$$\langle |\nabla r|^2 \rangle \equiv \frac{1}{2\pi}\int_0^{2\pi} |\nabla r|^2 \, d\theta, \tag{3.29}$$

and the vectors $\boldsymbol{b}$, $\boldsymbol{h}$ are given by

$$\boldsymbol{b} = (..., (|\nabla r|^2)_{0,-1}, (|\nabla r|^2)_{0,1}, ...), \tag{3.30}$$

$$\boldsymbol{h} = (..., \hat{H}_{0,-1}, \hat{H}_{0,0}, \hat{H}_{0,1}, ...). \tag{3.31}$$

Here $(|\nabla r|^2)_{l,m}$ and $\hat{H}_{l,m}$ are computed by Eq. (3.8), and the vectors $\boldsymbol{X}$ and $\bar{\boldsymbol{X}}$ defined as

$$\boldsymbol{X} \equiv (..., X_{-2}, X_{-1}, X_0, X_1, X_2, ...), \tag{3.32}$$

and

$$\bar{\boldsymbol{X}} \equiv (..., X_{-2}, X_{-1}, X_1, X_2, ...), \tag{3.33}$$

and define $\boldsymbol{V}$ and $\bar{\boldsymbol{V}}$, similarly. By eliminating $V_0(r)$ in Eq. (3.21) with Eq. (3.28), we obtain a linear equation for $\bar{\boldsymbol{V}}$,

$$\underline{\bar{\mathbf{P}}}\bar{\boldsymbol{V}} = -\underline{\bar{\mathbf{Q}}}\frac{\partial}{\partial r}\left(r\bar{\boldsymbol{X}}\right) - n\left(\frac{r}{R_0}\right)^2 \mathbf{H}_B \boldsymbol{X}, \tag{3.34}$$

where the matrices $\underline{\bar{\mathbf{P}}}$, $\underline{\bar{\mathbf{Q}}}$, and $\bar{\mathbf{H}}_B$ are given by

$$\underline{\bar{\mathbf{P}}} = \mathrm{Diag}(m^2) + n^2\left(\frac{r}{R_0}\right)^2 \underline{\bar{\mathbf{G}}}, \tag{3.35}$$

$$\underline{\bar{\mathbf{Q}}} = \mathrm{Diag}(m) + \frac{n}{q}\left(\frac{r}{R_0}\right)^2 \underline{\bar{\mathbf{G}}}, \tag{3.36}$$

$$\bar{\mathbf{H}}_B = \hat{H}_{l,m} - \frac{1}{\langle |\nabla r|^2 \rangle}(|\nabla r|^2)_{l,0}\hat{H}_{0,m}, \tag{3.37}$$

and $\underline{\bar{\mathbf{G}}}$ is

$$\underline{\bar{G}}_{l,m} = (|\nabla r|^2)_{l,m} - \frac{1}{\langle |\nabla r|^2 \rangle}(|\nabla r|^2)_{l,0}(|\nabla r|^2)_{0,m}. \tag{3.38}$$

Here the notations on the arbitrary matrix $\mathbf{T}$ ($\underline{\bar{\mathbf{T}}}$, $\bar{\mathbf{T}}$, and $\underline{\mathbf{T}}$) express as

$$\underline{\bar{\mathbf{T}}} = \begin{pmatrix} \cdots & \cdots & \cdots & \cdots \\ \cdots & T_{-1,-1} & T_{-1,1} & \cdots \\ \cdots & T_{1,-1} & T_{1,1} & \cdots \\ \cdots & \cdots & \cdots & \cdots \end{pmatrix}, \quad \bar{\mathbf{T}} = \begin{pmatrix} \cdots & \cdots & \cdots & \cdots & \cdots \\ \cdots & T_{-1,-1} & T_{-1,0} & T_{-1,1} & \cdots \\ \cdots & T_{1,-1} & T_{1,0} & T_{1,1} & \cdots \\ \cdots & \cdots & \cdots & \cdots & \cdots \end{pmatrix}, \tag{3.39}$$

and

$$\underline{\mathbf{T}} = \begin{pmatrix} \cdots & \cdots & \cdots & \cdots \\ \cdots & T_{-1,-1} & T_{-1,1} & \cdots \\ \cdots & T_{0,-1} & T_{0,1} & \cdots \\ \cdots & T_{1,-1} & T_{1,1} & \cdots \\ \cdots & \cdots & \cdots & \cdots \end{pmatrix}, \tag{3.40}$$

where

$$\mathbf{T} = \begin{pmatrix} \cdots & \cdots & \cdots & \cdots & \cdots \\ \cdots & T_{-1,-1} & T_{-1,0} & T_{-1,1} & \cdots \\ \cdots & T_{0,-1} & T_{0,0} & T_{0,1} & \cdots \\ \cdots & T_{1,-1} & T_{1,0} & T_{1,1} & \cdots \\ \cdots & \cdots & \cdots & \cdots & \cdots \end{pmatrix}. \tag{3.41}$$

The matrices $\bar{\underline{\mathbf{P}}}$ and $\bar{\underline{\mathbf{Q}}}$ satisfy the relation

$$-\bar{\underline{\mathbf{Q}}} + \bar{\underline{\mathbf{P}}}\mathrm{Diag}\left(\frac{1}{m}\right) = n\left(\frac{r}{R_0}\right)^2 \bar{\underline{\mathbf{G}}}\bar{\underline{\mathbf{D}}}, \tag{3.42}$$

where the matrix $\bar{\underline{\mathbf{D}}}$ is defined as

$$\bar{\underline{\mathbf{D}}} \equiv \mathrm{Diag}\left(\frac{n}{m} - \frac{1}{q}\right). \tag{3.43}$$

Next, we express the terms including $\bar{V}$ in Eq. (3.23) as

$$\frac{\partial V}{\partial \theta} + \frac{\partial}{\partial r}(rX) = \left[\mathrm{Diag}(m)\bar{\boldsymbol{V}} + \frac{\partial}{\partial r}(r\bar{\boldsymbol{X}})\right] \cdot \bar{\boldsymbol{e}}(\theta) + \frac{\partial}{\partial r}(rX_0), \tag{3.44}$$

$$\frac{\partial}{\partial \theta}\left(\frac{\partial V}{\partial \theta} + \frac{\partial}{\partial r}(rX)\right) = \mathrm{iDiag}(m)\left[\mathrm{Diag}(m)\bar{\boldsymbol{V}} + \frac{\partial}{\partial r}(r\bar{\boldsymbol{X}})\right] \cdot \bar{\boldsymbol{e}}(\theta), \tag{3.45}$$

where $\bar{\boldsymbol{e}}(\theta)$ is defined as

$$\bar{\boldsymbol{e}}(\theta) = (..., \exp(-2\mathrm{i}\theta), \exp(-\mathrm{i}\theta), \exp(\mathrm{i}\theta), \exp(2\mathrm{i}\theta), ...). \tag{3.46}$$

By substituting the solution of Eq. (3.34)

$$\bar{\boldsymbol{V}} = -\left(\bar{\underline{\mathbf{P}}}\right)^{-1} \mathbf{Q}\frac{\partial}{\partial r}(r\bar{\boldsymbol{X}}) - n\left(\frac{r}{R_0}\right)^2 \left(\bar{\underline{\mathbf{P}}}\right)^{-1} \mathbf{H}_B \boldsymbol{X}, \tag{3.47}$$

into Eq. (3.44), we obtain

$$\begin{aligned} \mathrm{Diag}(m)\bar{\boldsymbol{V}} + \frac{\partial}{\partial r}(r\bar{\boldsymbol{X}}) = &\left[-\mathrm{Diag}(m)\left(\bar{\underline{\mathbf{P}}}\right)^{-1} \bar{\underline{\mathbf{Q}}} + \mathbf{I}\right]\frac{\partial}{\partial r}(r\bar{\boldsymbol{X}}) \\ &- n\left(\frac{r}{R_0}\right)^2 \mathrm{Diag}(m)\left(\bar{\underline{\mathbf{P}}}\right)^{-1} \bar{\mathbf{H}}_B \boldsymbol{X}, \end{aligned} \tag{3.48}$$

where $\mathbf{I}$ is the unit matrix. With the relation Eq. (3.42), we obtain

$$\mathrm{Diag}(m)\bar{V} + \frac{\partial}{\partial r}(r\bar{X}) = n\left(\frac{r}{R_0}\right)^2 \left[\underline{\bar{\mathbf{L}}}_B \underline{\bar{\mathbf{D}}} \frac{\partial}{\partial r}(r\bar{X}) - \bar{\mathbf{H}}\bar{X}\right], \tag{3.49}$$

where the matrices $\underline{\bar{\mathbf{L}}}_B$ and $\underline{\bar{\mathbf{H}}}$ are given by

$$\underline{\bar{\mathbf{L}}}_B \equiv \mathrm{Diag}(m)\left(\underline{\bar{\mathbf{P}}}\right)^{-1} \underline{\bar{\mathbf{G}}}, \tag{3.50}$$

$$\bar{\mathbf{H}} \equiv \mathrm{Diag}(m)\left(\underline{\bar{\mathbf{P}}}\right)^{-1} \bar{\mathbf{H}}_B. \tag{3.51}$$

By using Eq. (3.49), we have δW_p expressed in the quadratic form of $\boldsymbol{X}$,

$$\delta W_p = 2\pi^2 \int_0^a \mathcal{L}(\boldsymbol{X}, \boldsymbol{X}) dr, \tag{3.52}$$

where

$$\begin{aligned}\mathcal{L}(\boldsymbol{X}, \boldsymbol{X}) = &\left(\frac{F}{R_0}\right)^2 \frac{R_0}{r}\left|\frac{\partial}{\partial r}(rX_0)\right|^2 + \langle \boldsymbol{X}|\mathbf{K}|\boldsymbol{X}\rangle \\ &+ \left(\frac{F}{R_0}\right)^2 \frac{r}{R_0}\left[\left\langle \frac{\partial}{\partial r}(r\bar{\boldsymbol{X}})|\underline{\bar{\mathbf{D}}}\underline{\bar{\mathbf{L}}}\underline{\bar{\mathbf{D}}}|\frac{\partial}{\partial r}(r\bar{\boldsymbol{X}})\right\rangle\right. \\ &\left. + \left\langle \boldsymbol{X}|\underline{\mathbf{M}}\underline{\bar{\mathbf{D}}}|\frac{\partial}{\partial r}(r\bar{\boldsymbol{X}})\right\rangle + \left\langle \frac{\partial}{\partial r}(r\bar{\boldsymbol{X}})|\underline{\bar{\mathbf{D}}}\,(\underline{\mathbf{M}})^t|\boldsymbol{X}\right\rangle\right].\end{aligned} \tag{3.53}$$

Here the matrices $\underline{\bar{\mathbf{L}}}$, $\underline{\mathbf{M}}$, and $\mathbf{K}$ are defined as

$$\underline{\bar{\mathbf{L}}} = \left(\underline{\bar{\mathbf{L}}}_B\right)^t \hat{\mathbf{G}}\underline{\bar{\mathbf{L}}}_B, \tag{3.54}$$

$$\underline{\mathbf{M}} = -(\underline{\mathbf{H}})^t \hat{\mathbf{G}}\underline{\bar{\mathbf{L}}}_B, \tag{3.55}$$

$$\mathbf{K} = \left(\frac{F}{R_0}\right)^2 \frac{r}{R_0}(\mathbf{A} + \mathbf{N}) + \mathbf{E}, \tag{3.56}$$

and matrices in Eqs. (3.54)-(3.56) are given by

$$\hat{\mathbf{G}} = \mathrm{Diag}(m)\left(\frac{1}{|\nabla r|^2}\right)\mathrm{Diag}(m) + n^2\left(\frac{r}{R_0}\right)^2 \mathbf{I}, \tag{3.57}$$

$$\mathbf{A} = \mathrm{Diag}\left(\frac{m}{q} - n\right)\left(\frac{R_0}{R}\right)^2 \left(\frac{1}{|\nabla r|^2}\right)\mathrm{Diag}\left(\frac{m}{q} - n\right), \tag{3.58}$$

$$\mathbf{N} = \left(\bar{\mathbf{H}}\right)^t \hat{\mathbf{G}}\bar{\mathbf{H}}, \tag{3.59}$$

and

$$\mathbf{E} = (e(r,\theta)) = \frac{1}{2\pi}\int_0^{2\pi} e(r,\theta)\exp(\mathrm{i}(m-l)\theta)d\theta. \tag{3.60}$$

3.3.3 Normalization

We measure the length by a in Eq. (3.3) and the magnetic field by B_0 at the magnetic axis. Thus variables are written as

$$r = a\check{r}, \tag{3.61}$$

$$F = R_0 B_0 \check{F}, \tag{3.62}$$

$$p = B_0^2 \check{p}, \tag{3.63}$$

and

$$\psi = R_0^2 B_0 \check{\psi}. \tag{3.64}$$

The matrices $\bar{\underline{\mathbf{L}}}$, $\underline{\mathbf{M}}$, and $\mathbf{N}$ are non-dimensional, and $\mathbf{K}$ can be written as

$$\mathbf{K} = \frac{a}{R_0} B_0^2 \check{\mathbf{K}}. \tag{3.65}$$

The normalized potential energy becomes

$$\delta \check{W}_p = 2\pi^2 \int_0^1 \check{\mathcal{L}} d\check{r}, \tag{3.66}$$

and the potential energy density $\mathcal{L}$ reads

$$\begin{aligned} \check{\mathcal{L}} = \frac{1}{\epsilon^2} \frac{\check{F}^2}{\check{r}} \left| \frac{\partial Y_0}{\partial r} \right| + \left\langle \boldsymbol{Y} \left| \frac{\check{\mathbf{K}}}{\check{r}^2} \right| \boldsymbol{Y} \right\rangle + \check{r} \check{F}^2 \left\langle \frac{\partial \bar{\boldsymbol{Y}}}{\partial r} | \bar{\underline{\mathbf{D}}} \bar{\underline{\mathbf{L}}} \bar{\underline{\mathbf{D}}} | \frac{\partial \bar{\boldsymbol{Y}}}{\partial r} \right\rangle \\ + \check{F}^2 \left[\left\langle \frac{\partial \bar{\boldsymbol{Y}}}{\partial r} | \bar{\underline{\mathbf{D}}} \, (\underline{\mathbf{M}})^t \, | \boldsymbol{Y} \right\rangle + \left\langle \boldsymbol{Y} | \underline{\mathbf{M}} \bar{\underline{\mathbf{D}}} | \frac{\partial \bar{\boldsymbol{Y}}}{\partial r} \right\rangle \right], \end{aligned} \tag{3.67}$$

where $\epsilon = a/R_0$, and we have introduced the vector function $\boldsymbol{Y}$ as

$$\boldsymbol{Y} = \check{r} \boldsymbol{X}. \tag{3.68}$$

3.3.4 Surface term

The surface term driving the unstable external kink mode can be derived from the last two terms in the right hand side (RHS) of Eq. (3.67). We divide the matrix $\underline{\mathbf{M}}$ into the diagonal matrix $\bar{\underline{\mathbf{M}}}_D$ and the off-diagonal matrix $\underline{\mathbf{M}}_O$ as

$$\underline{\mathbf{M}} = \bar{\underline{\mathbf{M}}}_D + \underline{\mathbf{M}}_O \tag{3.69}$$

$$= \begin{pmatrix} \ddots & & & \\ & M_{-1,-1} & 0 & \\ & 0 & M_{1,1} & \\ & & & \ddots \end{pmatrix} + \begin{pmatrix} & \vdots & & \\ & 0 & M_{-1,1} & M_{-1,2} \\ \cdots & M_{0,-1} & M_{0,1} & M_{0,2} \\ & M_{1,-1} & 0 & M_{1,2} \\ & M_{2,-1} & M_{2,1} & 0 \\ & & \vdots & \end{pmatrix} \cdots . \tag{3.70}$$

Then the last two terms in the RHS of Eq. (3.67) read

$$\begin{aligned}\check{F}^2\left[\left\langle\frac{\partial\bar{\boldsymbol{Y}}}{\partial r}|\bar{\underline{\mathbf{D}}}\,(\underline{\mathbf{M}})^t\,|\boldsymbol{Y}\right\rangle+\left\langle\boldsymbol{Y}|\underline{\mathbf{M}}\bar{\underline{\mathbf{D}}}|\frac{\partial\bar{\boldsymbol{Y}}}{\partial r}\right\rangle\right]\\ =\check{F}^2\left[\left\langle\frac{\partial\bar{\boldsymbol{Y}}}{\partial r}|\bar{\underline{\mathbf{D}}}\,(\underline{\mathbf{M}}_O)^t\,|\boldsymbol{Y}\right\rangle+\left\langle\boldsymbol{Y}|\underline{\mathbf{M}}_O\bar{\underline{\mathbf{D}}}|\frac{\partial\bar{\boldsymbol{Y}}}{\partial r}\right\rangle\right]\\ +\left\langle\frac{\partial\bar{\boldsymbol{Y}}}{\partial r}|\check{F}^2\bar{\underline{\mathbf{D}}}\left(\bar{\underline{\mathbf{M}}}_D\right)^t|\bar{\boldsymbol{Y}}\right\rangle+\left\langle\bar{\boldsymbol{Y}}|\check{F}^2\bar{\underline{\mathbf{M}}}_D\bar{\underline{\mathbf{D}}}|\frac{\partial\bar{\boldsymbol{Y}}}{\partial r}\right\rangle.\end{aligned}\tag{3.71}$$

Since we assume up-down symmetry, the matrix$\underline{\mathbf{M}}$ is a real matrix, and

$$\begin{aligned}\int_{r_1}^{r_2}\left[\left\langle\frac{\partial\bar{\boldsymbol{Y}}}{\partial r}|\bar{\underline{\mathbf{M}}}_H|\bar{\boldsymbol{Y}}\right\rangle+\left\langle\boldsymbol{Y}|\bar{\underline{\mathbf{M}}}_H|\frac{\partial\bar{\boldsymbol{Y}}}{\partial r}\right\rangle\right]dr\\ =\int_{r_1}^{r_2}\frac{d}{dr}\langle\bar{\boldsymbol{Y}}|\bar{\underline{\mathbf{M}}}_H|\bar{\boldsymbol{Y}}\rangle dr-\int_{r_1}^{r_2}\left\langle\bar{\boldsymbol{Y}}\left|\frac{d\bar{\underline{\mathbf{M}}}_H}{dr}\right|\bar{\boldsymbol{Y}}\right\rangle dr.\end{aligned}\tag{3.72}$$

Here the matrix

$$\bar{\underline{\mathbf{M}}}_H(r)\equiv F^2\bar{\underline{\mathbf{M}}}_D\bar{\underline{\mathbf{D}}}\tag{3.73}$$

is a real, diagonal matrix, and

$$\langle\bar{\boldsymbol{Y}}|\bar{\underline{\mathbf{M}}}_H|\bar{\boldsymbol{Y}}\rangle=\sum_{j\neq0}(M_H)_{j,j}\,|Y_j|^2.\tag{3.74}$$

Afterward, we have suppressed the symbol $\check{x}$ expressing the normalized quantities. For the harmonics Y_j without any rational surfaces, we obtain

$$\int_0^1\frac{d}{dr}\left[(M_H(r))_{j,j}|Y_j(r)|^2\right]dr=(M_H(1))_{j,j}|Y_j(1)|^2.\tag{3.75}$$

Here we have used the regularity condition

$$\boldsymbol{Y}(0)=0.\tag{3.76}$$

For the harmonics Y_m with a rational surface, on the other hand, we derive

$$\begin{aligned}\int_0^1\frac{d}{dr}\left[(M_H(r))_{m,m}|Y_m(r)|^2\right]dr\\ =(M_H(1))_{m,m}|Y_m(1)|^2+(M_H(r_m-0))_{m,m}|Y_m(r_m-0)|^2\\ -(M_H(r_m+0))_{m,m}|Y_m(r_m+0)|^2,\end{aligned}\tag{3.77}$$

where r_m is the position of the rational surface. However, $(M_H(r))_{m,m}\sim(r-r_m)$ around $r=r_m$, and as shown in Subsection 3.4.2, the singularity of $Y_m(r)$ is bounded as $|Y_m(r)|^2\sim|r-r_m|^{-1+2\mu_{mer}}$, where μ_{mer} is the Suydam-Mercier index. Therefore, we have

$$(M_H(r))_{m,m}|Y_m(r)|^2\sim|r-r_m|^{2\mu_{mer}}\to0.\tag{3.78}$$

Thus the surface terms disappear at the rational surfaces and we find

$$\int_0^1 \frac{d}{dr}\langle \bar{\boldsymbol{Y}}|\bar{\underline{\mathbf{M}}}_H|\bar{\boldsymbol{Y}}\rangle dr = \sum_{j\neq 0}(M_H(1))_{j,j}|Y_j(1)|^2. \tag{3.79}$$

By using Eqs.(3.71), (3.72) and (3.79) in Eqs. (3.66) and (3.67), the normalized potential energy can be written as

$$\delta W_p = 2\pi^2 \int_0^1 \mathcal{L} dr + \delta W_s, \tag{3.80}$$

where the potential energy density $\mathcal{L}$ is

$$\begin{aligned}\mathcal{L} = \frac{1}{\epsilon^2}\frac{F^2}{r}\left|\frac{\partial Y_0}{\partial r}\right|^2 + \left\langle \boldsymbol{Y}\left|\frac{1}{r^2}\mathbf{K}\right|\boldsymbol{Y}\right\rangle + \left\langle \bar{\boldsymbol{Y}}\left|-\frac{d}{dr}\bar{\underline{\mathbf{M}}}_H\right|\bar{\boldsymbol{Y}}\right\rangle \\ + rF^2\left\langle \frac{\partial \bar{\boldsymbol{Y}}}{\partial r}|\bar{\underline{\mathbf{D}}}\bar{\underline{\mathbf{L}}}\bar{\underline{\mathbf{D}}}|\frac{\partial \bar{\boldsymbol{Y}}}{\partial r}\right\rangle + F^2\left[\left\langle \frac{\partial \bar{\boldsymbol{Y}}}{\partial r}|\bar{\underline{\mathbf{D}}}\,(\underline{\mathbf{M}}_O)^t\,|\boldsymbol{Y}\right\rangle + \left\langle \boldsymbol{Y}|\underline{\mathbf{M}}_O\bar{\underline{\mathbf{D}}}|\frac{\partial \bar{\boldsymbol{Y}}}{\partial r}\right\rangle\right],\end{aligned} \tag{3.81}$$

and the surface term is

$$\delta W_s = 2\pi^2 \sum_{j\neq 0}(M_H)_{j,j}(1)|Y_j(1)|^2. \tag{3.82}$$

The surface term W_s and W_V in Eq. (2.64) give the boundary condition at the plasma surface for the free boundary modes [32, 57], and determines the behavior of the modes there.

The singular structure of the quadratic form, Eq. (3.81), is explicitly described by the matrix $\bar{\underline{\mathbf{D}}}$ defined by Eq. (3.43). This structure is later exploited in deriving the Newcomb equation and in formulating the eigenvalue problem. For an up-down symmetric equilibrium, all matrices in Eq. (3.81) are real. In addition, the matrices $\bar{\underline{\mathbf{L}}}$, $\mathbf{K}$, and $\bar{\underline{\mathbf{M}}}_H$ are symmetric.

3.4 2D Newcomb Equation

3.4.1 Euler equation for $\boldsymbol{Y}$

We divide the potential energy density $\mathcal{L}$ given by Eq. (3.81) into two parts: $\mathcal{L}_0$ for the $l = 0$ mode and $\tilde{\mathcal{L}}$ for the $l \neq 0$ modes,

$$\mathcal{L} = \tilde{\mathcal{L}} + \mathcal{L}_0, \tag{3.83}$$

Here $\tilde{\mathcal{L}}$ in Eq. (3.83) is given by

$$\begin{aligned}\tilde{\mathcal{L}} = rF^2\left\langle \frac{d\bar{\boldsymbol{Y}}}{dr}|\bar{\underline{\mathbf{D}}}\bar{\underline{\mathbf{L}}}\bar{\underline{\mathbf{D}}}|\frac{d\bar{\boldsymbol{Y}}}{dr}\right\rangle + F^2\left[\left\langle \frac{d\bar{\boldsymbol{Y}}}{dr}|\bar{\underline{\mathbf{D}}}\,(\underline{\mathbf{M}}_O)^t\,|\bar{\boldsymbol{Y}}\right\rangle + \left\langle \bar{\boldsymbol{Y}}|\underline{\mathbf{M}}_O\bar{\underline{\mathbf{D}}}|\frac{d\bar{\boldsymbol{Y}}}{dr}\right\rangle\right] \\ + \langle \bar{\boldsymbol{Y}}|\check{\mathbf{K}}|\bar{\boldsymbol{Y}}\rangle + \sum_{l\neq 0} Y_l\frac{K_{l,0}}{r^2}Y_0 + F^2\sum_{l\neq 0}\frac{dY_l}{dr}\left(\frac{n}{l}-\frac{1}{q}\right)(M_O)_{0,l}Y_0,\end{aligned} \tag{3.84}$$

where

$$\check{\mathbf{K}} = \sum_{l\neq 0, j\neq 0}\frac{K_{l,j}}{r^2} - \frac{d}{dr}(M_H)_{l,j}. \tag{3.85}$$

The Euler equation for Y_l ($l = \pm 1, \pm 2 \ldots$) derived from Eq. (3.84) reads

$$(\mathcal{N}\boldsymbol{Y})_l = \sum_{j \neq 0,l} \left[\frac{d}{dr}\left(f_{l,j} \frac{dY_j}{dr} \right) + g_{l,j} \frac{dY_j}{dr} + h_{l,j} Y_j \right] + \frac{d}{dr}\left[f_{l,l} \frac{dY_l}{dr} \right] - \check{K}_{l,l} Y_l + \frac{d}{dr}(g_{l,0} Y_0) + h_{l,0} Y_0 = 0, \tag{3.86}$$

where

$$f_{l,j} = rF^2 \left(\frac{n}{l} - \frac{1}{q} \right) \left(\frac{n}{j} - \frac{1}{q} \right) L_{l,j}, \tag{3.87}$$

$$g_{l,j} = F^2 \left[\left(\frac{n}{l} - \frac{1}{q} \right) (M_O)_{j,l} - \left(\frac{n}{j} - \frac{1}{q} \right) (M_O)_{l,j} \right], \tag{3.88}$$

$$h_{l,j} = \frac{d}{dr}\left[F^2 \left(\frac{n}{l} - \frac{1}{q} \right) (M_O)_{j,l} \right] - \check{K}_{l,j}, \tag{3.89}$$

$$g_{l,0} = F^2 \left(\frac{n}{l} - \frac{1}{q} \right) (M_O)_{0,j}, \tag{3.90}$$

$$h_{l,0} = -\check{K}_{l,0}. \tag{3.91}$$

Next, $\mathcal{L}_0$ is given by

$$\mathcal{L}_0 = \frac{1}{\epsilon^2} \frac{F^2}{r} \left| \frac{dY_0}{dr} \right|^2 + \frac{K_{0,0}}{r^2} |Y_0|^2 + Y_0 \sum_{l \neq 0} \frac{K_{0,l}}{r^2} Y_l + Y_0 \sum_{l \neq 0} F^2 (\underline{\mathbf{M}}_O \underline{\bar{\mathbf{D}}})_{0,l} \frac{dY_l}{dr}, \tag{3.92}$$

where the last two terms in Eq. (3.92) mean the correlation between the $l = 0$ mode and the $l \neq 0$ modes. The Euler equation for $Y_0(r)$ derived from Eq. (3.92) is

$$(\mathcal{N}\boldsymbol{Y})_0 = \frac{d}{dr}\left(f_{0,0} \frac{dY_0}{dr} \right) + \sum_{l \neq 0} \left(g_{0,l} \frac{dY_l}{dr} + \check{h}_{0,l} Y_l \right) + \check{h}_{0,0} Y_0 = 0, \tag{3.93}$$

where

$$f_{0,0} = \frac{1}{\epsilon^2} \frac{F^2}{r}, \tag{3.94}$$

$$g_{0,l} = -F^2 \left(\frac{n}{l} - \frac{1}{q} \right) (M_O)_{0,l}, \tag{3.95}$$

$$\check{h}_{0,l} = -\frac{K_{0,l}}{r^2}. \tag{3.96}$$

Equations (3.86) and (3.93) are the two-dimensional Newcomb equation expressed by the Fourier harmonics $\{Y_l(r)\}$.

3.4.2 Frobenius solution

When the maximum poloidal mode number is taken to be M ($l = 0, \pm 1, \ldots, \pm M$), then Eqs. (3.86) and (3.93) are second order ordinary differential equations for $(2M + 1)$ harmonics.

Therefore, they have $2(2M+1)$ fundamental solutions around each rational surface $r = r_m$ $(nq(r_m) = m)$. Among the fundamental solutions, two solutions are singular at $r = r_m$, comprising of big and small solutions, and the remainders are analytic at $r = r_m$ [58, 59]. We obtain the singular solutions by using the Frobenius method [60]. The singular solutions can be expressed as

$$\boldsymbol{Y} = x^{\alpha}\left[\boldsymbol{y}^{(0)} + x\boldsymbol{y}^{(1)} + \cdots\right], \tag{3.97}$$

where

$$x \equiv r - r_m, \tag{3.98}$$

and α is the index to be determined. The vector $\boldsymbol{y}^{(0)} = \{y_l^{(0)}\}$ is

$$y_l^{(0)} = \begin{cases} y_m^{(0)} & \text{for } l = m, \\ 0 & \text{for } l \neq m, \end{cases} \tag{3.99}$$

and $(n/m - 1/q)$ is expanded as

$$\frac{n}{m} - \frac{1}{q} = x \cdot \left[\frac{q'}{q^2}\right]_{r=r_m} + x^2 \cdot \frac{1}{2}\left[\frac{q''}{q^2} - 2\frac{q'}{q^3}\right]_{r=r_m} + \cdots. \tag{3.100}$$

In the $l = m$ case, the lowest power components of x in Eq. (3.86) are

$$\frac{d}{dr}\left[rF^2\left(\frac{n}{m} - \frac{1}{q}\right)^2 L_{m,m}\frac{dY_m}{dr}\right] = \left[rF^2\left(\frac{q'}{q^2}\right)^2 L_{m,m}\right]_{r=r_m} \alpha(\alpha+1)x^{\alpha}y_m^{(0)} + \cdots, \tag{3.101}$$

$$-\check{K}_{m,m}Y_m = -\left(\check{K}_{m,m}\right)_{r=r_m} x^{\alpha}y_m^{(0)} + \cdots, \tag{3.102}$$

and since the lowest x power in Y_j is $x^{\alpha+1}$,

$$\begin{aligned} &\frac{d}{dr}\left[rF^2\left(\frac{n}{m} - \frac{1}{q}\right)\left(\frac{n}{j} - \frac{1}{q}\right)L_{m,j}\frac{dY_j}{dr}\right] \\ &\quad = \left(\frac{n}{j} - \frac{1}{q}\right)\left[rF^2\frac{q'}{q}L_{m,j}\right](\alpha+1)^2 x^{\alpha}y_p^{(1)} + \cdots, \end{aligned} \tag{3.103}$$

$$\begin{aligned} &F^2\left[\left(\frac{n}{m} - \frac{1}{q}\right)(M_O)_{j,m} - \left(\frac{n}{j} - \frac{1}{q}\right)(M_O)_{m,j}\right]\frac{dY_j}{dr} \\ &\quad = -\left(\frac{n}{j} - \frac{1}{q}\right)\left[F^2(M_O)_{m,j}\right](\alpha+1)x^{\alpha}y_p^{(1)}. \end{aligned} \tag{3.104}$$

Since the lowest x power of other terms in Eq. (3.86) is $x^{\alpha+1}$, we obtain the equation as

$$\begin{aligned} &\left\{\left[rF^2\left(\frac{q'}{q^2}\right)^2 L_{m,m}\right]\alpha(\alpha+1) - \check{K}_{m,m}\right\}y_m^{(0)} \\ &\quad + \sum_{j\neq m}\left(\frac{n}{j} - \frac{1}{q}\right)(\alpha+1)\left\{\left[rF^2\frac{q'}{q^2}L_{m,j}\right](\alpha+1) - \left[F^2(M_O)_{m,j}\right]\right\}y_j^{(1)} = 0. \end{aligned} \tag{3.105}$$

As well as $l = m$ case, in the $l \neq m$ and $l \neq 0$ case, we derive the equation with the lowest x power ($= x^{\alpha-1}$) terms in Eq. (3.86) as

$$\left(\frac{n}{l} - \frac{1}{q}\right)\alpha(\alpha+1)\sum_{j\neq m}\left(\frac{n}{j} - \frac{1}{q}\right)\left[rF^2 L_{l,j}\right]y_j^{(1)} + \left(\frac{n}{l} - \frac{1}{q}\right)\alpha\left\{\left[rF^2\frac{q'}{q^2}L_{l,m}\right]\alpha + \left[F^2(M_O)_{m,l}\right]\right\}y_m^{(0)} = 0. \tag{3.106}$$

In the $l = 0$ case, the lowest x power of Eq. (3.93) is $x^{\alpha+2}$, and we obtain the condition as

$$y_0^{(1)} = 0. \tag{3.107}$$

Equations (3.105) and (3.106) are the homogeneous equations for $y_m^{(0)}$ and $y_j^{(1)}$ ($j \neq m$), and the index α is determined by the condition that these equations have the nontrivial solution. By assuming $\alpha \neq 0$, we obtain the linear equation for $y_j^{(1)}$ from Eq. (3.106) as

$$\left[L_{l,j}\right]z_p^{(1)} = -\left\{\left[\frac{q'}{q^2}L_{l,m}\right]\alpha + \left[\frac{(M_O)_{m,l}}{r}\right]\right\}y_m^{(0)}, \tag{3.108}$$

$$z_p^{(1)} = \left(\frac{n}{j} - \frac{1}{q}\right)(\alpha+1)y_j^{(1)}. \tag{3.109}$$

From these equations, we obtain

$$z_l^{(1)} = -\left\{\alpha\frac{q'}{q^2}\left(L_B^{-1}\right)_{l,j}[L_{j,m}] + \left(L_B^{-1}\right)_{l,j}\left[\frac{(M_O)_{m,j}}{r}\right]\right\}y_m^{(0)}, \tag{3.110}$$

$$y_l^{(1)} = \left(\frac{n}{l} - \frac{1}{q}\right)^{-1}\frac{z_l^{(1)}}{\alpha+1}, \tag{3.111}$$

where $\alpha \neq -1$ is assumed. With Eqs. (3.110) and (3.111), Eq. (3.105) reads

$$\left\{rF^2\left(\frac{q'}{q^2}\right)^2[L_{m,m} - L_{m,l}\left(L_B^{-1}\right)_{l,j}L_{j,m}]\alpha(\alpha+1) - \left[\check{K}_{m,m} + \left[F^2\frac{q'}{q^2}\right]L_{m,l}\left(L_B^{-1}\right)_{l,j}(M_O)_{m,j} - \left[\frac{F^2}{r}\right](M_O)_{m,l}\left(L_B^{-1}\right)_{l,j}(M_O)_{m,j}\right]\right\}y_m^{(0)} = 0, \tag{3.112}$$

where we use the condition that $\underline{\bar{\mathbf{L}}}$ and $\underline{\bar{\mathbf{L}}}_B$ are real and diagonal matrices. By introducing

$$a \equiv \left[rF^2\left(\frac{q'}{q^2}\right)^2\right][L_{m,m} - L_{m,l}\left(L_B^{-1}\right)_{l,j}L_{j,m}], \tag{3.113}$$

$$c \equiv \check{K}_{m,m} + \left[F^2\frac{q'}{q^2}\right]L_{m,l}\left(L_B^{-1}\right)_{l,j}(M_O)_{m,j} - \left[\frac{F^2}{r}\right](M_O)_{m,l}\left(L_B^{-1}\right)_{l,j}(M_O)_{m,j}, \tag{3.114}$$

Eq. (3.112) can be rewritten as

$$a\alpha(\alpha+1) = c. \tag{3.115}$$

As the solutions of Eq. (3.115), we obtain

$$\alpha^b = -\frac{1}{2} - \mu_{mer}, \tag{3.116}$$

$$\alpha^s = -\frac{1}{2} + \mu_{mer}, \tag{3.117}$$

where the Suydam-Mercier index μ_{mer} is

$$\mu_{mer} = \sqrt{\frac{1}{4} + \frac{c}{a}}. \tag{3.118}$$

By using Eqs. (3.116) and (3.117) in Eqs. (3.110) and (3.111), $y_m^{(0)}$ and $y_l^{(1)}$ $(l \neq m)$ in Eq. (3.97) can be determined.

3.5 Eigenvalue Problem

Here we formulate the eigenvalue problem associated with the two-dimensional Newcomb equation and introduce the boundary condition. The spectra of this eigenvalue problem consist of only discrete eigenvalues. Thus, the eigenvalues identify the stable state as well as the unstable state.

3.5.1 Kinetic energy integral

We introduce δW_k be a semi-positive definite (non-negative) quadratic form of the vector function $\boldsymbol{Y}(r)$. The condition that the functional

$$\mathcal{W} \equiv \delta W_p - \lambda \delta W_k \tag{3.119}$$

is stationary for arbitrary variations of $\boldsymbol{Y}$ yields an eigenvalue problem associated with the Newcomb equation, where λ is the eigenvalue. The spectral structure of this eigenvalue problem is determined by the choice of the kinetic energy integral and the boundary conditions at the rational surfaces [30, 57]; the latter choices are discussed in the next subsection. In the one-dimensional case, the appropriate kinetic energy integral and the boundary conditions are introduced in Ref. [30] and Appendix B. This theory in the one-dimensional case is applied to the two-dimensional case as

$$\delta W_k = 2\pi^2 \int \sum_l \rho_l(r) |Y_l(r)|^2 dr, \tag{3.120}$$

where the weight function $\rho_m(r)$ is given by

$$\rho_m(r) = F^2 \left(\frac{m}{q} - n \right)^2 \tag{3.121}$$

for Y_m(r) if $m = nq$ for some r in [0,1], and by

$$\rho_l(r) = F^2 \tag{3.122}$$

for $Y_l(r)$ if $l \neq nq$ for any r in [0,1]. Therefore, the eigenvalue problem generated by Eqs. (3.119) and (3.120) is

$$\mathcal{N}_\lambda \boldsymbol{Y} = 0, \tag{3.123}$$

$$\mathcal{N}_\lambda = \mathcal{N} + \lambda \mathrm{Diag}(\rho_l(r)). \tag{3.124}$$

This is the eigenvalue problem associated with the two-dimensional Newcomb equation. We find by direct inspection that the Frobenius series of the singular solutions for Eq. (3.123) coincide with those for the original Newcomb equation to the second terms.

The spectra λ of the eigenvalue problem consist of real and denumerable eigenvalues without continuous spectra by imposing correctly the boundary conditions for $\boldsymbol{Y}(r)$ at the rational surfaces. The eigenvalues λ_j can be ordered in the form of $\lambda_0 \leq \lambda_1 \leq ...$, and each eigenfunction behaves as a sum of the small and the analytic solutions for the original Newcomb equation at each rational surface thanks to the form of the weight functions given by Eqs. (3.121) and (3.122). Next, the stability against the ideal MHD motion is determined by the sign of the minimum eigenvalue λ_0 ; if λ_0 is negative, the plasma is unstable. When the plasma is marginally stable, the eigenvalue problem has the null eigenvalue ($\lambda = 0$) with the nontrivial global solution. Furthermore, from the theory of eigenfunctions, we have $\lambda = \delta W_p / \delta W_k$, where both potential and kinetic energies are evaluated by using the eigenfunction corresponding to the eigenvalue λ.

3.5.2 Boundary conditions

When we consider the one-dimensional problem, the correct boundary condition at rational surfaces is the "natural boundary condition" [30]. In this two-dimensional case, to determine the boundary conditions at rational surfaces, let us rewrite Eq. (3.119) in a general quadratic form

$$\mathcal{W}[\boldsymbol{Y}] = \int_0^1 \left\{ \left\langle \frac{d\boldsymbol{Y}}{dr} \left| \mathbf{A} \right| \frac{d\boldsymbol{Y}}{dr} \right\rangle + \left\langle \frac{d\boldsymbol{Y}}{dr} \left| \mathbf{B}^t \right| \boldsymbol{Y} \right\rangle + \left\langle \boldsymbol{Y} \left| \mathbf{B} \right| \frac{d\boldsymbol{Y}}{dr} \right\rangle + \langle \boldsymbol{Y} | \mathbf{C} | \boldsymbol{Y} \rangle \right\}, \tag{3.125}$$

where matrices $\mathbf{A}$, $\mathbf{B}$, and $\mathbf{C}$ have the block matrix structure, and $\mathbf{A}$ and $\mathbf{C}$ are Hermitian. The stationary condition for $\mathcal{W}[\boldsymbol{Y}]$ for the arbitrary variation for $\boldsymbol{Y}$ yields

$$\delta \mathcal{W} = -\int_0^1 \delta \boldsymbol{Y} \cdot \mathcal{N}_\lambda \boldsymbol{Y} dr + \left\langle \delta \boldsymbol{Y} \left| \mathbf{A} \frac{d\boldsymbol{Y}}{dr} + \mathbf{B}^t \boldsymbol{Y} \right\rangle \right|_0^1 = 0, \tag{3.126}$$

where the operation $\mathcal{N}_\lambda$ is written as

$$\mathcal{N}_\lambda \boldsymbol{Y} \equiv \frac{d}{dr}\left(\mathbf{A} \frac{d\boldsymbol{Y}}{dr} \right) + \frac{d}{dr}(\mathbf{B}^t \boldsymbol{Y}) - \mathbf{B} \frac{d\boldsymbol{Y}}{dr} - \mathbf{C}\boldsymbol{Y}, \tag{3.127}$$

and the second term in the RHS of Eq. (3.126) expresses the boundary terms.

By assuming, for simplicity, that only $r = r_m$ is the rational surface, and the fixed boundary condition at $r = 1$ as $\boldsymbol{Y}(1) = 0$, the boundary term becomes

$$\text{boundary term} = \left\langle \delta\boldsymbol{Y} \left| \mathbf{A}\frac{d\boldsymbol{Y}}{dr} + \mathbf{B}^t\boldsymbol{Y} \right\rangle_{r=r_m-0} - \left\langle \delta\boldsymbol{Y} \left| \mathbf{A}\frac{dY}{dr} + \mathbf{B}^t\boldsymbol{Y} \right\rangle_{r=r_m+0}, \right. \tag{3.128}$$

where we have used the regularity condition, Eq. (3.76), at $r = 0$. Since $\delta\boldsymbol{Y}$ is arbitrary, we obtain Eqs. (3.123) and (3.124) and the boundary condition at the rational surface

$$\left[\mathbf{A}\frac{d\boldsymbol{Y}}{dr} + \mathbf{B}^t\boldsymbol{Y}\right]_{r=r_m-0} = \left[\mathbf{A}\frac{d\boldsymbol{Y}}{dr} + \mathbf{B}^t\boldsymbol{Y}\right]_{r=r_m+0}. \tag{3.129}$$

As mentioned in Subsection 3.4.2, an eigenfunction $\boldsymbol{Y}(r)$ around $r = r_m$ is a sum of the singular component $\boldsymbol{Y}^{(s)}(r)$ proportional to the small solution and the analytic component $\boldsymbol{Y}^{(a)}(r)$,

$$\boldsymbol{Y}(r) = \boldsymbol{Y}^{(a)}(r) + \boldsymbol{Y}^{(s)}(r). \tag{3.130}$$

For the analytic component, $\mathbf{A}d\boldsymbol{Y}^{(a)}/dr + \mathbf{B}^t\boldsymbol{Y}^{(a)}$ is continuous and the condition Eq. (3.129) is automatically satisfied. The singular component, on the other hand, are independent across $r = r_m$, and we find that the conditions

$$\left[\mathbf{A}\frac{d\boldsymbol{Y}^{(s)}}{dr} + \mathbf{B}^t\boldsymbol{Y}^{(s)}\right]_{r=r_m-0} = 0, \tag{3.131}$$

$$\left[\mathbf{A}\frac{d\boldsymbol{Y}^{(s)}}{dr} + \mathbf{B}^t\boldsymbol{Y}^{(s)}\right]_{r=r_m+0} = 0, \tag{3.132}$$

are satisfied independently at $r = r_m - 0$ and $r = r_m + 0$.

Since the $l \neq m$ harmonics in the singular component $\boldsymbol{Y}^{(s)}(r)$ begin from the power $x^{1/2+\mu_{mer}}$ for $l \neq 0$, or $x^{3/2+\mu_{mer}}$ for $l = 0$ ($x = r - r_m$), $Y_l(r)$ is continuous at $r = r_m$ for $l \neq m$. Therefore, we can impose at $r = r_m$ the continuous condition for $Y_l(r)$, $l \neq m$, and the natural boundary condition for $Y_m(r)$. These conditions are convenient from the numerical point of view. This is the reason we adopt the Fourier harmonic representation of $\boldsymbol{Y}$.

3.6 Numerical code MARG2D

For realizing the stability analysis of ideal MHD modes on the basis of the analytical model derived in the previous sections, a code MARG2D, which compute the eigenfunction by using the lowest order finite hybrid element method [61], have been developed [29]. In this code, $\boldsymbol{Y}(r)$ and $d\boldsymbol{Y}/dr$ are approximated as

$$\boldsymbol{Y}(r) = \sum_{j=1}^{N} \frac{\boldsymbol{Y}_j + \boldsymbol{Y}_{j+1}}{2} e_{j+1/2}(r), \tag{3.133}$$

$$\frac{d\boldsymbol{Y}}{dr} = \sum_{j=1}^{N} \frac{\boldsymbol{Y}_{j+1} - \boldsymbol{Y}_j}{r_{j+1} - r_j} e_{j+1/2}(r), \tag{3.134}$$

where $\{r_j\}$'s are nodal points in the radial direction, and the element $e_{j+1/2}(r)$ is defined by $e_{j+1/2}(r) = 1$ for $r_j < r < r_{j+1}$, and $e_{j+1/2}(r) = 0$, otherwise. By substituting Eqs. (3.133) and (3.134) into Eqs. (3.80) and (3.81), we obtain a matrix expressing the plasma potential energy integral as follows.

$$\int \left\langle \boldsymbol{Y} \left| \frac{1}{r^2}\mathbf{K} \right| \boldsymbol{Y} \right\rangle dr = \sum_{j=1}^{NR} \left\langle \boldsymbol{Y}_j + \boldsymbol{Y}_{j+1} \left| \mathbf{K}_\Delta \right| \boldsymbol{Y}_j + \boldsymbol{Y}_{j+1} \right\rangle, \tag{3.135}$$

$$\int \left\langle \frac{\partial}{\partial r}\bar{\boldsymbol{Y}} \left| \underline{\bar{\mathbf{D}}}\underline{\bar{\mathbf{L}}}\underline{\bar{\mathbf{D}}} \right| \frac{\partial}{\partial r}\bar{\boldsymbol{Y}} \right\rangle dr = \sum_{j=1}^{NR} \left\langle \bar{\boldsymbol{Y}}_{j+1} - \bar{\boldsymbol{Y}}_j \left| \mathbf{L}_\Delta \right| \bar{\boldsymbol{Y}}_{j+1} - \bar{\boldsymbol{Y}}_j \right\rangle, \tag{3.136}$$

$$\int \left\langle \boldsymbol{Y} \left| \underline{\mathbf{M}}_O\underline{\bar{\mathbf{D}}} \right| \frac{\partial}{\partial r}\bar{\boldsymbol{Y}} \right\rangle dr = \sum_{j=1}^{NR} \left\langle \boldsymbol{Y}_j + \boldsymbol{Y}_{j+1} \left| \mathbf{M}_\Delta \right| \bar{\boldsymbol{Y}}_{j+1} - \bar{\boldsymbol{Y}}_j \right\rangle, \tag{3.137}$$

$$\int \left\langle \frac{\partial}{\partial r}\bar{\boldsymbol{Y}} \left| \underline{\bar{\mathbf{D}}}\,(\underline{\mathbf{M}}_O)^t \right| \boldsymbol{Y} \right\rangle dr = \sum_{j=1}^{NR} \left\langle \bar{\boldsymbol{Y}}_{j+1} - \bar{\boldsymbol{Y}}_j \left| \mathbf{M}_\Delta^t \right| \boldsymbol{Y}_j + \boldsymbol{Y}_{j+1} \right\rangle, \tag{3.138}$$

$$\int \left| \frac{\partial}{\partial r} Y_0 \right|^2 dr = \sum_{j=1}^{NR} \left\langle (Y_0)_{j+1} - (Y_0)_j \left| R_\Delta \right| (Y_0)_{j+1} - (Y_0)_j \right\rangle, \tag{3.139}$$

$$\int \left\langle \bar{\boldsymbol{Y}} \left| -\frac{d}{dr}\underline{\bar{\mathbf{M}}}_H \right| \bar{\boldsymbol{Y}} \right\rangle dr = \sum_{j=1}^{NR} \left\langle \bar{\boldsymbol{Y}}_j + \bar{\boldsymbol{Y}}_{j+1} \left| \mathbf{dM}_\Delta \right| \bar{\boldsymbol{Y}}_j + \bar{\boldsymbol{Y}}_{j+1} \right\rangle, \tag{3.140}$$

where NR is the is the mesh number in the radial direction,

$$\mathbf{K}_\Delta = \frac{\mathbf{K}(r_{j+1/2})}{4r_{j+1/2}^2}\Delta r_{j+1/2}, \tag{3.141}$$

$$\mathbf{L}_\Delta = \frac{\underline{\bar{\mathbf{D}}}(r_{j+1/2})\underline{\bar{\mathbf{L}}}(r_{j+1/2})\underline{\bar{\mathbf{D}}}(r_{j+1/2})}{\Delta r_{j+1/2}}, \tag{3.142}$$

$$\mathbf{M}_\Delta = \frac{\underline{\mathbf{M}}_O(r_{j+1/2})\underline{\bar{\mathbf{D}}}(r_{j+1/2})}{2}, \tag{3.143}$$

$$\mathbf{M}_\Delta^t = \frac{\underline{\bar{\mathbf{D}}}(r_{j+1/2})\left(\underline{\mathbf{M}}_O(r_{j+1/2})\right)^t}{2}, \tag{3.144}$$

$$R_\Delta = \frac{1}{\Delta_{j+1/2}}, \tag{3.145}$$

$$\mathbf{dM}_\Delta = \frac{\Delta r_{j+1/2}}{4}\left(\frac{d}{dr}\underline{\bar{\mathbf{M}}}_H\right)_{r=r_{j+1/2}}, \tag{3.146}$$

and

$$r_{j+1/2} = \frac{r_j + r_{j+1}}{2}, \tag{3.147}$$

$$\Delta r_{j+1/2} = r_{j+1} - r_j. \tag{3.148}$$

The surface term in Eq. (3.82) is already expressed in a matrix form, and the kinetic energy integral in Eq. (3.120) can be written as

$$\delta W_k = 2\pi^2\lambda \sum_m \sum_{j=1}^{NR} \left\langle (Y_j)_m + (Y_{j+1})_m \,|(Q_m)_\Delta|\, (Y_j)_m + (Y_{j+1})_m \right\rangle \tag{3.149}$$

$$= 2\pi^2\lambda \sum_{j=1}^{NR} \left\langle \boldsymbol{Y}_j + \boldsymbol{Y}_{j+1} \,|\mathbf{Q}_\Delta|\, \boldsymbol{Y}_j + \boldsymbol{Y}_{j+1} \right\rangle, \tag{3.150}$$

where

$$(Q_\Delta)_{m,m} = \frac{\rho_m(r_{j+1/2})}{4}\Delta r_{j+1/2}. \tag{3.151}$$

By introducing the vector

$$\boldsymbol{\Xi} = \begin{pmatrix} \boldsymbol{Y}_{-MM} \\ \boldsymbol{Y}_{-MM+1} \\ \vdots \\ \boldsymbol{Y}_{MM-1} \\ \boldsymbol{Y}_{MM} \end{pmatrix} = \begin{pmatrix} (Y_1)_{-MM} \\ (Y_1)_{-MM+1} \\ (Y_1)_{-MM+2} \vdots \\ \vdots \\ (Y_{NR+1})_{MM-2} \\ (Y_{NR+1})_{MM-1} \\ (Y_{NR+1})_{MM} \end{pmatrix}, \tag{3.152}$$

where MM is the maximum poloidal mode number to be considered, we derive the generalized eigenvalue problem in a matrix form as

$$\mathbf{A}_{W_p}\boldsymbol{\Xi} = \lambda \mathbf{B}_{W_k}\boldsymbol{\Xi}. \tag{3.153}$$

Here the matrices $\mathbf{A}_{W_p}$ and $\mathbf{B}_{W_k}$ are obtained with Eqs. (3.135)-(3.146) and Eqs. (3.150) and (3.151), respectively. The numerical numerical method to solve the eigenvalue problem Eq. (3.153) is a direct method with the LU factorization and the inverse iteration method [62].

3.7 Application to the theory for the external mode analysis

In the previous sections, we formulated the eigenvalue problem associated with the two-dimensional Newcomb equation Eqs. (3.123) and (3.124), and the sign of the minimum eigenvalue determines the stability of a plasma with the fixed boundary condition at the plasma surface. With the relation Eq. (2.62), this eigenvalue problem can be extended for the external mode analysis by calculating the vacuum energy contribution δW_V; two methods for obtaining such a vacuum contribution will be introduced in Section 4.2, Appendix C and Chapter 5.

For analyzing the external mode stability, a theory for the stability analysis of external MHD modes in a tokamak is developed by using the property of the Newcomb equation.

In this section, we formulate the method based on this theory, called the stability matrix method.

The bilinear form for ideal MHD motion with Eq. (3.125) and the contribution from the vacuum region is written as

$$W[\boldsymbol{\xi},\boldsymbol{\eta}] = W_p[\boldsymbol{\xi},\boldsymbol{\eta}] + \langle \boldsymbol{\xi}_a|\mathbf{M}_V|\boldsymbol{\eta}_a\rangle, \tag{3.154}$$

where $\boldsymbol{\xi}_a = \boldsymbol{\xi}(a)$,

$$W_p[\boldsymbol{\xi},\boldsymbol{\eta}] = \int_0^a \mathcal{L}[\boldsymbol{\xi},\boldsymbol{\eta}]dr, \tag{3.155}$$

$$\mathcal{L}[\boldsymbol{\xi},\boldsymbol{\eta}] = \left\langle \frac{d\boldsymbol{\xi}}{dr}|\mathbf{L}|\frac{d\boldsymbol{\eta}}{dr}\right\rangle + \langle\boldsymbol{\xi}|\mathbf{K}|\boldsymbol{\eta}\rangle + \left\langle \frac{d\boldsymbol{\xi}}{dr}|\mathbf{M}^t|\boldsymbol{\eta}\right\rangle + \left\langle \boldsymbol{\xi}|\mathbf{M}|\frac{d\boldsymbol{\eta}}{dr}\right\rangle, \tag{3.156}$$

and the matrix $\mathbf{M}_V$ stands for the contribution from the vacuum region. Let us notice that in Eq. (3.156)

$$\frac{d\xi_j}{dr}(L)_{j,k}\frac{d\eta_k}{dr} = \frac{d}{dr}\left[\xi_j(L)_{j,k}\frac{d\eta_k}{dr}\right] - \xi_j\frac{d}{dr}\left[(L)_{j,k}\frac{d\eta_k}{dr}\right], \tag{3.157}$$

and

$$\frac{d\xi_j}{dr}(M^t)_{j,k}\eta_k = \frac{d}{dr}\left[\xi_j(M^t)_{j,k}\eta_k\right] - \xi_j\frac{d}{dr}\left[(M^t)_{j,k}\eta_k\right]. \tag{3.158}$$

Let $S = \{\boldsymbol{\xi} \mid \mathcal{N}\boldsymbol{\xi} = 0\}$ be a set of functions that satisfy the Newcomb equation. By using Eqs. (3.157) and (3.158) and the integration by part in Eq. (3.155), we have for $\boldsymbol{\xi}(r), \boldsymbol{\eta}(r) \in S$

$$W_p[\boldsymbol{\xi},\boldsymbol{\eta}] = \langle\boldsymbol{\xi}_a|\mathbf{M}_H|\boldsymbol{\eta}_a\rangle + \frac{1}{2}\left\langle\boldsymbol{\xi}_a|\mathbf{L}|\frac{d\boldsymbol{\eta}_a}{dr}\right\rangle + \frac{1}{2}\left\langle\frac{d\boldsymbol{\xi}_a}{dr}|\mathbf{L}|\boldsymbol{\eta}_a\right\rangle, \tag{3.159}$$

$$\mathbf{M}_H := \frac{1}{2}(\mathbf{M} + \mathbf{M}^t). \tag{3.160}$$

Therefore, the bilinear form of the ideal plasma motion that satisfies the Newcomb equation can be expressed in terms of the boundary values of the displacement. Next, let $\boldsymbol{Y}^m(r)$ be a vector function ($m = 0, \pm1, \cdots, \pm L_f$)

$$\boldsymbol{Y}^m(r) = (Y^m_{-L_f}(r), \cdots, Y^m_{L_f}(r))^t, \tag{3.161}$$

where each poloidal harmonic $Y^m_l(r)$ satisfies the condition

$$Y^m_l(a) = 0 \quad (l \neq m), \qquad Y^m_m(a) = 1, \tag{3.162}$$

for $l = 0, \pm1, \cdots, \pm L_f$. The set $\{\boldsymbol{Y}^m(r)\}$ forms a basis for external modes [10]; any external mode can be expressed by using a set of real numbers $\{x_m\}$ as

$$\boldsymbol{\xi}(r) = \sum_m x_m \boldsymbol{Y}^m(r). \tag{3.163}$$

Let us notice that $\xi_m(a) = x_m$ for the $m-$th poloidal Fourier harmonics of $\boldsymbol{\xi}(r)$. The change of the potential energy due to the mode $\boldsymbol{\xi}$ is given by the quadratic form of the vector $\boldsymbol{x}$,

$$W[\boldsymbol{\xi}, \boldsymbol{\xi}] = \langle \boldsymbol{x}|\mathbf{A}|\boldsymbol{x}\rangle, \tag{3.164}$$

where the matrix $\mathbf{A}$ is given by

$$\mathbf{A} = \mathbf{M}_p + \mathbf{M}_V, \tag{3.165}$$

$$\left(M_p\right)_{l,m} = W_p[\boldsymbol{Y}^l, \boldsymbol{Y}^m]. \tag{3.166}$$

The matrix $\mathbf{A}$ is real and symmetric for an equilibrium with the mirror symmetry. We call in the present paper $\mathbf{A}$ *the stability matrix* for external modes. The stability of external modes is clarified by solving the eigenvalue problem

$$\mathbf{A}\boldsymbol{x} = \mu \boldsymbol{x}, \tag{3.167}$$

where μ denotes the eigenvalue of $\mathbf{A}$; this is to emphasize the difference between the eigenvalue problem Eqs. (3.123) and (3.124), the eigenvalue is defined as λ, and that Eq. (3.167). If the minimum eigenvalue of $\mathbf{A}$ is negative, then the plasma is unstable against ideal external kink modes. The stability matrix $\mathbf{A}$ also plays an indispensable role in the stability for resistive wall modes [10].

The basis $\boldsymbol{Y}^m(r)$ can be constructed by using the response formalism [30]. Let us write $\boldsymbol{Y}^m(r)$ as

$$\boldsymbol{Y}^m(r) = \boldsymbol{X}^m(r) + \boldsymbol{Z}^m(r), \tag{3.168}$$

where $\boldsymbol{Z}^m(r)$ given analytically satisfies the inhomogeneous boundary condition Eq. (3.162). Consequently, we have an inhomogeneous equation for $\boldsymbol{X}^m(r)$ with the homogeneous boundary condition [63]

$$\mathcal{N}\boldsymbol{X}^m(r) = -\mathcal{N}\boldsymbol{Z}^m(r), \quad \boldsymbol{X}^m(a) = 0. \tag{3.169}$$

Since Eq. (3.169) can be solved by the MARG2D code, we can construct the basis $\{\boldsymbol{Y}^m(r)\}$ and the stability matrix $\mathbf{A}$.

On solving Eq. (3.169), the same boundary condition with the eigenvalue problem Eqs. (3.123) and (3.124) is imposed at the rational surfaces. Also the matrix $\mathbf{M}_V$ is computed under the assumption of no wall limit or ideal conducting wall. Those conditions guarantee the Hermitian property of the stability matrix $\mathbf{A}$. However, if the plasma surface coincides *exactly* with the rational surface, an eigenvalue problem cannot be constructed for an external kink mode within the present formulation. This aspect is similar to the ERATOJ code.

The MARG2D-SM code realizes the analysis of the external mode stability with the stability matrix. In this code, the inhomogeneous equation Eq. (3.169) is numerically solved with the LU factorization, and the eigenvalue problem Eq. (3.167) is solved with the QR algorithm for real Hessenberg matrices [62].

Chapter 4

Application of the two-dimensional Newcomb equation to compute the stability matrix of external MHD modes in tokamaks

4.1 Introduction

The Newcomb equation, the inertia free linear ideal MHD equation [27,28], plays fundamental roles in the MHD stability theory, as mentioned in Chapter 3. A code MARG2D [29] has been developed which solves numerically the two-dimensional Newcomb equation and the associated eigenvalue problem by a finite element method [30, 32]. We can know the ideal MHD stability of the plasma from the sign of the eigenvalue λ; if λ be positive (negative), then the plasma is stable (unstable) against ideal MHD perturbations.

I also have introduced in Section 3.7 the application of the theory of the Newcomb equation to the stability analysis of external modes in a tokamak. In this application, a matrix method has been developed by using the property of the Newcomb equation to express the change of the potential energy due to the plasma displacement by a quadratic form (a matrix form) with respect to the values of the displacement at the plasma surface [10].

In this chapter, I execute the benchmark tests of the MARG2D-SM code, which realizes the external mode analysis with the stability matrix, by comparing the ERATOJ code in several cases. After confirming the validity of the stability matrix method, we study comprehensively the spectral structure of ideal external modes, stable or unstable, by using the newly developed method.

The formulation introduced in Section 3.7 is indispensable for the analysis of the resistive wall modes (RWMs) and a code DCON has already reported [13]. However, if the matrix

method be combined with the eigenvalue problem associated with the original Newcomb equation in the MARG2D code, the MARG2D-SM code enables us to get deeper insight into the spectral properties of the external modes. These MARG2D and MARG2D-SM codes clarify the effects of stable internal modes in a highβ plasma on the properties of the external modes. Among such effects, the stable internal modes can destabilize external modes and change the surface mode structure of external modes into a global mode structure when the internal modes approach to their marginal stability. The code also elucidates the difference of the spectral properties between a normal shear tokamak and a reversed shear tokamak. These spectral properties of ideal external modes not only are interesting by themselves but also will be useful in the study of RWMs.

With the benefits of this MARG2D-SM code, the facility and the short computation time for identifying the marginal stability, I apply this code to analyze an effect of the aspect ratio on an external kink-ballooning stability, which attracts attention recently in the design research on high-performance tokamaks.

In Section 4.2, I show benchmark tests of the present formulation with ERATOJ code [32] (the JAERI version of the ERATO code). After confirming the validity of the MARG2D-SM code, the spectral properties of external modes are investigated in Section 4.3. In Section 4.4 we study, numerically and analytically, the coupling between external modes and internal modes by using the stability matrix method together with the associated eigenvalue problem for internal modes. An effect of the aspect ratio on the stability of ideal external kink-ballooning modes is investigated in Section 4.5. Summary of the present work is given in Section 4.6.

4.2 Benchmark test of MARG2D code

We execute benchmark tests among the method that solves Eq. (3.167) with the stability matrix (SM) by the MARG2D-SM code, that solving the eigenvalue problem associated with the Newcomb equation

$$\mathcal{N}\boldsymbol{\xi} = -\lambda \mathrm{Diag}(\rho(r))\boldsymbol{\xi}, \tag{4.1}$$

with the free boundary condition(EV) by the MARG2D code, and the ERATOJ code [32]. Here this eigenvalue problem Eq. (4.1) and the numerical codes MARG2D and MARG2D-SM are introduced in Chapter 3.

The Equilibria used in benchmark tests have circular cross sections with the aspect ratio $A = 3.30$; they are obtained by solving Grad-Shafranov equation numerically [48]. Figure 4.1 shows the contour of $\psi = const.$, and the profiles of the pressure $p(s)$ and the safety factor $q(s)$ $(s = \sqrt{\psi})$ with the poloidal beta $\beta_p = 0.01$; it is defined in Eq. (2.33). The safety factor at the magnetic axis q_0 and that at the plasma surface q_a are 1.32 and 2.80.

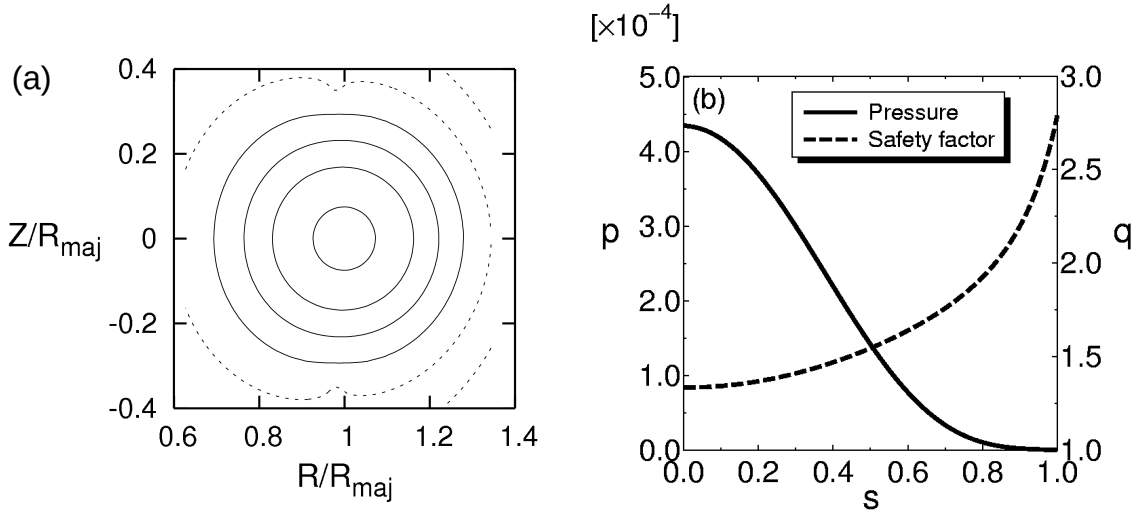

Figure 4.1: Equilibrium for benchmark tests when $\beta_p = 0.01$. (a) Contours of ψ (magnetic surfaces). Solid lines are for $\psi \leq 0$ (plasma region), and the broken lines are for $\psi > 0$ (vacuum region). The outermost solid line shows the plasma surface. (b) Profiles of the pressure p and the safety factor q ($s = \sqrt{\psi}$). The values of the safety factor at the magnetic axis q_0 and that at the plasma surface q_a are 1.32 and 2.80, respectively.

We first investigate the stability of $n = 1$ ideal external kink modes in the (q_a, μ) plane, where μ is the eigenvalue of the stability matrix. A series of equilibria $(\tilde{\psi}, \tilde{p}, \tilde{F})$ is obtained from the known equilibrium (ψ, p, F), as shown in Fig. 4.1, by the scaling with the parameter σ,

$$\tilde{\psi} = \sigma\psi, \tag{4.2}$$

$$\tilde{p}(\tilde{\psi}) = \sigma^2 p(\psi), \tag{4.3}$$

$$\tilde{F}^2(\tilde{\psi}) - \tilde{F}^2(\tilde{\psi}_0) = \sigma^2 \left[F^2(\psi) - F^2(\psi_0)\right], \tag{4.4}$$

where ψ_0 is the poloidal flux function at the magnetic axis. The safety factor q is scaled as

$$\tilde{q}(\tilde{\psi}) = \frac{1}{\sigma}\frac{\tilde{F}(\tilde{\psi})}{F(\psi)} q(\psi), \tag{4.5}$$

however, since $\tilde{I}_p$ changes as $\tilde{I}_p = \sigma I_p$, β_p is unchanged by this scaling. In this article, each equilibrium has no current density on the plasma surface.

The mesh numbers in both the MARG2D codes and the ERATOJ code are determined by confirming the convergence of the eigenvalues. Since the ERATOJ code is based on the two-dimensional finite element method with the lowest order elements, this code needs at least four times mesh numbers in the poloidal direction as many as the MARG2D codes, based

on the Fourier harmonics in the poloidal direction. On the other hand, in the radial direction, the MARG2D codes needs many mesh numbers near each rational surface to meet the convergence. In this paper, the radial mesh number $NPSI_{M2D} = 1200$ and the maximum poloidal mode number $M_{M2D} = 32$ are set for both the MARG2D codes, and the radial mesh number $NPSI_{ERT} = 500$ and the mesh number in the poloidal direction $NCHI_{ERT} = 256$ are used for ERATOJ.

In both the MARG2D and the ERATOJ codes, the matrix representing the vacuum contribution, $\mathbf{M}_V$ in Eq. (3.154), is calculated by using a Green's function of the scalar potential for the perturbation of magnetic fields in the vacuum [32, 64] with no wall limit assumption. The Calculation with a Green's function technique is demonstrated in Appendix C.

Figure 4.2 shows the dependence of the minimum eigenvalues on q_a; this expresses the stability of the ideal external mode in the $A = 3.30$ and $\beta_p = 0.01$ equilibria. The solid line denotes the minimum eigenvalues of SM μ_0, the dashed line shows those obtained by EV λ_{0-M2D}, and the dotted line is for those calculated by ERATOJ λ_{0-ERT}, respectively. Ideal external modes are marginally stable when the minimum eigenvalue equals to zero. From this figure, q_{a-mgl} which are the q_a values when ideal external modes are marginally stable are obtained by the SM method as $q_{a-mgl} = 2.66$ and 3.00, which well agree with those obtained by EV and ERATOJ.

We also compare the eigenfunctions belonging to the minimum eigenvalues when $q_a = 2.67$ which is close to q_{a-mgl}; each minimum eigenvalue is negative. As shown in Fig. 4.3, each poloidal Fourier harmonic of these eigenfunctions obtained by (a) SM, (b) EV, and (c) ERATOJ is similar to each other. These show surface modes with the dominant harmonic $l = 3$; it is a well-known feature of $m \geq 2$ ideal external kink modes in low-β_p tokamaks [65]. The harmonics $l = 2$ and $l = 4$ are excited by the poloidal mode coupling with the harmonic $l = 3$. While the harmonic $l = 2$ computed by the ERATOJ code is smooth at $q = 2$ rational surface ($s = 0.85$), this harmonic obtained by the MARG2D codes is discontinuous at $r = 0.81$, which is the feature of the MARG2D formulation explained in the previous sections.

A next benchmark test is executed in the $\beta_p = 0.80$ equilibria, whose p and q profiles when $\sigma = 1$ are shown in Fig. 4.4. The values of q_0 and q_a are 1.30 and 2.80, respectively. Figure 4.5 shows the dependence of the minimum eigenvalues on q_a. The q_{a-mgl} value is obtained by the SM method as $q_{a-mgl} = 4.28$, and also well agrees with those obtained by other methods. The dependences of the minimum eigenvalues on q_a revealed by these three methods are convex downward between $q_a = 3.00$ and $q_a = q_{a-mgl} = 4.28$. The poloidal Fourier harmonics of the eigenfunctions belonging to the minimum eigenvalues when $q_a = 4.27$, that is close to q_{a-mgl}, are shown in Fig. 4.6. These Fourier harmonics obtained by (a) SM, (b) EV, and (c) ERATOJ are also almost same each other, and have global mode structures.

The q_a dependence of μ_0 and structures of the eigenfunctions are different from those in the low-β_p case in figures Figs. 4.2 and 4.3, and it seems that only the poloidal mode coupling

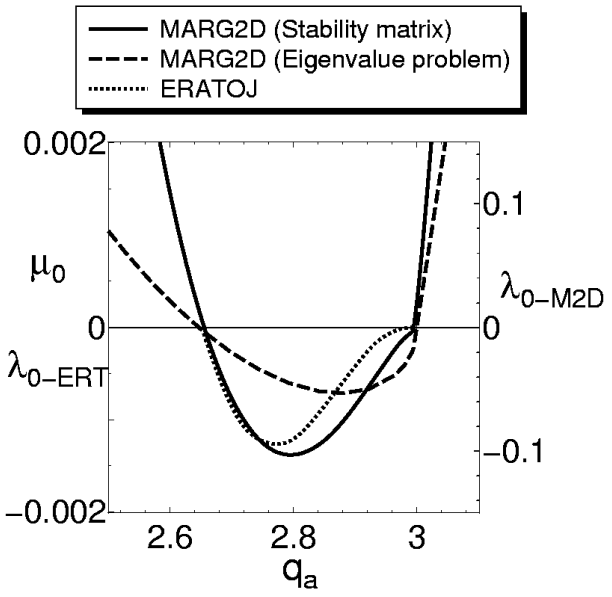

Figure 4.2: Dependence of the minimum eigenvalues on q_a when $\beta_p = 0.01$. The label μ_0 denotes the minimum eigenvalue of the stability matrix (SM), λ_{0-M2D} is that obtained by solving Eq. (4.1) with the free boundary condition (EV), and λ_{0-ERT} is that calculated by ERATOJ, respectively. The marginally stable q_a values are clarified by SM as $q_{a-mgl} = 2.66$ and 3.00, and are identical to those obtained by EV and ERATOJ.

will not explain the causes of such differences. These are the next topics discussed in Sections 4.3 and 4.4.

4.3 Spectral structure of external modes in tokamaks

The stability matrix **A** given by Eq. (3.165) should possess the all properties of external modes even when these modes are stable. Among them, an interesting property is the intersection of the eigenvalues of the modes in tokamaks [33, 65]. Here we investigate numerically such a spectral structure of the external modes by using the stability matrix.

Reference [33] has shown that the spectral structure, in particular, the intersection of the eigenvalues, is strongly affected by both the aspect ratio A and the current poloidal beta β_p. Consequently, we make three kinds of equilibria whose A and β_p are different from each other. One is the $A = 100$ and $\beta_p = 0.01$ equilibrium (EQ-1), and the second is the $A = 3.30$ and $\beta_p = 0.01$ equilibrium (EQ-2); p and q of these equilibria are shown in Fig. 4.7. The values of q_0 and q_a in the EQ-1 case are 1.32 and 2.80, respectively. The last one is the $A = 3.30$ and $\beta_p = 0.80$ equilibrium, already shown in Fig. 4.4 (EQ-3). Each equilibrium has circular

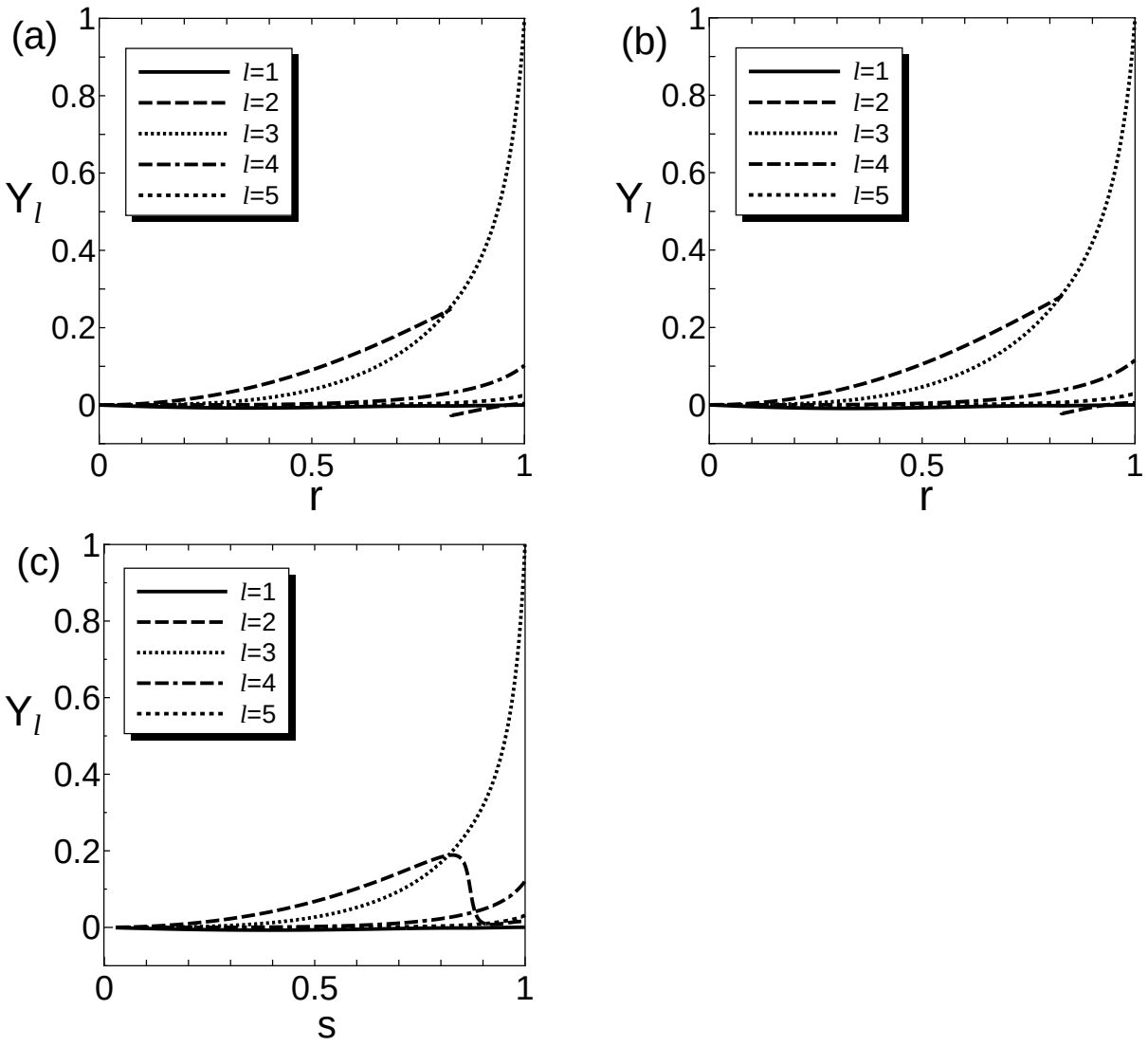

Figure 4.3: Poloidal Fourier harmonics of the eigenfunctions belonging to the minimum eigenvalues when $\beta_p = 0.01$ and $q_a = 2.67$. These are obtained by (a) SM, (b) EV, and (c) ERATOJ. The harmonics Y_l obtained by three methods are similar to each other, and these show typical surface modes with the dominant harmonic $l = 3$. The harmonic $l = 2$ computed by the MARG2D codes is discontinuous at $q = 2$ rational surface ($r = 0.81$) while this harmonic obtained by ERATOJ is smooth at $s = 0.85$.

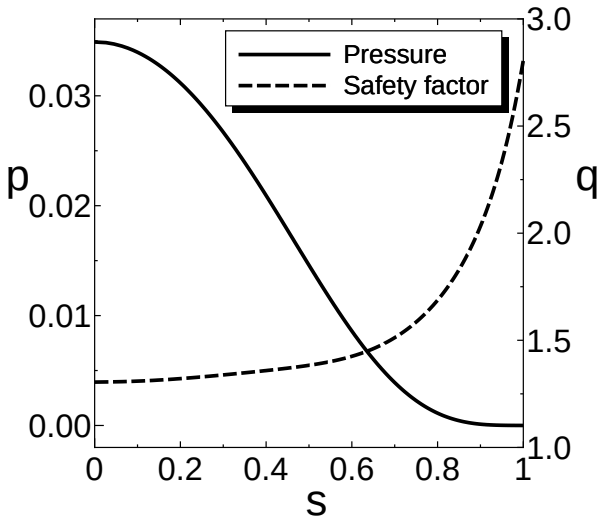

Figure 4.4: Profiles of the pressure p and the safety factor q of the $\beta_p = 0.80$ equilibrium. The values of q_0 and q_a are 1.30 and 2.80, respectively. The magnetic surfaces of this equilibrium are circular.

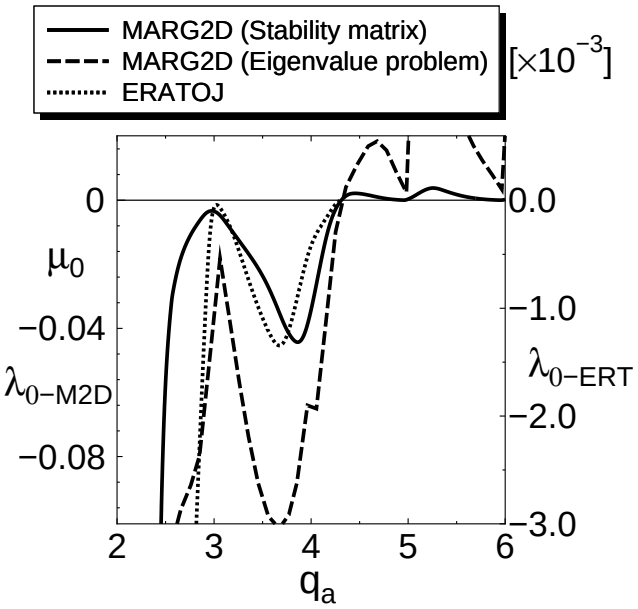

Figure 4.5: Dependence of the minimum eigenvalues on q_a when $\beta_p = 0.80$. The marginally stable q_a values obtained by three methods are identical with each other as $q_{a-mgl} = 4.28$. The behaviors of the q_a dependence of the minimum eigenvalues are convex downward and are similar to each other between $q_a = 3.00$ and $q_a = q_{a-mgl} = 4.28$.

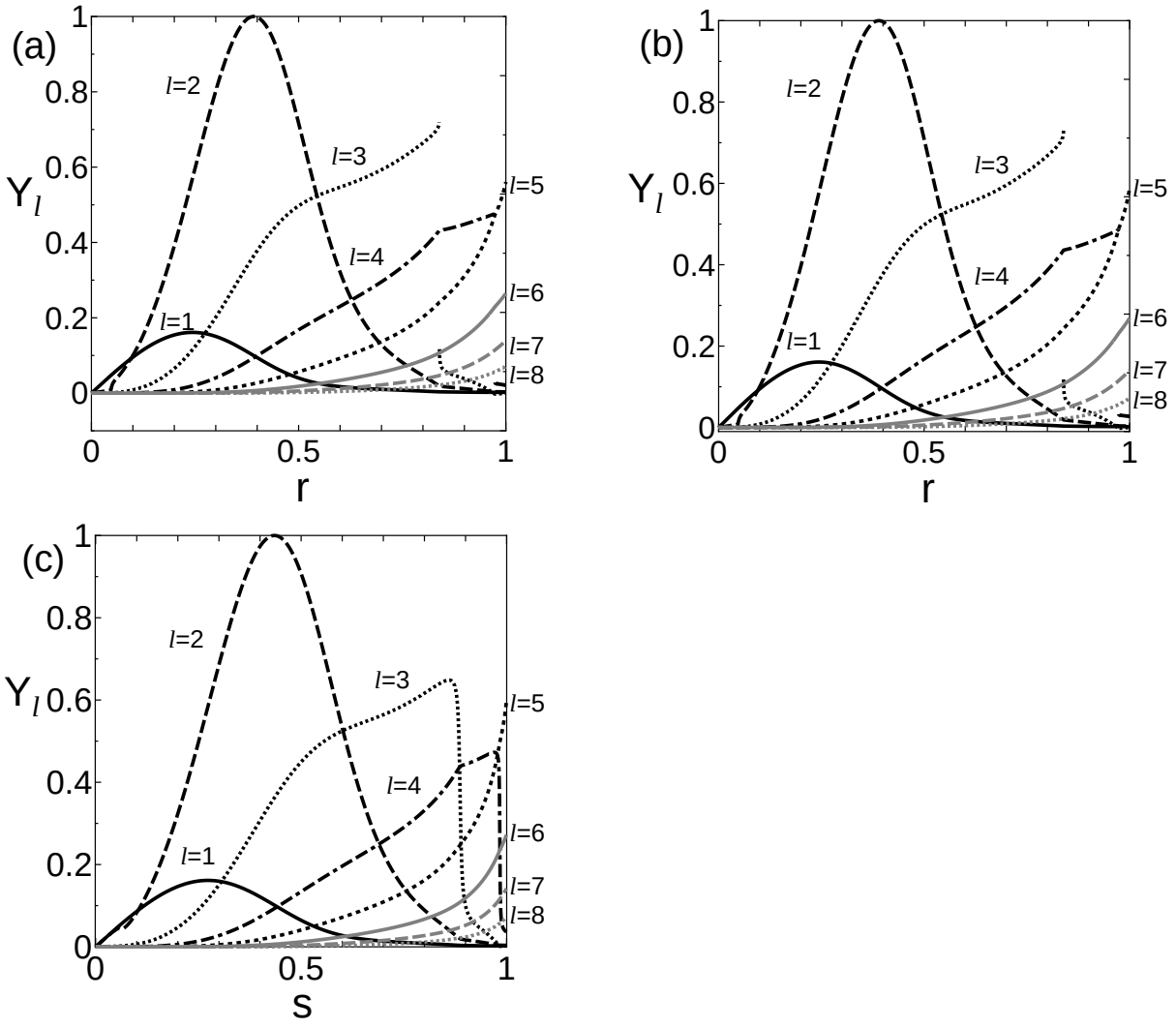

Figure 4.6: Poloidal Fourier harmonics of the eigenfunctions belonging to the minimum eigenvalues when $\beta_p = 0.80$ and $q_a = 4.27$. These are obtained by (a) SM, (b) EV, and (c) ERATOJ, which are similar to each other, and have global mode structures unlike the eigenfunctions in the low-β_p case in Fig. 4.3.

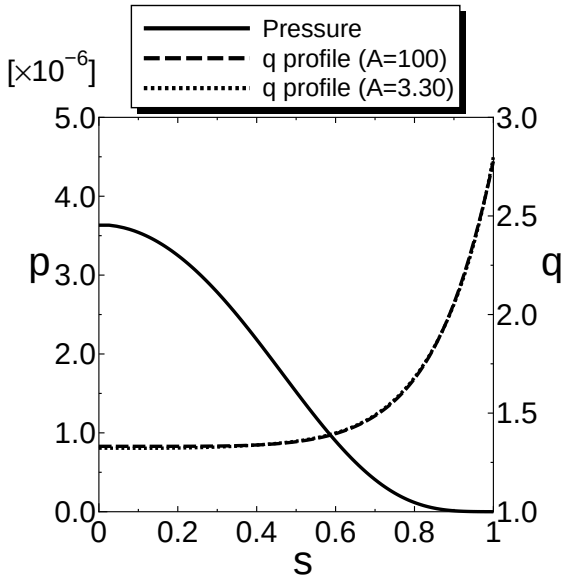

Figure 4.7: Profiles of the pressure p and the safety factor q of the $A = 100$ equilibrium and those of the $A = 3.30$ one. The p profile and β_p are same for both cases ($\beta_p = 0.01$). The q profiles are shown with the dashed line ($A = 100$) and the dotted line ($A = 3.30$). The values of q_0 and q_a are 1.32 and 2.80, respectively. The magnetic surfaces of this equilibrium are circular.

cross sections. The q profile is scaled as Eq. (4.5), and the vacuum contribution is calculated by assuming no wall limit.

Figure 4.8(a) shows the q_a dependence of the eigenvalues, called the spectral structure, in the EQ-1 case. The solid line, the dashed line, the dotted line, the dot-2dashed line, and the short-dotted line, denote the minimum, the second, the third, the fourth, and the fifth eigenvalues, respectively. The i-th ($i = 2, 3, ...$) eigenvalue intersects the $i \pm 1$-th eigenvalues in the stable region $\mu > 0$. For example, in Fig. 4.8(b) that is the enlargement of Fig. 4.8(a) in $4.50 \leq q_a \leq 6.00$, the minimum eigenvalue intersects the second eigenvalue between $q_a = 5.15$ and 5.40.

The meaning of the spectral intersection can be understood from the poloidal Fourier harmonics of the eigenfunctions. Figure 4.9(a) shows the poloidal Fourier harmonics of the eigenfunction belonging to the minimum eigenvalue (EF_{min}) when $q_a = 5.15$ and the dominant harmonic of this eigenfunction is $l = 5$; Fig. 4.9(b) shows those of the eigenfunction belonging to the second eigenvalue (EF_{second}) when $q_a = 5.15$ and the dominant harmonic of this eigenfunction is $l = 6$. On the other hand, when $q_a = 5.40$, just after the intersection point, the dominant harmonic of EF_{min} shown in Fig. 4.9(c) is $l = 6$, and that of EF_{second} in Fig. 4.9(d) is $l = 5$. From these figures, we see the exchange of the eigenfunction belonging to the

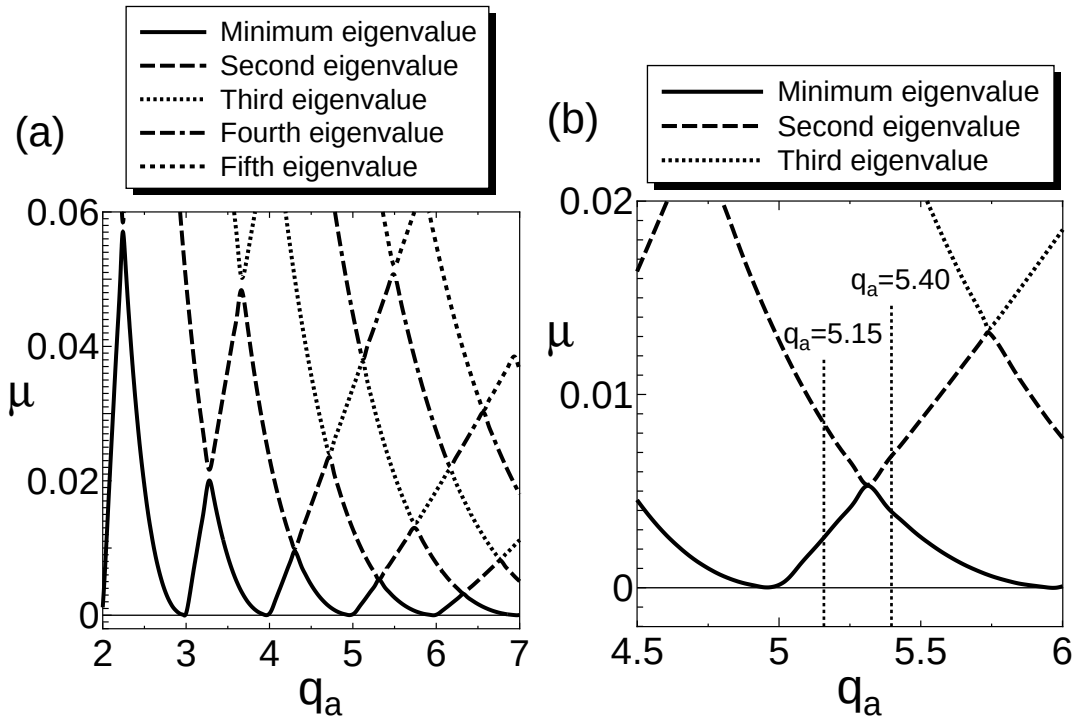

Figure 4.8: (a) Spectral structure of $n = 1$ ideal external kink modes in the $A = 100$ and $\beta_p = 0.01$ equilibria. (b) Expansion of figure (a) in $4.50 \leq q_a \leq 6.00$. The analysis with the stability matrix reveals the spectral structure of external modes when these modes are stable. The i-th eigenvalue intersects the $(i \pm 1)$-th eigenvalues in the stable region, $\mu > 0$ $(i = 2, 3, ...)$.

i-th eigenvalue for that belonging to the $i + 1$-th or $i - 1$-th eigenvalue induces the spectral intersection.

Next, the spectral structure in the EQ-2 case $(A = 3.30, \beta_p = 0.01)$ is shown in Fig. 4.10(a). Unlike in the EQ-1 case, we see gaps at the intersection between the i-th eigenvalue and the $i \pm 1$ eigenvalues; we call them the spectral gaps. We look at the spectral gap between $q_a = 5.15$ and $q_a = 5.40$ in Fig. 4.10(b), the enlargement of Fig. 4.10(a) in $4.50 \leq q_a \leq 6.00$. The poloidal Fourier harmonics of the eigenfunctions are shown in Fig. 4.11. EF_{min} when $q_a = 5.15$, whose dominant harmonic is $l = 5$, changes to EF_{second} as q_a increases to 5.40, and EF_{second} when $q_a = 5.15$, whose dominant harmonic is $l = 6$, becomes EF_{min} as q_a becomes larger to 5.40. We also observe a difference between the case of $A = 100$ and that of $A = 3.30$. In the $A = 3.30$ case, the dominant harmonics of these eigenfunctions excite the neighbor harmonics; especially the eigenfunctions whose dominant harmonic is $l = 6$, shown in figures 4.11(b) and 4.11(c), accompany the harmonics $l = 4$, 5, and 7. The poloidal couplings originated from the finite aspect ratio effect induce these harmonics, and are thought to make the spectral gaps in the

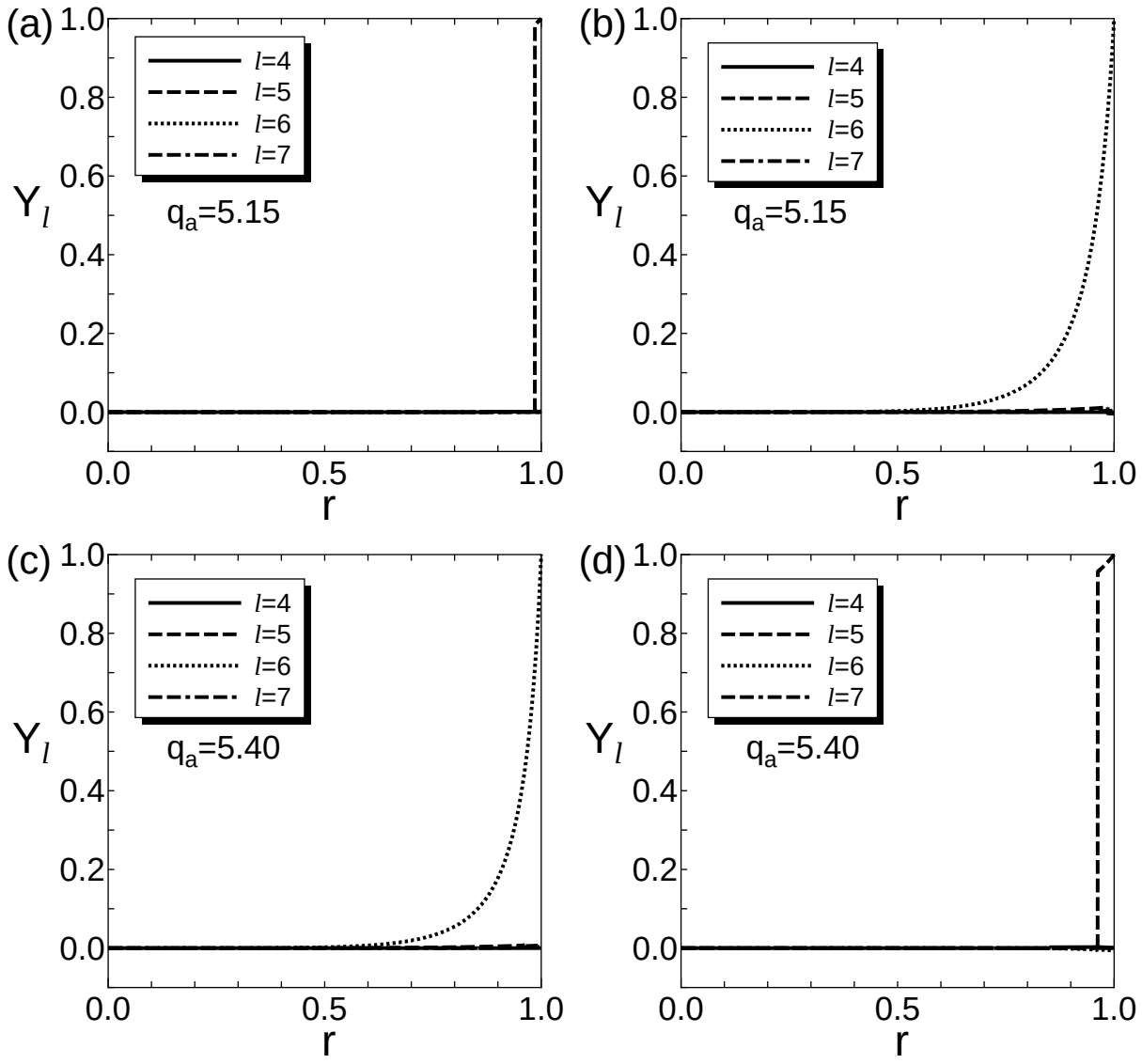

Figure 4.9: Poloidal Fourier harmonics of the eigenfunction when $A = 100$ and $\beta_p = 0.01$. (a) The eigenfunction belonging to the minimum eigenvalue and (b) that belonging to the second eigenvalue when $q_a = 5.15$. (c) The eigenfunction belonging to the minimum eigenvalue and (d) that belonging to the second eigenvalues when $q_a = 5.40$. The eigenfunction, whose dominant harmonic is $l = 5$, changes from the eigenfunction belonging to the minimum eigenvalue to that belonging to the second eigenvalue as q_a increases from 5.15 to 5.40. On the other hand, the eigenfunction belonging to the second eigenvalue when $q_a = 5.15$, whose dominant harmonic is $l = 6$, becomes the eigenfunction belonging to the minimum eigenfunction when $q_a = 5.40$.

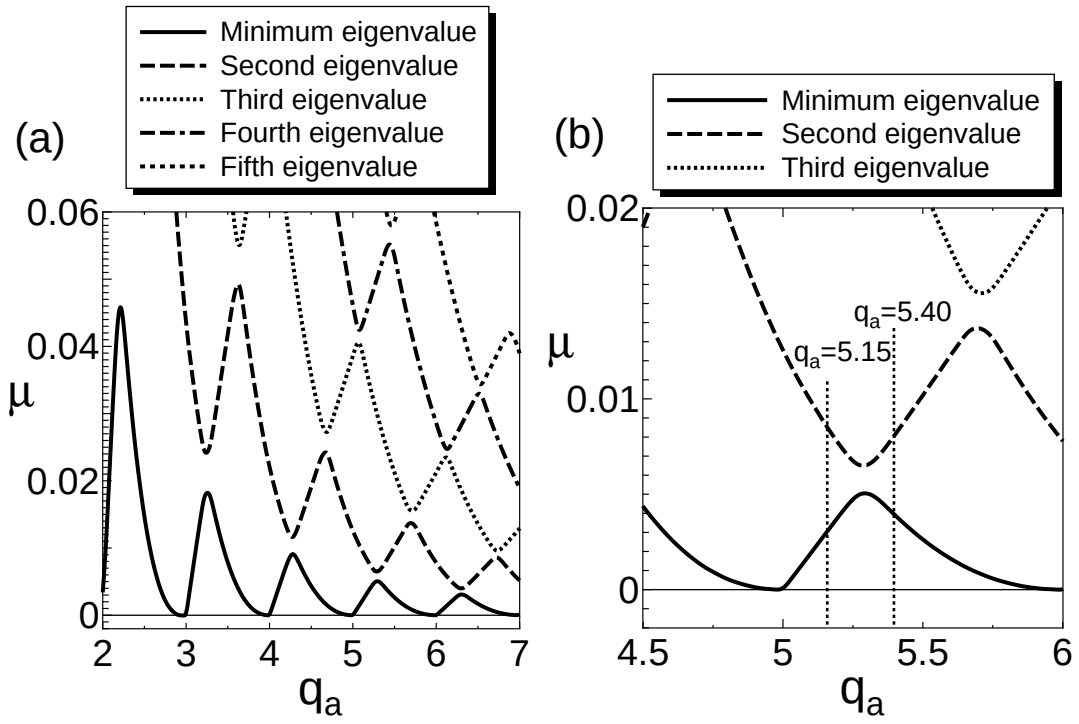

Figure 4.10: (a) Spectral structure of $n = 1$ external kink modes in the $A = 3.30$ and $\beta_p = 0.01$ equilibria. (b) Expansion of figure (a) in $4.50 \leq q_a \leq 6.00$. Spectrum gaps are generated at the spectral intersection points.

spectral structure [33].

We show in Fig. 4.12(a) the spectral structure in the EQ-3 case ($\beta_p = 0.80$). The spectral gaps become wider than those in the EQ-2 case. This is because of increase in β_p, and this effect of β_p is consistent with the analysis in [33]. However, we observe that the structure is qualitatively different from the previous $\beta_p = 0.01$ cases. The minimum eigenvalue becomes negative (unstable) in the region $q_a \leq 4.28$; this feature is already seen in Fig. 4.5.

To reveal the β_p effect in detail, we focus on the region for $5.15 \leq q_a \leq 5.40$ shown in Fig. 4.12(b), the enlargement of Fig. 4.12(a) in $4.50 \leq q_a \leq 6.00$ as in the previous cases. Figure 4.13 shows EF_{min} and EF_{second} when $q_a = 5.15$ and $q_a = 5.40$, respectively. Although, the mode structures become more complicated than those in the low β_p cases, we see the $l = 5$ and 6 harmonics in EF_{min} and EF_{second} exchange for each other as q_a increases from 5.15 to 5.40. However, each eigenfunction has the global mode structure whose $l = 3$ harmonic is strongly excited. This suggests that the finite β_p effect induces, as well as the well-known poloidal coupling as in the EQ-2 case, another coupling between external modes and internal modes.

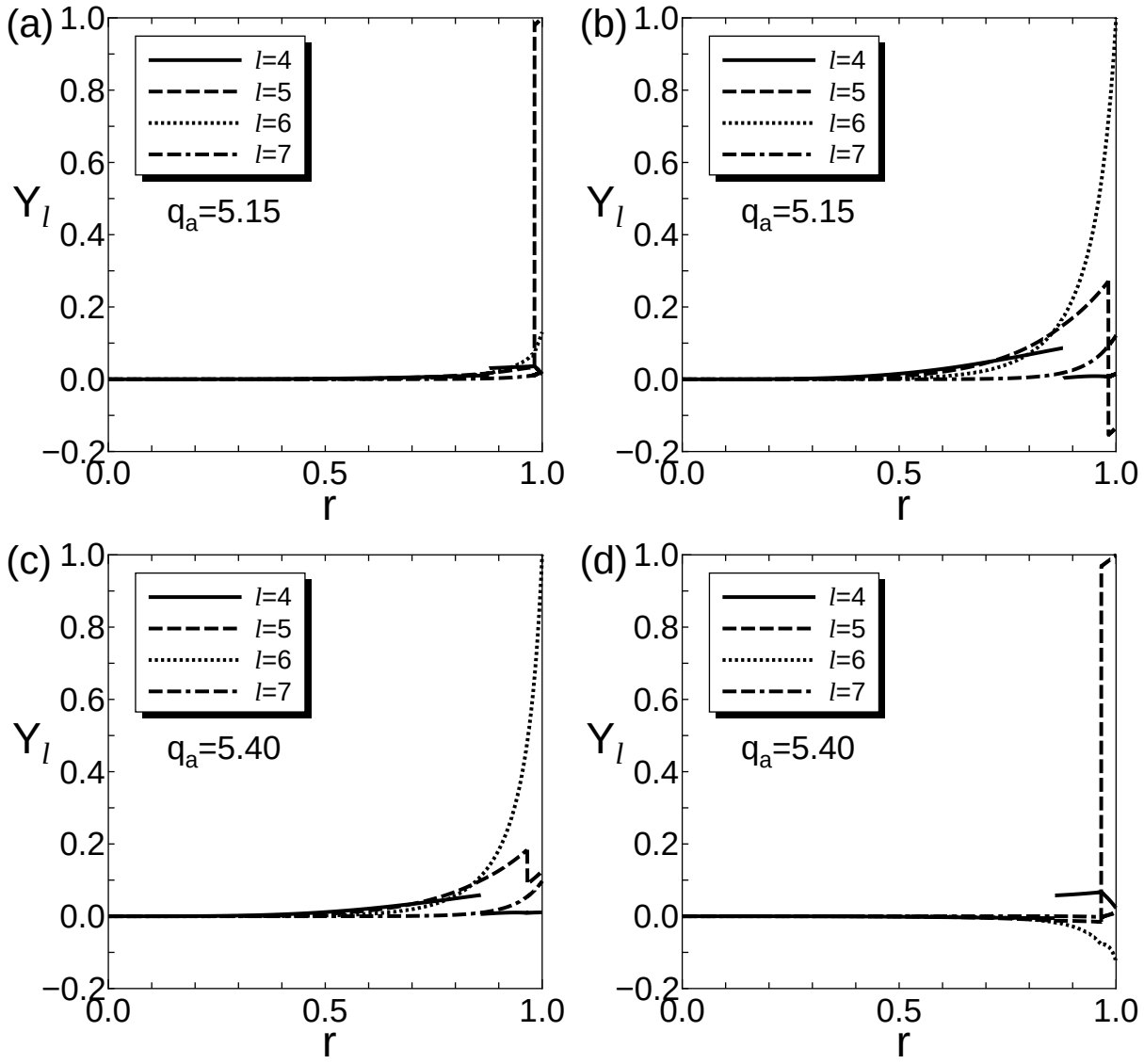

Figure 4.11: Poloidal Fourier harmonics of the eigenfunction when $A = 3.30$ and $\beta_p = 0.01$. (a) The eigenfunction belonging to the minimum eigenvalue and (b) that belonging to the second eigenvalue when $q_a = 5.15$. (c) The eigenfunction belonging to the minimum eigenvalue and (d) that belonging to the second eigenvalue when $q_a = 5.40$. The eigenfunction belonging to the minimum eigenvalue and that belonging to the second eigenvalue exchange for each other when q_a increases from 5.15 to 5.40. The dominant harmonics of these eigenfunctions accompany the neighbor harmonics; especially in the eigenfunction whose dominant harmonic is $l = 6$, shown in figures 4.11(b) and 4.11(c), the $l = 4$, 5, and 7 harmonics are excited.

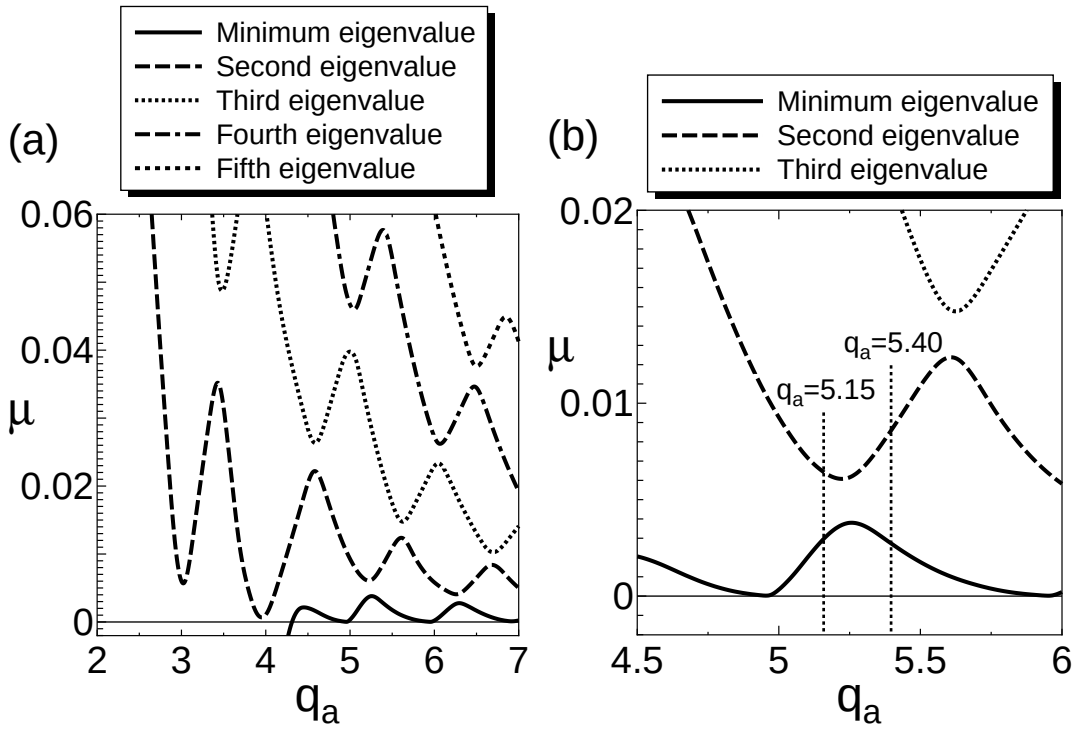

Figure 4.12: (a) Spectral structure of $n = 1$ external modes when $A = 3.30$ and $\beta_p = 0.80$. (b) Expansion of figure (a) in $4.50 \leq q_a \leq 6.00$. There are spectrum gaps and the widths of them are broader than those of the gaps when $A = 3.30$ and $\beta_p = 0.01$ in Fig. 4.10. The minimum eigenvalues become negative (unstable) in the region $q_a \leq 4.28$.

4.4 Coupling between ideal external modes and ideal internal modes

4.4.1 Coupling in high-β_p normal shear tokamaks

In this section, we verify the conjecture in the previous section; external modes couple with internal modes in the high-β_p case. We analyze the stability of internal modes by solving the associated eigenvalue problem Eq. (4.1) with the fixed boundary condition at the plasma surface (EV-fix), and compare the q_a dependence of λ_{0-int} with that of μ_0, where λ_{0-int} is the minimum eigenvalue obtained by EV-fix and μ_0 is that of the stability matrix (SM). The eigenvalues λ_{0-int} give us the spectral structure of internal modes even when these modes are stable [29]. Moreover, the SM method assumes that internal modes are stable, then the stability of external modes can be analyzed separately from that of internal modes. With these features, we can investigate the coupling between external modes and internal modes.

The equilibria used in this section are already shown in Fig. 4.4; whose cross sections are

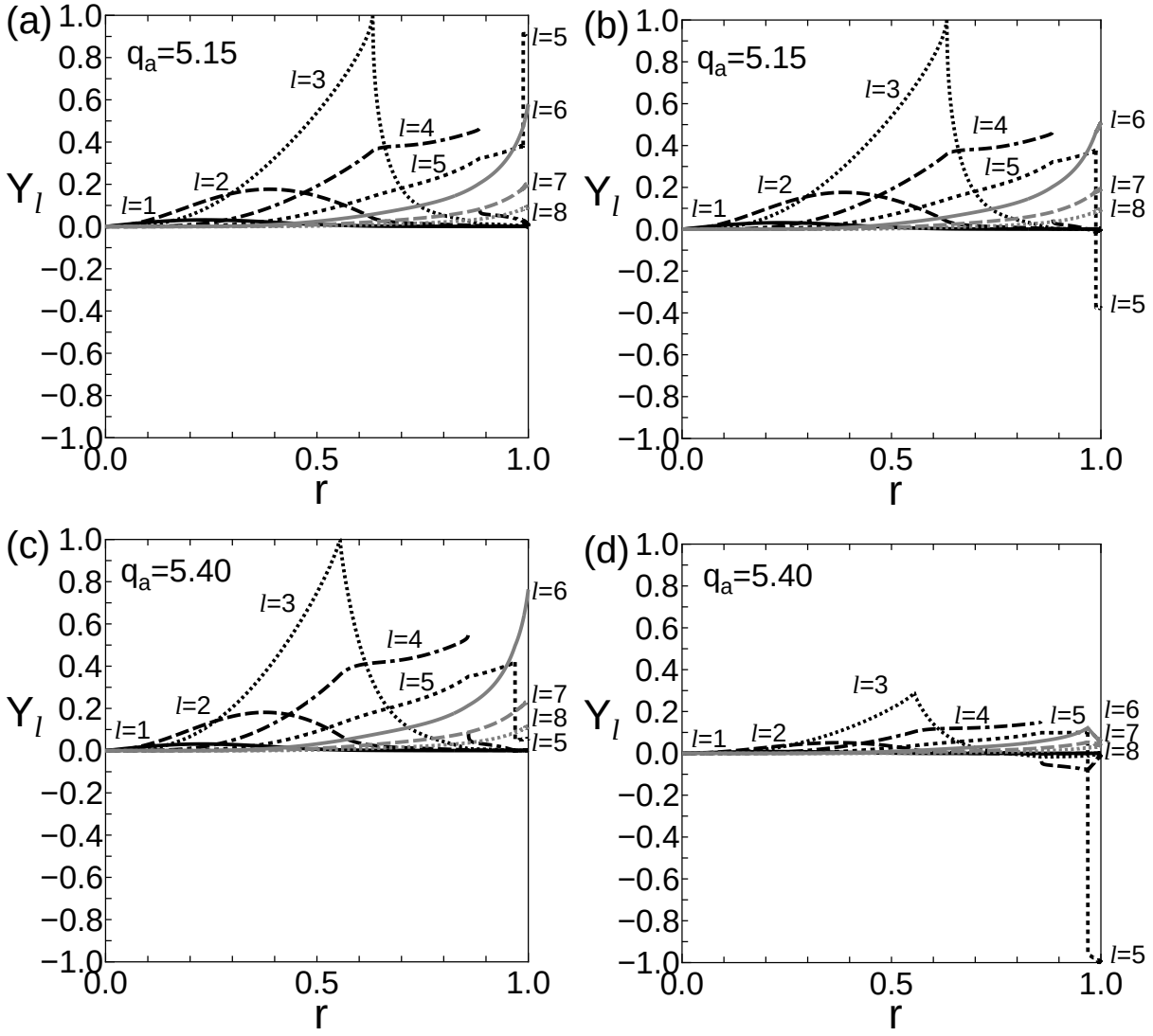

Figure 4.13: Poloidal Fourier harmonics of the eigenfunction when $A = 3.30$ and $\beta_p = 0.80$. (a) The eigenfunction belonging to the minimum eigenvalue and (b) that belonging to the second eigenvalue when $q_a = 5.15$. (c) The eigenfunction belonging to the minimum eigenvalue and (d) that belonging to the second eigenvalue when $q_a = 5.40$. The $l = 5$ and 6 harmonics of the eigenfunction belonging to the minimum eigenvalue and those of the eigenfunction belonging to the second eigenvalue exchange for each other when q_a increases from 5.15 to 5.40. However, unlike in the low-β_p toroidal case shown in Fig. 4.11, the $l = 3$ harmonic of these eigenfunctions is strongly excited.

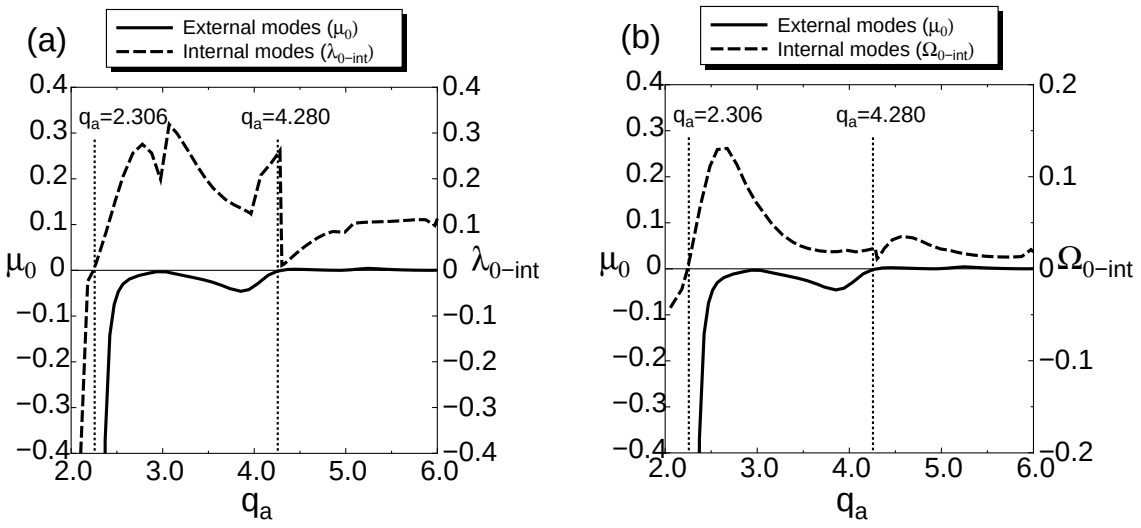

Figure 4.14: (a) Dependence of μ_0 on q_a and that of λ_{0-int} on q_a when $\beta_p = 0.80$. The label λ_{0-int} is the minimum eigenvalue obtained by solving Eq. (4.1) with the fixed boundary condition. The μ_0 value tends toward $-\infty$ as λ_{0-int} approaches to +0 near $q_a = 2.30$. Additionally, near $q_a = 4.00$, the q_a dependence of μ_0 and that of λ_{0-int} are convex downward. These results imply that the stability of internal modes affects that of external modes. (b) Dependence of μ_0 on q_a and that of Ω_{0-int} on q_a. This result also intimates that the stability of external modes is influenced by internal modes.

circular and $\beta_p = 0.80$. The vacuum contribution is calculated with the assumption of the no wall limit same as in the previous sections. The stability of internal modes is investigated in the (q_a, λ_{0-int}) plane, and a series of equilibria is obtained by the scaling as in Sections 4.2 and 4.3.

The eigenvalue λ_{0-int} expresses the potential energy integral $\delta W_p = 2\pi^2 \int_0^1 \langle \boldsymbol{Y}|\boldsymbol{\mathcal{N}}\boldsymbol{Y}\rangle\, dr$ normalized with the kinetic energy integral $\delta K = 2\pi^2 \int_0^1 \langle \boldsymbol{Y}|\mathrm{Diag}(\rho(r))|\boldsymbol{Y}\rangle\, dr$. However, the weight function $\rho(r)$ in δK varies as the safety factor profile changes. We introduce the normalized potential energy Ω_{0-int} defined as

$$\Omega_{0-int} = \delta \bar{W}_p = \int_0^1 \left\langle \bar{\boldsymbol{Y}}|\boldsymbol{\mathcal{N}}\bar{\boldsymbol{Y}}\right\rangle dr = \lambda_{0-int} \int_0^1 \left\langle \bar{\boldsymbol{Y}}|\mathrm{Diag}(\rho)|\bar{\boldsymbol{Y}}\right\rangle dr, \tag{4.6}$$

where

$$\left\langle \bar{\boldsymbol{Y}}|\bar{\boldsymbol{Y}}\right\rangle = 1, \tag{4.7}$$

and also investigate the stability of internal modes by comparing the values of Ω_{0-int}.

Figure 4.14(a) shows the q_a dependences of μ_0 and that of λ_{0-int}, and the q_a dependence of Ω_{0-int} is shown in Fig. 4.14(b). The solid line denotes μ_0 expressing the stability of external

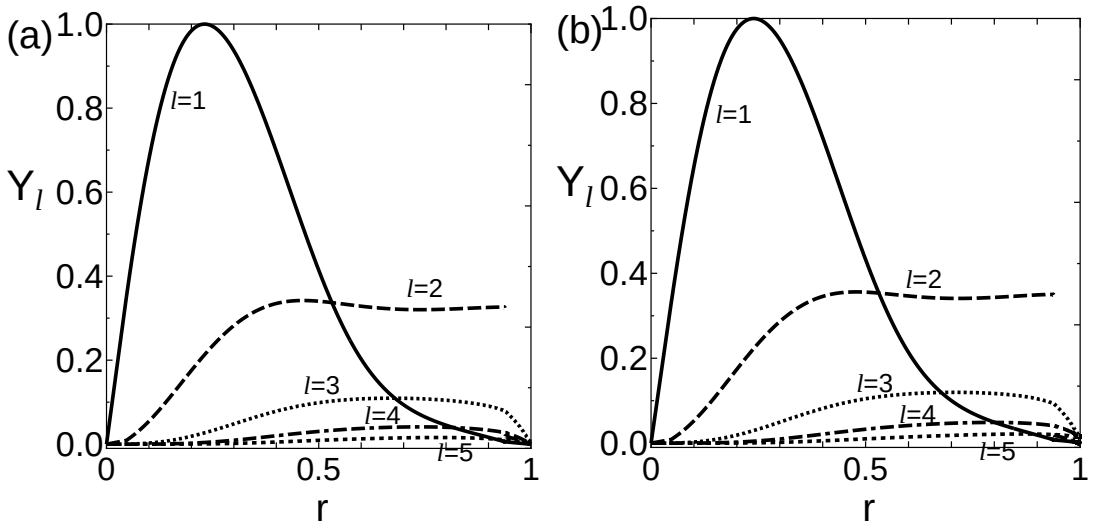

Figure 4.15: Poloidal Fourier harmonics of the eigenfunction belonging to the minimum eigenvalue when $q_a = 2.32$. (a) Eigenfunction obtained by solving Eq. (4.1) with the fixed boundary condition ($\lambda_{0-int} = 1.32 \times 10^{-3}$). (b) Eigenfunction obtained with the stability matrix ($\mu_0 = -27.5$). Since these are almost same as each other, the stability of internal modes affects that of external modes.

modes, already shown in Fig. 4.5, and the dashed line in Fig. 4.14(a) shows λ_{0-int} and that in Fig. 4.14(b) indicates Ω_{0-int} for the stability of internal modes. When $q_a < q_{a-mgl-int} = 2.306$ ($q_0 < 1.069$), internal modes whose dominant poloidal Fourier harmonic is $l = 1$ become unstable, and the analysis with SM is invalid.

When q_a is close to but larger than $q_{a-mgl-int}$, μ_0 tends toward $-\infty$ as λ_{0-int} approaches to +0, asymptotically. The poloidal Fourier harmonics of the eigenfunction belonging to λ_{0-int} and those of the eigenfunction belonging to μ_0 when $q_a = 2.32$ are shown in figures 4.15(a) ($\lambda_{0-int} = 1.32 \times 10^{-3}$) and 4.15(b) ($\mu_0 = -27.5$), respectively. Though the eigenfunction belonging to μ_0 expresses an external mode, both eigenfunctions are indistinguishable. These results show that internal modes strongly affect the stability of external modes when $q_a \simeq q_{a-mgl-int}$. The behavior of μ_0 near $q_a = q_{a-mgl-int}$ will be investigated analytically in the next subsection.

In the region $3.00 < q_a < 4.30$, the dependence of λ_{0-int} and that of Ω_{0-int} on q_a shown in Fig. 4.14, is convex downward. Moreover, the q_a dependence of μ_0 in Fig. 4.14 is also convex downward; $q_a = 3.97$ where μ_0 takes the minimum value is nearly equal to $q_a = 3.98$ where λ_{0-int} becomes minimum, and is also close to $q_a = 3.86$ where Ω_{0-int} is minimized.

Figure 4.16 shows the poloidal Fourier harmonics of the eigenfunction belonging to λ_{0-int} when $q_a = 4.27$; this q_a is same as that in Fig. 4.6. The $l \leq 3$ harmonics of this eigenfunction

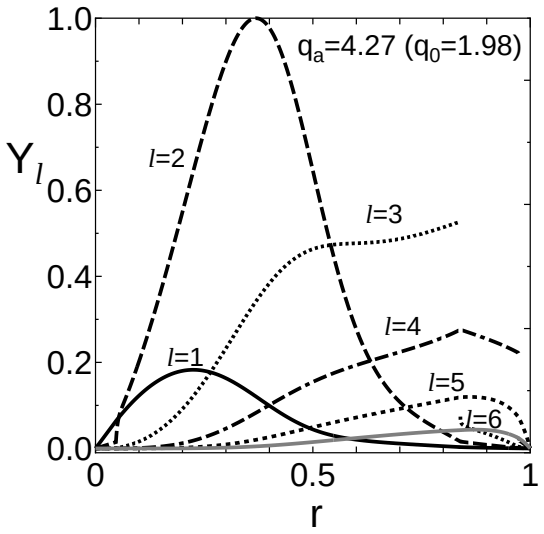

Figure 4.16: Poloidal Fourier harmonics of the eigenfunction belonging to the minimum eigenvalue obtained by solving Eq. (4.1) with the fixed boundary condition when $q_a = 4.27$. The $l \leq 3$ harmonics of this eigenfunction are similar to those of the eigenfunction belonging to μ_0 shown in Fig. 4.6(a).

are similar to those of the eigenfunction belonging to μ_0 shown in Fig. 4.6(a). We see that the stable internal mode is superimposed onto the surface mode with $l \geq 5$. These results also mean that external modes couple with internal modes.

The coupling between external modes and internal modes becomes weak as q_a increases so long as n is small. Figure 4.17 shows the poloidal Fourier harmonics of the eigenfunction belonging to λ_{0-int} and those of the eigenfunction belonging to μ_0 when $q_a = 4.90$. Unlike in figures 4.16 and 4.6(a), these eigenfunctions are quite different from each other, and we see that internal modes have little effect on the stability of external modes.

At $q_a \simeq 4.30$ ($q_0 \simeq 2.00$), the magnetic axis is also a rational surface, and it is impossible to calculate the eigenvalue λ_{0-int} correctly by the present formulation. Such a case is out of scope in this article.

4.4.2 Analysis near the marginal stability of ideal internal modes

In Subsection 4.4.1, we have shown that the minimum eigenvalue of the stability matrix μ_0 tends toward $-\infty$ as λ_{0-int} approaches to +0, where λ_{0-int} is the minimum eigenvalue obtained by solving the eigenvalue problem Eq. (4.1) with the fixed boundary condition. In this subsection, we investigate such behavior of μ_0 analytically.

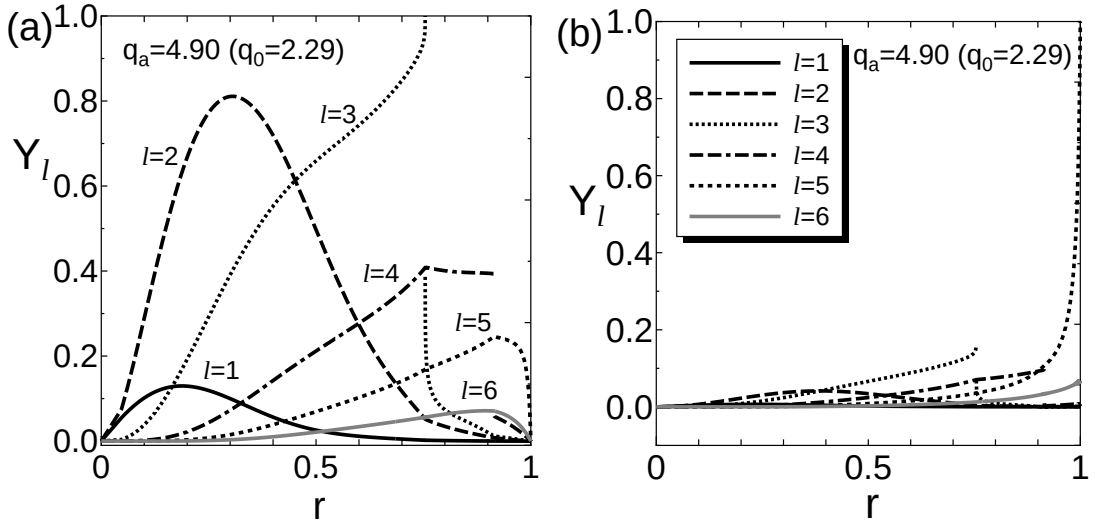

Figure 4.17: Poloidal Fourier harmonics of the eigenfunction belonging to the minimum eigenvalue when $q_a = 4.90$. (a) Eigenfunction obtained by solving Eq. (4.1) with the fixed boundary condition. (b) Eigenfunction obtained with the stability matrix. The mode structure of the internal mode, shown in Fig. 4.17(a), is quite different from that of the external mode in Fig. 4.17(b).

In general, the solution of the simultaneous equation

$$\mathbf{P}\boldsymbol{x} = \boldsymbol{y}, \tag{4.8}$$

can be written with the eigenfunctions $\boldsymbol{e}_n$ of the eigenvalue problem

$$\mathbf{P}\boldsymbol{e}_n = \Omega_n R\boldsymbol{e}_n, \tag{4.9}$$

as

$$\boldsymbol{x} = \sum_j x_j \boldsymbol{e}_j, \tag{4.10}$$

$$x_j = \frac{1}{\Omega_j}(\boldsymbol{e}_j \cdot \boldsymbol{y}), \tag{4.11}$$

where $\boldsymbol{e}_j$ is normalized as $(\boldsymbol{e}_j \cdot R\boldsymbol{e}_k) = \delta_{j,k}$ and R is the weight function. We apply this relation to Eq. (3.169) with the eigenfunction of Eq. (4.1) solved with the fixed boundary condition at the plasma surface. When $\lambda_{0-int} > 0$ be small, Eq. (3.169) for the basis functions can be approximately solved as

$$\boldsymbol{X}^m_{appx}(r) = -\frac{b^m_0}{\lambda_{0-int}}\boldsymbol{\xi}_{0-int}(r), \tag{4.12}$$

where $\boldsymbol{\xi}_{0-int}$ is the eigenfunction belonging to λ_{0-int} and satisfies the boundary condition $\boldsymbol{\xi}_{0-int}(a) = 0$; the coefficient b_0^m is given by

$$b_0^m = (\boldsymbol{\xi}_{0-int}(r), -\mathcal{N}\boldsymbol{Z}^m(r)) = \int_0^a \boldsymbol{\xi}_{0-int}(r) \cdot (-\mathcal{N}\boldsymbol{Z}^m(r))dr. \tag{4.13}$$

By using Eq. (4.12) in Eq. (3.166), we have

$$\begin{aligned} W_p[\boldsymbol{Y}^l, \boldsymbol{Y}^m]_{appx} = &\frac{b_0^l}{\lambda_{0-int}} \cdot \frac{b_0^m}{\lambda_{0-int}} W_p[\boldsymbol{\xi}_{0-int}, \boldsymbol{\xi}_{0-int}] - \frac{b_0^l}{\lambda_{0-int}} W_p[\boldsymbol{\xi}_{0-int}, \boldsymbol{Z}^m] \\ &- \frac{b_0^m}{\lambda_{0-int}} W_p[\boldsymbol{Z}^l, \boldsymbol{\xi}_{0-int}] + W_p[\boldsymbol{Z}^l, \boldsymbol{Z}^m]. \end{aligned} \tag{4.14}$$

Here, let us remember that $W_p[\boldsymbol{\xi}_{0-int}, \boldsymbol{\xi}_{0-int}] = \lambda_{0-int}$ and

$$\begin{aligned} W_p[\boldsymbol{\xi}_{0-int}, \boldsymbol{Z}^m] &= \int_0^a \boldsymbol{\xi}_{0-int}(r) \cdot (-\mathcal{N}\boldsymbol{Z}^m(r))dr = b_0^m, \\ W_p[\boldsymbol{Z}^l, \boldsymbol{\xi}_{0-int}] &= \int_0^a \boldsymbol{\xi}_{0-int}(r) \cdot (-\mathcal{N}\boldsymbol{Z}^l(r))dr = b_0^l. \end{aligned} \tag{4.15}$$

Consequently, Eq. (4.14) reads

$$W_p[\boldsymbol{Y}^l, \boldsymbol{Y}^m]_{appx} = -\frac{1}{\lambda_{0-int}} \boldsymbol{b} \otimes \boldsymbol{b} + W_p[\boldsymbol{Z}^l, \boldsymbol{Z}^m], \tag{4.16}$$

and the stability matrix $\mathbf{A}_{appx}$ is given by

$$\mathbf{A}_{appx} = -\frac{1}{\lambda_{0-int}} \boldsymbol{b} \otimes \boldsymbol{b} + W_p[\boldsymbol{Z}^l, \boldsymbol{Z}^m] + \boldsymbol{M}_V. \tag{4.17}$$

Here

$$\boldsymbol{b} := \{b_0^{-L_f}, \cdots, b_0^{L_f}\}, \tag{4.18}$$

and

$$\boldsymbol{b} \otimes \boldsymbol{b} = (b_0^l b_0^m). \tag{4.19}$$

Let us notice that the matrix $\boldsymbol{b} \otimes \boldsymbol{b}$ is a symmetric semi-positive matrix and all eigenvalues of $\boldsymbol{b} \otimes \boldsymbol{b}$ are non-negative. Let α_{-1} be the maximum eigenvalue of $\boldsymbol{b} \otimes \boldsymbol{b}$ and $\boldsymbol{y}_0$ is the eigenvector belonging to α_{-1}, then the minimum eigenvalue of $\mathbf{A}_{appx}$ is approximately given by

$$\mu_{0-appx} = -\frac{\alpha_{-1}}{\lambda_{0-int}} + \left\langle \boldsymbol{y}_0 | W_p[\boldsymbol{Z}^l, \boldsymbol{Z}^m] + \mathbf{M}_V | \boldsymbol{y}_0 \right\rangle. \tag{4.20}$$

Therefore, μ_{0-appx} tends toward $-\infty$ when λ_{0-int} approaches to $+0$; $n = 1$ ideal external modes are always unstable when $n = 1$ ideal internal modes are marginally stable.

Figure 4.18 shows the dependence of μ_0 on q_0 and that on q_a. The λ_{0-int} value becomes to be zero at $q_{0-int} = 1.0694$, and $1/\mu_0$ also becomes to be zero at q_{0-int}. The solid line denotes the minimum eigenvalue μ_0 obtained with the original stability matrix Eq. (3.166) (Original), the dashed line shows that obtained with the approximated stability matrix Eq. (4.17) (Approximation 1), and the dotted line is for the approximated eigenvalue μ_{0-appx} given by Eq.

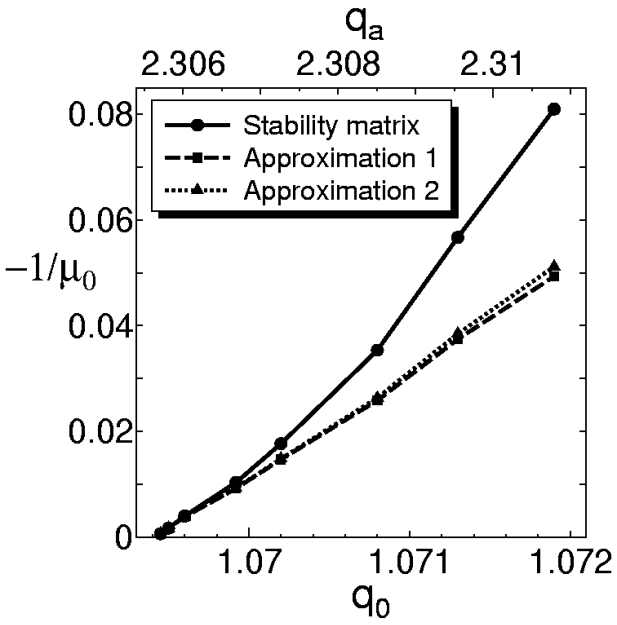

Figure 4.18: Dependence of $-1/\mu_0$ on q_0 and that on q_a. The solid line denotes the result obtained with the original stability matrix Eq. (3.166), the dashed line shows the result obtained with the approximated stability matrix Eq. (4.17), and the dotted line is for the result given by Eq. (4.20). Each line tends toward+0 as q_0 decreases to $q_{0-int} = 1.0694$.

(4.20) (Approximation 2), respectively. We observe that Eqs. (4.17) and (4.20) well describe the behavior of μ_0 near the marginal stability of internal modes. The q_a dependence of μ_0 analyzed by Approximation 1 and 2 are almost same each other, and tend toward the Original μ_0 as λ_{0-int} approaches to +0 asymptotically.

Equation (4.12) reveals the meaning of *coupling* between an external mode and an internal mode. When λ_{0-int} is small, the basis function $\boldsymbol{Y}^m$ defined by Eq. (3.163) is approximately given by

$$\boldsymbol{Y}^m(r) = -\frac{b_0^m}{\lambda_{0-int}}\boldsymbol{\xi}_{0-int}(r) + \boldsymbol{Z}^m(r). \tag{4.21}$$

Consequently, any external modes expressed by Eq. (3.168) include $\boldsymbol{\xi}_{0-int}(r)$ as the dominant component, which explains Figs. 4.13 and 4.15.

4.4.3 Coupling in reversed shear tokamaks

We have confirmed that internal modes can be coupled with external modes and can destabilize them in high-β_p tokamaks. Therefore, it will be interesting and important to investigate from this viewpoint the stability of external modes in reversed shear tokamaks (RS).

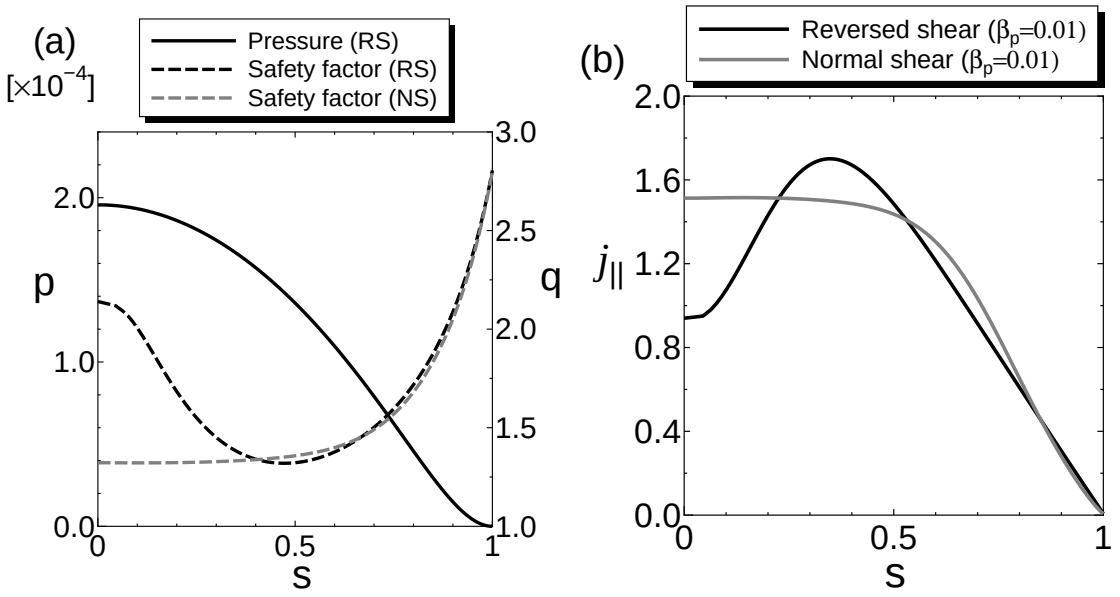

Figure 4.19: (a) Profiles of the pressure p and the safety factor q of the reversed shear equilibrium (RS) and the q profile of the normal shear one (NS). The β_p of these equilibria are 0.01. The minimum safety factor q_{min} in RS is 1.32 that equals to q_0 in NS, and the q_a values in both equilibria are 2.80. (b) Profile of the parallel current density $j_\parallel$ of RS and that of NS. These profiles near the plasma surface are similar to each other.

We first analyze the stability of external modes in the low $\beta_p (= 0.01)$ RS whose aspect ratio is $A = 3.30$ and the cross sections are circular. Since, in low β_p tokamaks, the stability of external modes mostly depends on the q profile and the average parallel current density $j_\parallel$ profile near the plasma surface, we make RS equilibria so that these profiles near the plasma surface are almost same as those of normal shear tokamaks (NS), where $j_\parallel$ is defined as

$$j_\parallel \equiv \frac{\langle \boldsymbol{J} \cdot \boldsymbol{B} \rangle_f}{\langle B^2 \rangle_f} = -\frac{F}{\langle B^2 \rangle_f} \frac{dp}{d\psi} - \frac{1}{\mu_0} \frac{dF}{d\psi}, \tag{4.22}$$

and $\langle C \rangle_f$ is the flux average value of a variable C defined in Eq. (2.18). Figure 4.19(a) shows the p and q profiles of the RS and the q profile of the $A = 3.30$ and $\beta_p = 0.01$ NS, already shown in Fig. 4.7, and the $j_\parallel$ profiles are shown in Fig. 4.19(b). The minimum q value of RS, q_{min}, is set to $q_0 = 1.32$ of NS when q_a of RS is equal to that of NS ($q_a = 2.80$) because the rational surfaces in the plasma are important for the stability of internal modes.

The spectral structure of external kink modes in the $\beta_p = 0.01$ RS is shown in Fig. 4.20, and is almost same as that in the $\beta_p = 0.01$ NS shown in Fig. 4.10. This is because the q and $j_\parallel$ profiles of NS and those of RS are almost same as each other near the plasma surface. This result means that the difference between the q profile of RS and that of NS in the plasma core scarcely affects the stability of external modes as expected; internal modes and external

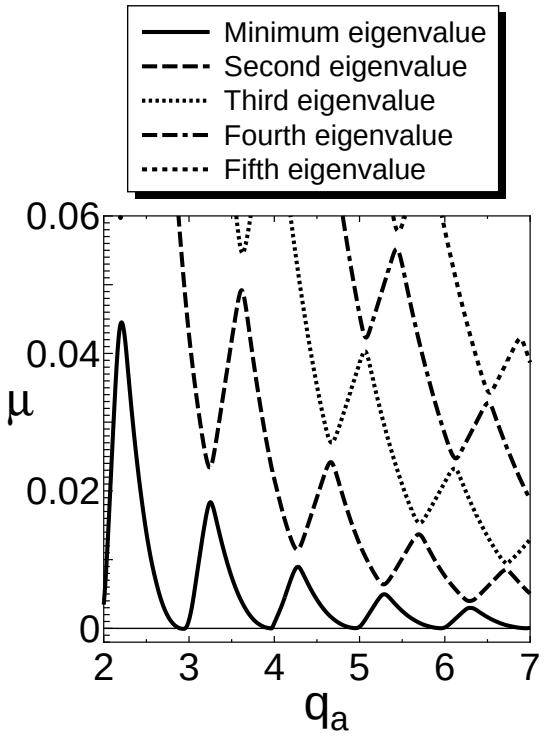

Figure 4.20: Spectral structure of $n = 1$ ideal external kink modes in the $A = 3.30$ and $\beta_p = 0.01$ RS. This structure is almost same as that in the $A = 3.30$ and $\beta_p = 0.01$ NS in Fig. 4.10.

modes are almost independent from each other. Next, we investigate the stability of external modes in the high-β_p ($= 0.80$) RS. The p and q profiles are shown in Fig. 4.21(a), and the $j_{\parallel}$ profiles are shown in Fig. 4.21(b); q_{min} of this RS is also set to $q_0 = 1.30$ of NS when q_a of RS is equal to that of NS ($q_a = 2.80$). Near the plasma surface, the q and $j_{\parallel}$ profiles of RS are almost same as those of NS and those of the low-β_p equilibria in Fig. 4.19.

Figure 4.22 shows the q_a dependence of μ_0, that of λ_{0-int} and that of Ω_{0-int}. In Fig. 4.22(a), the black solid line and the black dashed line show μ_0 and λ_{0-int} in NS, and the gray solid line and the gray dashed line are for μ_0 and λ_{0-int} in RS, already shown in Fig. 4.14, respectively. The black and gray dashed lines in Fig. 4.22(b) express Ω_{0-int} in NS and that in RS. When q_a is close to but larger than 2.32, μ_0 in RS tends toward $-\infty$ as λ_{0-int} approaches to $+0$. This agrees with the result in Subsection 4.4.2.

We first pay attention to the solid lines in the region $4.50 < q_a$; these are nearly identical to each other. Figure 4.23 shows the poloidal Fourier harmonics of the eigenfunction belonging to μ_0 in RS when $q_a = 4.90$. This eigenfunction is a surface mode whose dominant harmonic is $l = 5$, and is similar to the eigenfunction in high-β_p NS when $q_a = 4.90$ in Fig. 4.17. When q_a increases, low-n external modes become surface modes, and the stability is

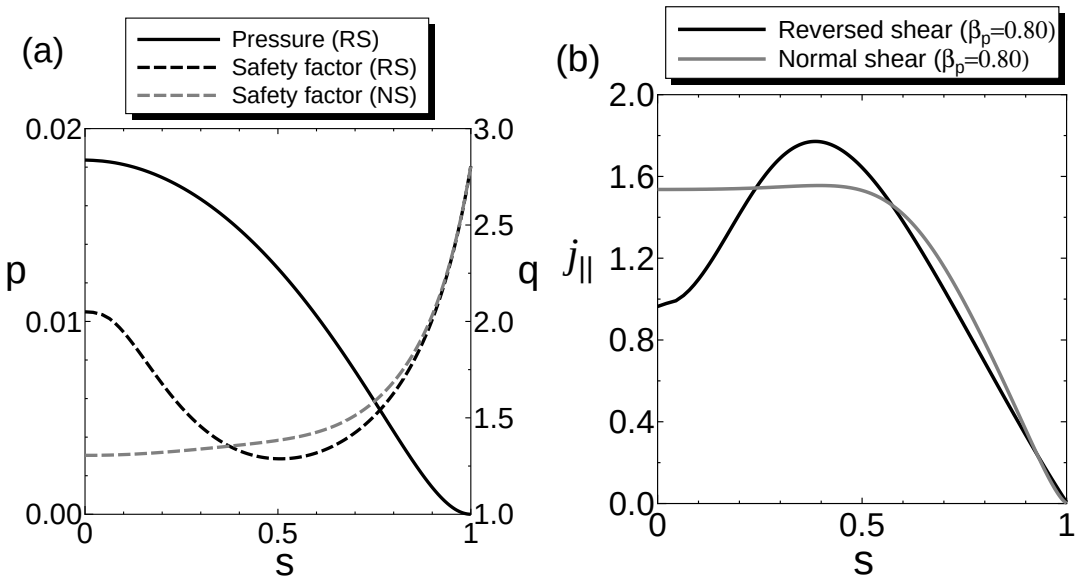

Figure 4.21: (a) Profiles of the pressure p and the safety factor q of RS and the q profile of NS. The β_p of these equilibria are 0.80. The values of q_{min} and q_a in RS are same as those in NS ($q_{min} = 1.30$, $q_a = 2.80$). (b) Profile of the parallel current density $j_{\|}$ of RS and that of NS. These profile near the plasma surface are similar to each other.

mostly determined by the magnetic shear and $j_{\|}$ profiles near the plasma surface, and internal modes have little effects on the stability of external modes. Figure 4.23 and the spectral structure for $q_a > 4.50$ in Fig. 4.22 confirm this conjecture.

We next find the high-β_p RS equilibria still have a stable window against external modes, $3.00 < q_a < 3.52$, although the high-β_p NS equilibria are unstable when $q_a < 4.28$. Since the destabilizing effects of the current density near the plasma surface in both equilibria are considered as almost same and the Ω_{0-int} values in RS are larger than those in NS as shown in Fig. 4.22(b), we guess that such stabilization of external modes reflects the difference of the stability of internal modes, which is caused by the different q profiles.

This conjecture is confirmed as follows. Figure 4.24 shows the poloidal Fourier harmonics of the eigenfunction belonging to μ_0 (Fig. 4.24(a)) and those of the eigenfunction belonging to λ_{0-int} (Fig. 4.24(b)) when $q_a = 3.53$ in RS; this q_a is close to $q_{a-mgl} = 3.52$ that is the marginally stable q_a for external modes in RS. These figures imply that the internal mode whose harmonics are $l \leq 3$ destabilize the external mode with the $l \geq 4$ harmonics peaking at the plasma surface, as in the high-β_p NS case shown in Fig. 4.6. However, Fig. 4.22 tells us that internal modes in RS are more stable than those in NS when $3.00 < q_a < 4.50$, and as the result, the effect of internal modes on the stability of external modes in RS is weaker than that in NS.

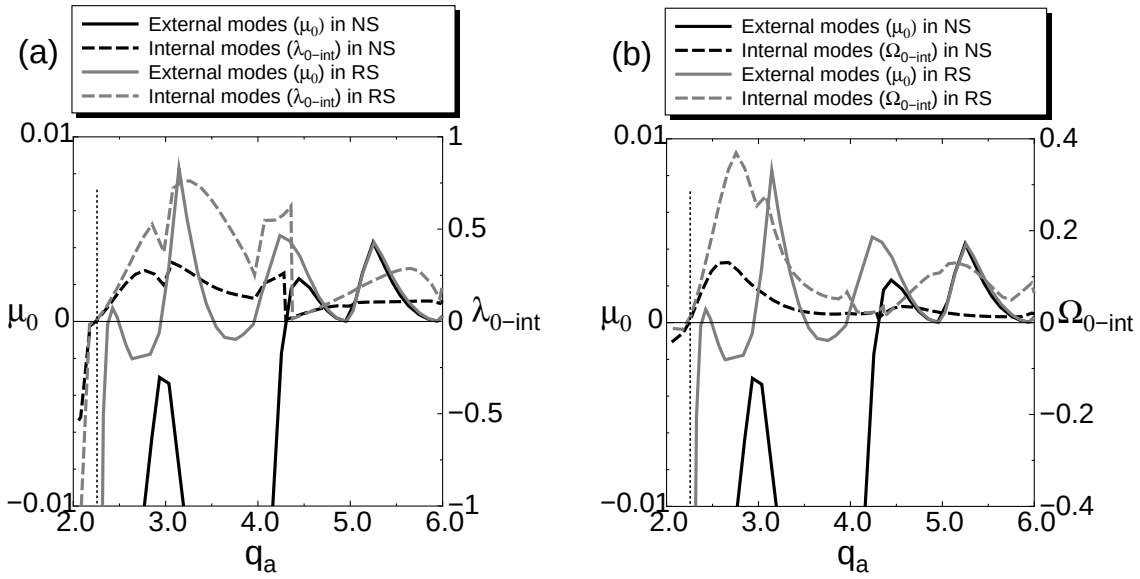

Figure 4.22: (a) Dependence of μ_0 on q_a and that of λ_{0-int} on q_a in RS, and those in NS, already shown in Fig. 4.14(a). The β_p of these RS and NS are same as 0.80. In both equilibria, μ_0 tends toward $-\infty$ as λ_{0-int} approach to +0 near the marginally stable q_a for internal modes. The spectral structure for external modes in RS when $q_a \geq 4.50$ is almost indistinguishable with that in NS. It is because the destabilizing effects for $q_a \geq 4.50$ are almost same as each other. In RS, a stable window against external modes exists in lower q_a, $3.00 \leq q_a \leq 3.53$. (a) Dependence of μ_0 on q_a and that of Ω_{0-int} on q_a in RS, and those in NS. The Ω_{0-int} values in RS are larger than Ω_{0-int} values in NS; this implies that internal modes in RS is more stable than those in NS.

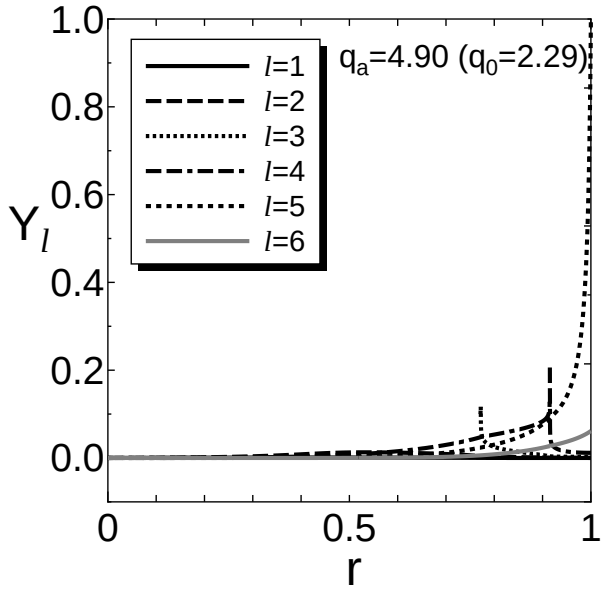

Figure 4.23: Poloidal Fourier harmonics of the eigenfunction belonging to the minimum eigenvalue of the stability matrix when $q_a = 4.90$ in RS. The eigenfunction shows a surface mode structure and is similar to the eigenfunction in NS (Fig. 4.17(b)). This result implies that the β_p effect on the stability of external modes becomes weak as q_a increases.

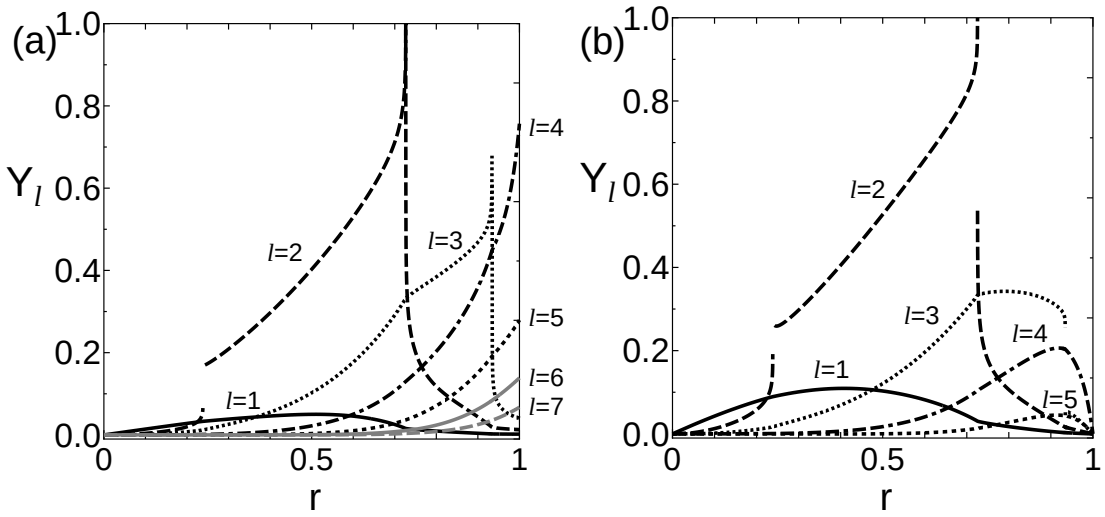

Figure 4.24: (a) Poloidal Fourier harmonics of the eigenfunction belonging to the minimum eigenvalue of the stability matrix (external modes), and (b) those of the eigenfunction belonging to the minimum eigenvalue obtained by solving Eq. (4.1) with the fixed boundary condition (internal modes), in the $\beta_p = 0.80$ and $q_a = 3.53$ RS. The profile of $l \leq 3$ harmonics in figure (a) are similar to that in figure (b), and these harmonics destabilize external modes.

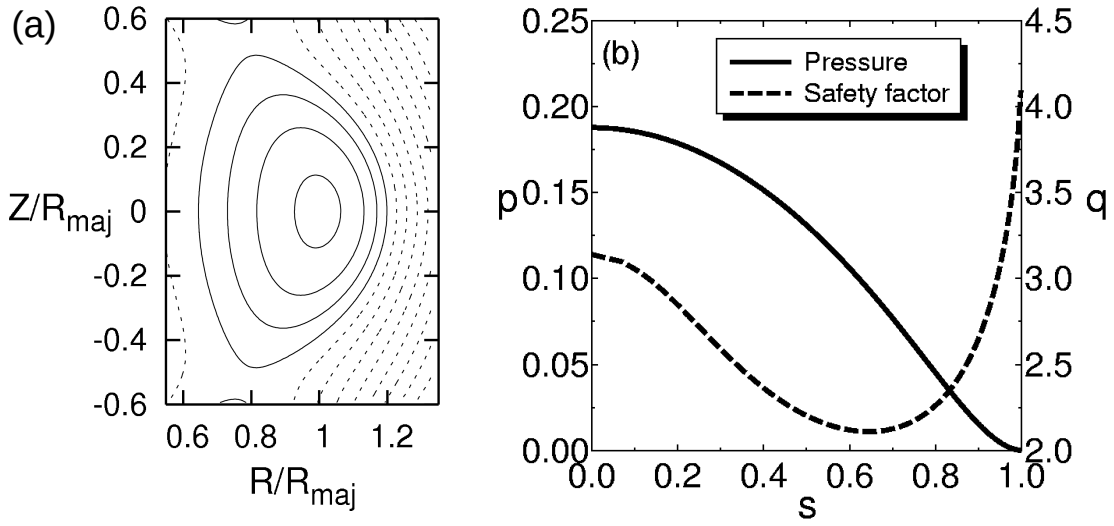

Figure 4.25: Equilibrium for analyzing the effect of aspect ratio. Parameters are $A = 3.26$ and $\beta_N = 6.0$. (a) Contours of ψ. The outermost solid line shows the plasma surface. (b) Profiles of the pressure p and the safety factor q. The q_0 and q_a values are 3.05 and 4.1, respectively.

4.5 Effect of the aspect ratio on the stability of external modes

As an application of the analysis with the stability matrix, we analyze the effect of the aspect ratio on the stability of $n = 1$ external modes. The shape parameters of equilibria are fixed as $\kappa = 1.8, \delta = 0.45$. The profiles of $dp/d\psi$ are also fixed. The toroidal magnetic field at the magnetic axis, B_{t0}, and the poloidal field current, I_p, depend on the aspect ratio A as

$$B_{t0}(A) = B_{t0}(A = 3.26) \times \frac{R_{maj}}{R_{maj}(A = 3.26)}, \tag{4.23}$$

$$I_p(A) \simeq I_p(A = 3.26) \times \frac{R_{maj}(A = 3.26)}{R_{maj}}, \tag{4.24}$$

where $B_{t0}(A = 3.26) = 3.36$, $R_{maj}(A = 3.26) = 2.93$, and $I_p(A = 3.26)$ of the normalized beta $\beta_N = 5.0$ equilibrium is set to 4.0, respectively. Though the q profile varies as A and β_N change, q value at $s = 0.95$ is fixed as $q_{95} = 3.5$ by adjusting the I_p value. The profiles of the $A = 3.26$ equilibrium are shown in Fig. 4.25.

We first investigate the dependence of the β_N limit on the aspect ratio against $n = 1$ ideal external modes with no wall limit assumption. As shown in Fig. 4.26, a low aspect ratio equilibrium is more stable against $n = 1$ external modes. In particular, when $A \leq 4$, the dependence of the external mode stability on the A value is stronger than that when $A > 4$; the β_N limit increases from 2.4 to 3.5 as A decreases from 4.0 to 2.24.

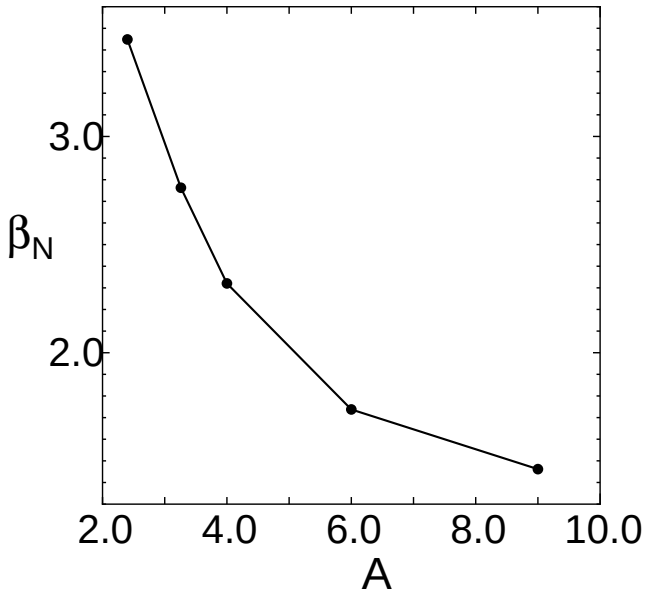

Figure 4.26: Dependence of the β_N limit against $n = 1$ ideal external kink modes on the aspect ratio A, where no perfect conducting wall limit is assumed. The β_N limit increases as A decreases.

Figure 4.27 shows the dependence of the β_N limit against $n = 1$ ideal external modes on the position of a perfect conducting wall. The position of a conducting wall b is defined as

$$b \equiv \frac{1}{2}\Big((R_{+wall}(\phi = 0, Z = 0) - R_{+plasma}(\phi = 0, Z = 0) + (R_{-wall}(\phi = 0, Z = 0) - R_{-plasma}(\phi = 0, Z = 0))\Big), \tag{4.25}$$

where R_{wall} is the R coordinate of the wall, R_{plasma} is that of the plasma surface, and subscripts + and − indicate $R_+ > R_-$. When $\beta_N < 7.5$, a small aspect ratio equilibrium is more stable than a large aspect ratio one. Especially, in these calculations, $b/a = 1.4$ is enough to achieve a high performance ($\beta_N > 5.0$) operation in each A case.

The eigenfunctions, when $\beta_N = 6.0$ and the wall position is slightly more far from a plasma surface than the marginally stable position, are shown in Fig. 4.28. In $A = 3.26$ case, the growth rate calculated with ERATOJ is $\gamma^2 = 1.6 \times 10^{-5}$; that is normalized with the toroidal Alfvén transit time at the magnetic axis. These eigenfunctions have a global mode structure unlike in a low β case shown in Section 4.2 [31]. From these results and those obtained in Section 4.4, the stability of ideal internal modes has an effect on the stability of ideal external modes.

The $m = 3$ Fourier components obtained with MARG2D-SM in each aspect ratio cases are pointed near the outer $q = 3.0$ rational surface. However, since the widths of these points

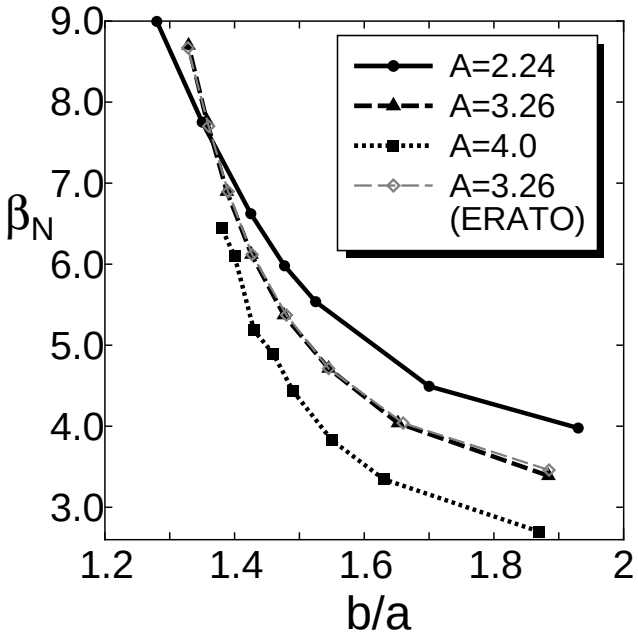

Figure 4.27: Dependence of the β_N limit against $n = 1$ ideal external kink modes on the position of a perfect conducting wall b. $b/a = 1.4$ is enough to achieve that the β_N limit is larger than 5.0 in each A case.

are nearly 0.001 measured in s, a general structure of the eigenfunction is almost the same as that obtained with ERATOJ.

4.6 Summary

I have developed the MARG2D-SM code to realizes the stability analysis of external modes with the stability matrix method, which is introduced in Section 3.7. By the benchmark tests of this code with MARG2D and ERATOJ, I confirmed the validity of this method. By using the stability matrix, we have comprehensively studied the spectral structure of the $n = 1$ ideal external kink modes, stable or unstable. Especially, I clarified numerically the spectral gaps induced by the poloidal coupling originated from the finite aspect ratio effect. It has been also shown that the finite poloidal beta (β_p) effect makes these gaps broaden. Such toroidal effects of the low-n external modes were previously predicted, and the present calculations confirmed clearly these predictions.

The stability matrix method enables us to perform deeper analysis of the external modes when it is combined with the eigenvalue problem associated with the original Newcomb equation. They elucidate numerically and analytically the effects of internal modes on the

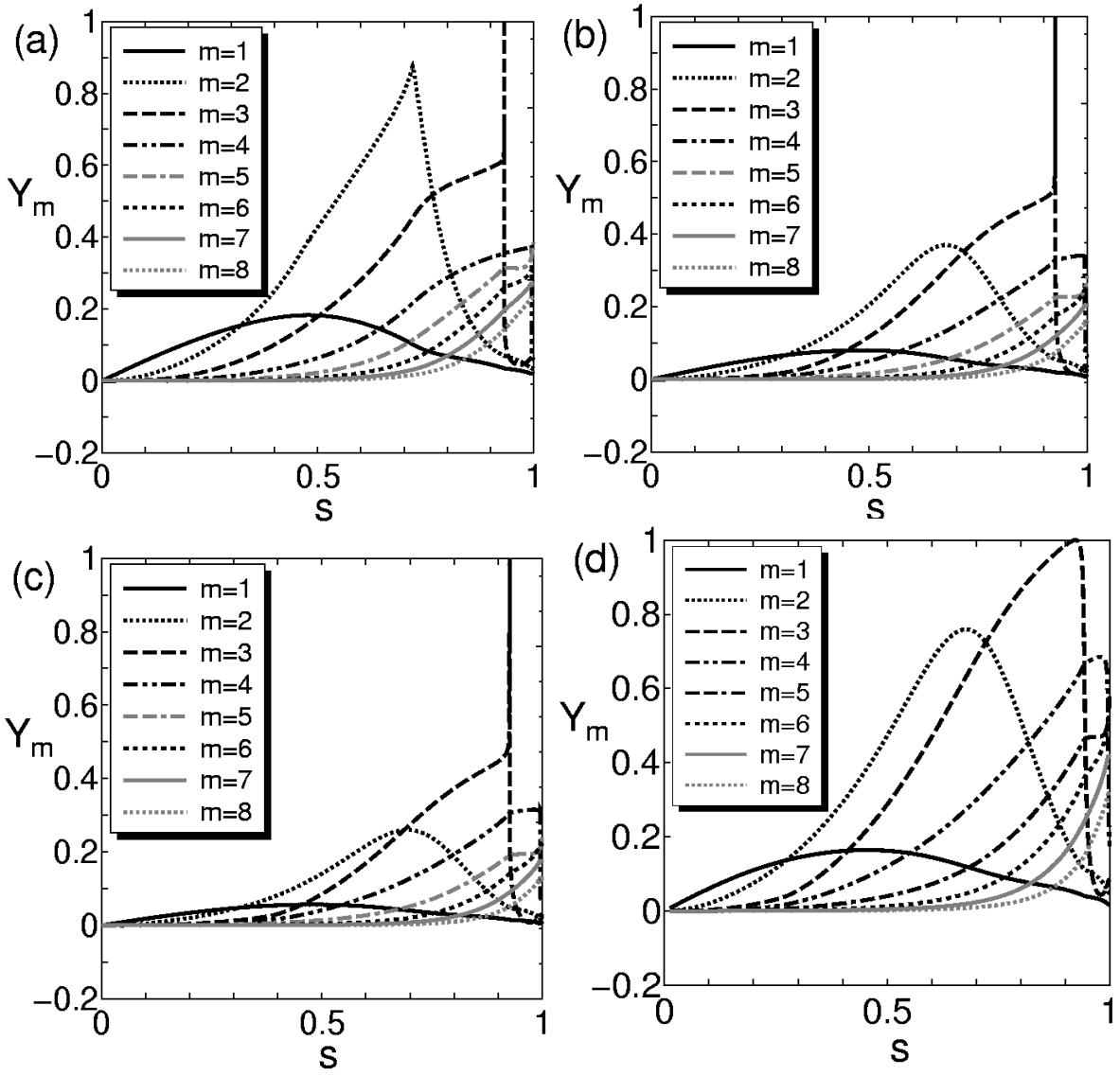

Figure 4.28: Eigenfunctions when $\beta_N = 6.0$. (a) $A = 2.44$ obtained with MARG2D-SM code. (b) $A = 3.26$ with MARG2D-SM. (c) $A = 4.0$ with MARG2D-SM. (d) $A = 3.26$ obtained with ERATOJ code.

stability of external modes when the internal modes approach to their marginal stability (the β limit, for example). The coupling with the internal modes changes the surface mode structure of the external modes into the global mode structure. It also explains the difference of stability against external modes between a normal shear tokamak and a reversed shear tokamak. Such effects may be also important for the stability of the resistive wall modes (RWMs) since we are interested in the stability of it for highβ plasma where the internal modes can be close to their marginal stability.

As an application of MARG2D-SM, I analyzed an effect of the aspect ratio on the stability of external modes in highβ tokamaks. From this result, I confirmed that external modes are stabilized as the aspect ratio decreases. Since the eigenfunction belonging to the minimum eigenvalue in highβ tokamaks has a global mode structure, low$n$ ideal external modes are dangerous for operations, and the aspect ratio is supposed to be optimized for stabilizing such MHD modes.

An application to the RWMs such as construction of an eigenvalue problem was out of scope in the present work. For example, M. Chu*et al.* showed in Ref. [13] that an eigenvalue problem for the RWMs with the Hermitian property can be constructed when the plasma inertia is neglected. The application of the present formulation to the RWMs will be reported near future.

Chapter 5

Extension of the analytical model for high-n external mode analysis in tokamak edge plasma

5.1 Introduction

In this chapter, we focus on a high-n external MHD mode analysis in tokamak edge plasma. As already mentioned in Chapter 1, since high-n external modes (a peeling mode [18], an edge-ballooning mode [19], and a couple of them called a peeling-ballooning mode) are related to edge localized modes (ELMs) that constrain the maximum achievable gradients in the pedestal at tokamak edge region [19, 26], these modes are one of key components for fusion research.

In Chapter 3 and Ref. [29], a new eigenvalue problem associated with the two-dimensional Newcomb equation has been posed by formulating such that the spectra of the eigenvalue problem are comprised of only real and denumerable eigenvalues without continuous spectra, and the MARG2D code [29] has been developed to solve this eigenvalue problem on the basis of this formulation. Though the eigenvalues obtained by the MARG2D code do not correspond to growth rates or frequencies of MHD modes, the sign of them can identify the stability against ideal MHD motions. By way of compensation, this code can realize a fast stability analysis in comparison with stability codes ERATO [32] and MISHKA [24], which are developed based on a full MHD model. From a pragmatic viewpoint about a linear ideal stability analysis, we often do not pay attention to growth rates of unstable MHD modes, but whether MHD modes are stable or unstable. Moreover, since continuous spectra exist in the stable region, a linear ideal MHD stability analysis based on a full MHD model can not identify the stable condition numerically. On the contrary, MARG2D always can determine whether MHD modes are stable or unstable. These benefits of the MARG2D code, in fact a

short computation time and a facility to identify marginal stability, are effective to analyze middle-n and high-n modes stabilities.

For an external MHD mode analysis, the vacuum energy contribution must be calculated correctly. However, a Green's function technique, introduced in Appendix C and applied in the previous chapters, is not suited to calculate the vacuum energy contribution in high-n case, because the numerical precision loses as n increases. To avoid such a problem, I apply the approach that the vacuum contribution is represented in the same form as the plasma contribution by introducing a solenoidal vector field, called the vector potential method [35], and extend the MARG2D formulation, introduced in Chapter 3, to the vacuum region. This extension realizes a broad n range of external mode analyses on the basis of the single physical model, unlike in the ELITE code [21,22] whose formulation uses the large-n ordering [19]. This benefit will be effective in future for analyzing edge phenomena by the integrated simulation between the MHD stability code and the transport code. To archive this simulation, I develop the MARG2D code as a parallel computing code with the message passing interface (MPI) [36] and the ScaLAPACK library [37], and shorten the computation time for the stability analysis.

This chapter is set out as follows. In the next section, I describe the coordinate system and a solenoidal vector field for the vacuum region. After introducing the boundary condition at the plasma-vacuum interface and that on the wall in Section 5.3, I extend the MARG2D formulation to the vacuum region in Section 5.4. Then, in Section 5.5, I describe benchmark tests of the extended MARG2D code implemented the present formulation with the ERATOJ code (the JAERI version of the ERATO code), and confirm the validity of high-n mode analysis with the extended MARG2D code in Section 5.6. In Section 5.7, performance results of parallel computing with the Scalapack library are shown. I summarize the present work in Section 5.8.

5.2 Construction of coordinates in the vacuum

5.2.1 Auxiliary coordinate system (ρ, ζ, ϕ)

We introduce an auxiliary coordinate system (ρ, ζ, ϕ) by

$$R = R_{maj} + \rho\cos\zeta, \quad Z = \rho\sin\zeta. \tag{5.1}$$

We assume that the shapes of the plasma edge (the plasma surface) and an ideal conducting wall are expressed as functions of ζ;

$$\rho = \rho_p(\zeta), \tag{5.2}$$

for the plasma edge, and

$$\rho = \rho_w(\zeta), \tag{5.3}$$

for the conducting wall. A function (quasi magnetic surface) ψ_V is defined by

$$\psi_V = \psi_p s^2, \quad 1 \le s \le s_{max}, \tag{5.4}$$

where s_{max} is a given number, for example $s_{max} = 2$. Each contour of $\psi_V = const.$ is expressed as

$$\rho = \rho_p(\zeta) + \frac{s^2 - 1}{s_{max}^2 - 1}[\rho_w(\zeta) - \rho_p(\zeta)], \quad 1 \le s \le s_{max}. \tag{5.5}$$

From $\psi_V = \psi_p s^2$, we have

$$\psi_V = \psi_p + \psi_p(s_{max}^2 - 1)\frac{\rho - \rho_p(\zeta)}{\rho_w(\zeta) - \rho_p(\zeta)}, \tag{5.6}$$

and

$$\frac{\partial \psi_V}{\partial \rho} = \psi_p \frac{s_{max}^2 - 1}{\rho_w(\zeta) - \rho_p(\zeta)}, \tag{5.7}$$

$$\left(\frac{\partial \psi_V}{\partial \rho}\right)^{-1} \frac{\partial \psi_V}{\partial \zeta} = -\frac{\rho - \rho_p(\zeta)}{\rho_w(\zeta) - \rho_p(\zeta)} \frac{d\rho_w}{d\zeta} - \frac{\rho_w(\zeta) - \rho}{\rho_w(\zeta) - \rho_p(\zeta)} \frac{d\rho_p}{d\zeta}. \tag{5.8}$$

5.2.2 Coordinate system (ψ_V, χ, ϕ)

In general the relation between the line element dl along a contour of poloidal flux function ψ (or ψ_V) $= const.$ and a poloidal angle χ is given by

$$\frac{d\chi}{dl} = \frac{1}{\sqrt{g(\psi,\chi)}} \frac{R}{|\nabla \psi|}, \tag{5.9}$$

where $\sqrt{g(\psi,\chi)}$ is the Jacobian of the coordinate system (ψ, χ, ϕ). It is of course

$$\sqrt{g(\psi,\chi)} = R^2 \frac{q(\psi)}{F(\psi)}, \tag{5.10}$$

for the straight field line coordinate, and

$$\sqrt{g(\psi,\zeta)} = \left(\frac{\partial \psi}{\partial \rho}\right)^{-1} \rho R, \tag{5.11}$$

for the auxiliary coordinate system (ρ, ζ, ϕ). Then we have

$$\frac{d\zeta}{d\chi} = \frac{\sqrt{g(\psi,\chi)}}{\sqrt{g(\psi,\zeta)}}. \tag{5.12}$$

Especially, the transformation formula between the two angles χ and ζ at the plasma edge is

$$\Theta_p(\chi) := \left.\frac{d\zeta}{d\chi}\right|_a = \frac{q_a}{F_s} \frac{R}{\rho} \frac{\partial \psi}{\partial \rho}, \tag{5.13}$$

where

$$\frac{\partial\psi}{\partial\rho} = \frac{\partial\psi}{\partial R}\cos\zeta + \frac{\partial\psi}{\partial Z}\sin\zeta, \tag{5.14}$$

and q_a, F_s are the safety factor and toroidal field function at the plasma edge.

We define the poloidal angle χ in the vacuum by the formula (5.13) and construct the coordinate system (ψ_V, χ, ϕ). Therefore, in the coordinate transformation $(\rho,\zeta) \Leftrightarrow (\psi_V,\chi)$, we have

$$\frac{\partial\chi}{\partial\rho} = 0, \tag{5.15}$$

and the fundamental relation

$$\nabla\psi_V = \frac{\partial\psi_V}{\partial\rho}\nabla\rho + \frac{\partial\psi_V}{\partial\zeta}\nabla\zeta, \quad \nabla\chi = \frac{d\chi}{d\zeta}\nabla\zeta = \frac{1}{\Theta_p}\nabla\zeta, \tag{5.16}$$

where $\partial\psi_V/\partial\rho$ and $\partial\psi_V/\partial\zeta$ are given by Eq. (5.7) and by Eq. (5.8), respectively. Now it is easy to obtain the following quantities that are necessary to express the quadratic form for the perturbed magnetic field in the vacuum.

$$\sqrt{g_V(\psi_V,\chi)} = (\rho R)\left(\frac{\partial\psi_V}{\partial\rho}\right)^{-1}\Theta_p, \tag{5.17}$$

$$|\nabla\psi_V|^2 = \left(\frac{\partial\psi_V}{\partial\rho}\right)^2 + \frac{1}{\rho^2}\left(\frac{\partial\psi_V}{\partial\zeta}\right)^2, \tag{5.18}$$

$$\beta_{\psi\chi} := \frac{\nabla\psi_V\cdot\nabla\chi}{|\nabla\psi_V|^2} = \frac{\partial\psi_V}{\partial\zeta}\frac{1}{\rho^2\Theta_p}\frac{1}{|\nabla\psi_V|^2}, \tag{5.19}$$

and

$$\beta_{s\chi} = 2\psi_p\, s\beta_{\psi\chi}. \tag{5.20}$$

5.2.3 Construction of a solenoidal vector field $\boldsymbol{C}_V$

We can define a solenoidal vector field $(\nabla\cdot\boldsymbol{C}_V = 0)$ by

$$\boldsymbol{C}_V = \nabla\phi\times\nabla\psi_V + T_V(\psi_V,\chi)\nabla\phi, \tag{5.21}$$

by specifying T_V as a function of ψ_V,χ. The gradient of the vector field $\boldsymbol{C}_V$ is

$$\nu(\psi_V,\chi) = \frac{\boldsymbol{C}_V\cdot\nabla\phi}{\boldsymbol{C}_V\cdot\nabla\chi} = T_V\frac{\sqrt{g_V(\psi_V,\chi)}}{R^2}, \tag{5.22}$$

and the contravariant form of $\boldsymbol{C}_V$ is

$$\boldsymbol{C}_V = \nabla\phi\times\nabla\psi_V + \nu\nabla\psi_V\times\nabla\chi. \tag{5.23}$$

Since the Jacobian $\sqrt{g_V}$ has been already defined in Eq. (5.17), we can specify the function $T_V(\psi_V,\chi)$ so that ν is equal to q_s, the edge safety factor, everywhere in the vacuum; that is, we give $T_V(\psi_V,\chi)$ as

$$T_V = q_a\frac{R^2}{\sqrt{g_V(\psi_V,\chi)}} = q_a\frac{R}{\rho\Theta_p}\frac{\partial\psi_V}{\partial\rho}. \tag{5.24}$$

When we use the coordinate system (ψ_V, ζ, ϕ), we have

$$\boldsymbol{C}_V = \nabla\phi \times \nabla\psi_V + q_a \frac{d\chi}{d\zeta} \nabla\psi_V \times \nabla\zeta, \tag{5.25}$$

and

$$\nu(\psi_V, \zeta) = \frac{q_a}{\Theta_p}. \tag{5.26}$$

Here, we briefly discuss the following linear partial differential equation for $f(\psi_V, \chi, \phi)$

$$\boldsymbol{C}_V \cdot \nabla f = \alpha, \tag{5.27}$$

where we assume $f, \alpha \propto \exp(-\mathrm{i}n\phi)$, and $\alpha(\psi_V, \chi, \phi)$ is a given function. On the (ψ_V, χ, ϕ) coordinate system, Eq. (5.27) reads

$$\left(\frac{\partial}{\partial\chi} - \mathrm{i}nq_a\right) f = \sqrt{g_V(\psi_V, \chi)}\alpha. \tag{5.28}$$

The right hand side of Eq. (5.28) can be expanded as

$$\sqrt{g_V(\psi_V, \chi)}\alpha(\psi_V, \chi, \phi) = \sum_m \alpha_m(\psi_V) \exp(\mathrm{i}m\chi - \mathrm{i}n\phi), \tag{5.29}$$

then, we have

$$f_m(\psi_V) = \frac{-\mathrm{i}\alpha_m(\psi_V)}{m - nq_a}, \tag{5.30}$$

and

$$f(\psi_V, \chi, \phi) = \sum_m f_m(\psi_V) \exp(\mathrm{i}m\chi - \mathrm{i}n\phi). \tag{5.31}$$

Therefore, Eq. (5.27) has the solution as long as the edge safety factor q_a is not a rational number and the toroidal mode number n is not equal to zero.

5.3 Boundary conditions

Let us first derive the boundary condition on the ideal conducting wall. The normal component of the perturbation of magnetic field $Q_n = \boldsymbol{Q} \cdot \boldsymbol{n}$ ($\boldsymbol{n}$ in Eq. (5.41) is the unit vector normal to the plasma surface) is given, on the (ψ_V, χ, ϕ) coordinate system, by

$$Q_n = \frac{1}{|\nabla\psi_V|} \nabla\psi_V \cdot \boldsymbol{Q} = \frac{q_a}{|\nabla\psi_V| \sqrt{g_V(\psi_V, \chi)}} \mathcal{D}_\chi(X_V), \tag{5.32}$$

where

$$Y_V = \vec{\xi}_V \cdot \nabla\psi_V, \tag{5.33}$$

and

$$\mathcal{D}_\chi(Y_V) \equiv \left(\frac{1}{q_a}\frac{\partial}{\partial\chi} - \mathrm{i}n\right) Y_V, \tag{5.34}$$

which is the same definition in the plasma region Eq. (3.15). Therefore, the boundary condition $Q_n = 0$ on the ideal conducting wall is

$$Y_V(\psi_V = \text{wall}, \chi) = 0. \tag{5.35}$$

Next, we express the continuous condition of Q_n at the plasma edge by Y_V. It is convenient to use the (ψ_V, ζ, ϕ) coordinate system. From the contravariant form of $\boldsymbol{C}_V$

$$\boldsymbol{C}_V = \nabla\phi \times \nabla\psi_V + \nu(\psi_V, \zeta)\nabla\psi_V \times \nabla\zeta, \tag{5.36}$$

we obtain

$$Q_n = \frac{1}{|\nabla\psi_V|}\nabla\psi_V \cdot \boldsymbol{Q} = \frac{q_a}{|\nabla\psi_V|\sqrt{g_V(\psi_V, \zeta)}}\mathcal{D}_\zeta(Y_V), \tag{5.37}$$

where

$$\mathcal{D}_\zeta(Y_V) \equiv \frac{1}{q_a}\left(\frac{\partial}{\partial\zeta} - \mathrm{i}n\nu(\psi_V, \zeta)\right) Y_V. \tag{5.38}$$

Therefore, the continuous condition of Q_n at the plasma edge is

$$\frac{1}{|\nabla\psi_V|\sqrt{g_V(\psi_V, \zeta)}}\mathcal{D}_\zeta(Y_V) = \frac{1}{|\nabla\psi|\sqrt{g(\psi, \zeta)}}\mathcal{D}_\zeta(Y), \tag{5.39}$$

where

$$Y = \vec{\xi} \cdot \nabla\psi. \tag{5.40}$$

Here, let us remember that

$$\frac{1}{|\nabla\psi_V|\sqrt{g_V(\psi_V, \zeta)}} = \frac{1}{|\nabla\psi|\sqrt{g(\psi, \zeta)}} = \boldsymbol{n} \cdot (\nabla\zeta \times \nabla\phi), \tag{5.41}$$

since the right hand side is a quantity intrinsic to the geometry of the plasma surface. Consequently we have, as the boundary condition at the plasma edge,

$$Y_V(\psi_V, \zeta) = Y(\psi, \zeta), \tag{5.42}$$

and

$$Y_V(\psi_V, \chi) = Y(\psi, \chi). \tag{5.43}$$

5.4 Extension of the MARG2D form in the vacuum

5.4.1 Mathematical preliminaries

Let $f(\chi)$ be a real periodic function with periodicity 2π

$$f(\chi) = \sum_m f_m \exp(\mathrm{i}m\chi), \quad f_{-m} = f_m^*, \tag{5.44}$$

and $\langle\ \rangle$ and $\oint d\chi$ be operations defined by

$$\langle f\rangle = \oint f(\chi)d\chi = \frac{1}{2\pi}\int_0^{2\pi} f(\chi)d\chi. \tag{5.45}$$

For example

$$\langle f\exp(-\mathrm{i}l\chi)\rangle = f_l,\quad \langle f\exp(\mathrm{i}l\chi)\rangle = f_{-l} = f_l^*. \tag{5.46}$$

We make a vector $|\boldsymbol{f}\rangle$ from f_l's by

$$|\boldsymbol{f}\rangle = \{f_l\} = (\cdots, f_{-1}, f_0, f_1, \cdots)^t, \tag{5.47}$$

and a vector $|\hat{\boldsymbol{f}}\rangle$ by eliminating f_0 from $|\boldsymbol{f}\rangle$

$$|\hat{\boldsymbol{f}}\rangle = \{f_l\}_{l\neq 0} = (\cdots, f_{-1}, f_1, \cdots)^t. \tag{5.48}$$

We also define the conjugate vector of$|\boldsymbol{f}\rangle$ by

$$\langle\boldsymbol{f}| = (\cdots, f_{-1}^*, f_0^*, f_1^*, \cdots),\quad \langle\boldsymbol{f}|_j = f_j^*, \tag{5.49}$$

and $\langle\hat{\boldsymbol{f}}|$ similarly. Next, we introduce a matrix generated from$f(\chi)$ by

$$\mathbf{F} = \{f_{l,m}\},\quad f_{l,m} = \oint f(\chi)\exp[\mathrm{i}(m-l)\chi]d\chi = f_{l-m}. \tag{5.50}$$

Since $f(\chi)$ is real, $\mathbf{F}$ is a hermitian matrix

$$f_{m,l} = f_{l,m}^*. \tag{5.51}$$

Let $|\boldsymbol{a}\rangle, |\boldsymbol{b}\rangle$ be two vectors, and $\mathbf{A}$ be a matrix. We write the inner product of two vectors as$\langle\ |\ \rangle$

$$\langle\boldsymbol{a}|\boldsymbol{b}\rangle = \sum_l a_l^* b_l,\quad \langle\boldsymbol{a}|\boldsymbol{a}\rangle = |\boldsymbol{a}|^2, \tag{5.52}$$

and a quadratic form as

$$\langle\boldsymbol{a}|\mathbf{A}|\boldsymbol{b}\rangle = \sum_{l,m} a_l^* A_{l,m} b_m. \tag{5.53}$$

Let us notice that a matrix can be generated from the two vectors$|\boldsymbol{a}\rangle$ and $|\boldsymbol{b}\rangle$ by

$$(|\boldsymbol{a}\rangle\langle\boldsymbol{b}|)_{l,m} = (\boldsymbol{a}\otimes\boldsymbol{b}^*)_{l,m} = a_l b_m^*, \tag{5.54}$$

and the product between$\langle\boldsymbol{x}|\boldsymbol{a}\rangle$ and $\langle\boldsymbol{b}|\boldsymbol{y}\rangle$ is written by a quadratic form as

$$\langle\boldsymbol{x}|\boldsymbol{a}\rangle\langle\boldsymbol{b}|\boldsymbol{y}\rangle := \langle\boldsymbol{x}|\boldsymbol{a}\otimes\boldsymbol{b}^*|\boldsymbol{y}\rangle. \tag{5.55}$$

Let $a_j(\chi)$ $(j = 1, \cdots, N)$ be complex functions of the variableχ and $|\boldsymbol{a}(\chi))$ be a vector function defined by

$$|\boldsymbol{a}(\chi)) = (a_1(\chi), \cdots, a_N(\chi))^t,\quad |\boldsymbol{a}(\chi))_j = a_j(\chi). \tag{5.56}$$

The conjugate vector function $(\boldsymbol{a}(\chi)|$ is defined by

$$(\boldsymbol{a}(\chi)| = (a_1^*(\chi), \cdots, a_N^*(\chi)), \quad (\boldsymbol{a}(\chi)|_j = a_j^*(\chi). \tag{5.57}$$

Then a function $f(\chi)$ given by

$$f(\chi) = \sum_{j=1}^{N} f_j a_j^*(\chi), \tag{5.58}$$

can be expressed by an inner product form as

$$f(\chi) = (\boldsymbol{a}(\chi)|\boldsymbol{f}\rangle. \tag{5.59}$$

From Eq. (5.59) we obtain

$$|f(\chi)|^2 = \sum_{j,k} f_j^* a_j(\chi) a_k^*(\chi) f_k = \langle \boldsymbol{f}|\boldsymbol{a}(\chi))(\boldsymbol{a}(\chi)|\boldsymbol{f}\rangle, \tag{5.60}$$

and

$$\langle |f(\chi)|^2\rangle = \oint |f(\chi)|^2 d\chi = \langle \boldsymbol{f}|\mathbf{A}|\boldsymbol{f}\rangle. \tag{5.61}$$

Here the matrix $\mathbf{A} = (A_{j,k})$ is given by

$$A_{j,k} = \oint a_j(\chi) a_k^*(\chi) d\chi, \tag{5.62}$$

and is a hermitian matrix. It can be also written as

$$\oint |\boldsymbol{a}(\chi))(\boldsymbol{a}(\chi)|d\chi = \mathbf{A}. \tag{5.63}$$

Next, for two functions

$$f(\chi) = (\boldsymbol{a}(\chi)|\boldsymbol{f}\rangle, \quad g(\chi) = (\boldsymbol{a}(\chi)|\boldsymbol{g}\rangle, \tag{5.64}$$

we write the inner product of them as

$$(f|g) = \oint f^*(\chi) g(\chi) d\chi, \tag{5.65}$$

and we have

$$(f|g) = \langle \boldsymbol{f}|\mathbf{A}|\boldsymbol{g}\rangle. \tag{5.66}$$

Let $b(\chi)$ be another function, then we obtain

$$\langle b(\chi) f(\chi)\rangle = \langle \boldsymbol{b}|\boldsymbol{f}\rangle, \tag{5.67}$$

where

$$|\boldsymbol{b}\rangle = \oint b(\chi)|\boldsymbol{a}(\chi))d\chi. \tag{5.68}$$

We also obtain

$$\langle b(\chi)|f(\chi)|^2\rangle = \langle \boldsymbol{f}|\mathbf{B}|\boldsymbol{f}\rangle. \tag{5.69}$$

Here the matrix $\mathbf{B} = (B_{j,k})$ is given by

$$\mathbf{B} = \oint |\boldsymbol{a}(\chi))b(\chi)(\boldsymbol{a}(\chi)|d\chi, \quad \mathrm{B}_{j,k} = \oint a_j(\chi)b(\chi)a_k^*(\chi)d\chi. \tag{5.70}$$

In this chapter, $\{\exp(-\mathrm{i}j\chi)\}$ are used as $\{a_j(\chi)\}$

$$|\boldsymbol{e}(\chi)) = (\cdots, \exp(\mathrm{i}j\chi), \cdots, 1, \cdots \exp(-\mathrm{i}j\chi), \cdots)^t, \tag{5.71}$$

$$|\boldsymbol{e}(\chi))_j = \exp(-\mathrm{i}j\chi). \tag{5.72}$$

We also use the vector $|\hat{\boldsymbol{e}}(\chi))$ that is made by eliminating the $j = 0$ component from $|\boldsymbol{e}(\chi))$. Since

$$\oint |\boldsymbol{e}(\chi))(\boldsymbol{e}(\chi)|d\chi = \mathbf{I}, \tag{5.73}$$

where $\mathbf{I}$ is the unit matrix, we obtain for Eq. (5.66)

$$(f|g) = \langle \boldsymbol{f}|\boldsymbol{g}\rangle. \tag{5.74}$$

We use repeatedly in this paper the following propositions on a quadratic form. A real function of a complex number z, $L(z)$, is introduced as

$$L(z) = a|z|^2 + b^*z + z^*b, \tag{5.75}$$

where a is real and b is complex. Then $L(z)$ takes its extremum

$$L(z) = -\frac{|b|^2}{a}, \tag{5.76}$$

at $z = -b/a$. Next, let $L(\boldsymbol{x})$ be a real quadratic form for a complex vector $\boldsymbol{x}$

$$L(\boldsymbol{x}) = \langle \boldsymbol{x}|\mathbf{A}|\boldsymbol{x}\rangle + \langle \boldsymbol{x}|\boldsymbol{b}\rangle + \langle \boldsymbol{b}|\boldsymbol{x}\rangle, \tag{5.77}$$

where $\mathbf{A}$ is a hermitian matrix and $\boldsymbol{b}$ is a complex vector. $L(\boldsymbol{x})$ takes its extremum

$$L(\boldsymbol{x}) = -\langle \boldsymbol{b}|\mathbf{A}^{-1}|\boldsymbol{b}\rangle, \tag{5.78}$$

for $\boldsymbol{x} = -\mathbf{A}^{-1}\boldsymbol{b}$.

5.4.2 Quadratic form for the change of potential energy in the vacuum

The perturbation of magnetic field in the vacuum is expressed by

$$\boldsymbol{Q} = \nabla \times \boldsymbol{A}, \quad \boldsymbol{A} = \boldsymbol{\xi} \times \boldsymbol{C}_V. \tag{5.79}$$

By introducing Y, V as

$$Y = \boldsymbol{\xi}_V \cdot \nabla\psi_V, \quad V = \boldsymbol{\xi}_V \cdot \nabla\theta - \frac{1}{q_a}\boldsymbol{\xi}_V \cdot \nabla\phi, \tag{5.80}$$

we have

$$\boldsymbol{A} = Y(\nabla\phi - q_a\nabla\theta) + q_a V\nabla\psi_V, \tag{5.81}$$

$$\boldsymbol{Q} = u_\psi \nabla\theta \times \nabla\phi + u_\theta \nabla\phi \times \nabla\psi_V + u_\phi \nabla\psi_V \times \nabla\theta. \tag{5.82}$$

Here

$$u_\psi = q_a \mathcal{D}_\theta(Y), \tag{5.83}$$

$$u_\theta = -\left[\frac{\partial Y}{\partial \psi_V} + \mathrm{i}nq_a V\right], \tag{5.84}$$

$$u_\phi = -q_a\left[\frac{\partial V}{\partial \theta} + \frac{\partial Y}{\partial \psi_V}\right], \tag{5.85}$$

and

$$\mathcal{D}_\theta(Y) = \left(\frac{1}{q_a}\frac{\partial}{\partial\theta} - \mathrm{i}n\right)Y. \tag{5.86}$$

Therefore, when the energy integral of the perturbed magnetic field is written by

$$W_V = \pi \int \mathcal{L}_V d\psi_V d\chi, \quad \mathcal{L}_V = \sqrt{g_V}|\boldsymbol{Q}|^2, \tag{5.87}$$

the potential energy density $\mathcal{L}_V$ is given by

$$\mathcal{L}_V = a|\mathcal{D}_\theta(Y)|^2 + b\left|\mathrm{i}nV + \frac{1}{q_a}\frac{\partial Y}{\partial \psi_V} + \beta_{\psi\theta}\mathcal{D}_\theta(Y)\right|^2 + c\left|\frac{\partial V}{\partial\theta} + \frac{\partial Y}{\partial\psi_V}\right|^2, \tag{5.88}$$

and the coefficients a, b, c in Eq. (5.88) are

$$a(\psi_V, \theta) = \frac{q_a^2}{|\nabla\psi_V|^2}\frac{1}{\sqrt{g_V}} = q_a\frac{T_V}{R^2|\nabla\psi_V|^2}, \tag{5.89}$$

$$b(\psi_V, \theta) = q_a^2\frac{|\nabla\psi_V|^2}{R^2}\sqrt{g_V} = \frac{q_a^3}{T_V}|\nabla\psi_V|^2, \tag{5.90}$$

$$c(\psi_V, \theta) = q_a^2\frac{R^2}{\sqrt{g_V}} = q_a T_V. \tag{5.91}$$

In the following we write, for simplicity, ψ instead of ψ_V. Let us introduce a new variable $\Phi(\psi, \chi)$ by

$$\Phi = \frac{\partial V}{\partial \chi} + \frac{\partial Y}{\partial \psi}, \tag{5.92}$$

and expand the variables in Fourier series as

$$V(\psi, \chi) = (-\mathrm{i})\sum_m V_m(\psi)\exp(\mathrm{i}m\chi), \tag{5.93}$$

$$(Y(\psi, \chi), \Phi(\psi, \chi)) = \sum_m (Y_m(\psi), \Phi_m(\psi))\exp(\mathrm{i}m\chi). \tag{5.94}$$

Consequently, we obtain

$$V_m(\psi) = \frac{1}{m}\Phi_m - \frac{1}{m}\frac{dY_m}{d\psi}, \quad \text{for } m \neq 0, \tag{5.95}$$

$$\Phi_0(\psi) = \frac{dY_0}{d\psi}, \quad \text{for } m = 0, \tag{5.96}$$

and

$$\frac{\partial V}{\partial \chi} + \frac{\partial Y}{\partial \psi} = \sum_m{}' \Phi_m \exp(\mathrm{i}m\chi) + \frac{dY_0}{d\psi} = (\hat{\boldsymbol{e}}(\chi)|\hat{\boldsymbol{\Phi}}\rangle + \frac{dY_0}{d\psi}. \tag{5.97}$$

Here we use the notations by Eqs. (5.71) and (5.59). By substituting Eq. (5.97) into the third term in Eq. (5.88), we have

$$\begin{aligned} c(\chi)\left|\frac{\partial V}{\partial \chi} + \frac{\partial Y}{\partial \psi}\right|^2 &= \langle\hat{\boldsymbol{\Phi}}|\hat{\mathbf{e}}(\chi))c(\chi)(\hat{\mathbf{e}}(\chi)|\hat{\boldsymbol{\Phi}}\rangle + \left|\frac{dY_0}{d\psi}\right|^2 c(\chi) \\ &\quad + \frac{dY_0^*}{d\psi}c(\chi)(\hat{\mathbf{e}}(\chi)|\hat{\boldsymbol{\Phi}}\rangle + \langle\hat{\boldsymbol{\Phi}}|\hat{\mathbf{e}}(\chi))c(\chi)\frac{dY_0}{d\psi}, \end{aligned} \tag{5.98}$$

and then

$$\oint c(\chi)\left|\frac{\partial V}{\partial \chi} + \frac{\partial Y}{\partial \psi}\right|^2 d\chi = \langle\hat{\boldsymbol{\Phi}}|\mathbf{C}|\hat{\boldsymbol{\Phi}}\rangle + \langle c\rangle\left|\frac{dY_0}{d\psi}\right|^2 + \frac{dY_0^*}{d\psi}\langle\boldsymbol{c}|\hat{\boldsymbol{\Phi}}\rangle + \frac{dY_0}{d\psi}\langle\hat{\boldsymbol{\Phi}}|\boldsymbol{c}\rangle. \tag{5.99}$$

Here, $\langle c\rangle$ is defined by Eq. (5.45),

$$\mathbf{C} = \oint |\hat{\boldsymbol{e}}(\chi))c(\chi)(\hat{\boldsymbol{e}}(\chi)|d\chi, \tag{5.100}$$

and

$$\boldsymbol{c} = \oint c(\chi)|\hat{\boldsymbol{e}}(\chi))d\chi. \tag{5.101}$$

Next, by using Eq. (5.95) in the second term in Eq. (5.88), we obtain

$$\begin{aligned} &\frac{\partial Y}{\partial \psi} + \mathrm{i}nq_a V + q_a\beta_{\psi\chi}\mathcal{D}_\chi(Y) \\ &\quad = \left(\hat{\boldsymbol{e}}(\chi)\left|\mathrm{Diag}\left(\frac{nq_a}{m}\right)\hat{\boldsymbol{\Phi}}\right\rangle + nq_a V_0\right. \\ &\quad\quad + \left(\hat{\boldsymbol{e}}(\chi)\left|\bar{\mathbf{D}}_V\frac{d\hat{\boldsymbol{Y}}}{d\psi}\right\rangle + \mathrm{i}q_a\beta_{\psi\chi}(\psi,\chi)(\boldsymbol{e}(\chi)|\mathbf{D}_V\boldsymbol{Y}\rangle + \frac{dY_0}{d\psi}. \end{aligned} \tag{5.102}$$

Here $\mathbf{D}_V$ and $\bar{\mathbf{D}}_V$ are diagonal matrices; they are

$$\mathbf{D}_V = \mathrm{Diag}\left(\frac{m}{q_a} - n\right), \tag{5.103}$$

$$\bar{\mathbf{D}}_V := \mathrm{Diag}\left(1 - \frac{nq_a}{m}\right) = \mathbf{D}_V\mathrm{Diag}\left(\frac{q_a}{m}\right). \tag{5.104}$$

Consequently, the second term in Eq. (5.88) is

$$\begin{aligned} &\oint b(\chi)\left|\frac{\partial Y}{\partial \psi} + \mathrm{i}nq_a V + q_a\beta_{\psi\chi}\mathcal{D}_\chi(Y)\right|^2 d\chi \\ &\quad = \oint d\chi\left[\left\langle\hat{\boldsymbol{\Phi}}\mathrm{Diag}\left(\frac{nq_a}{l}\right)|\hat{\boldsymbol{e}}(\chi)\right\rangle + nq_a V_0^* + f^*(\chi)\right] \\ &\quad\quad \times b(\chi)\left[\left(\hat{\boldsymbol{e}}(\chi)\left|\mathrm{Diag}\left(\frac{nq_a}{m}\right)\hat{\boldsymbol{\Phi}}\right\rangle + nq_a V_0 + f(\chi)\right.\right], \end{aligned} \tag{5.105}$$

where

$$f(\chi) = \left(\hat{\boldsymbol{e}}(\chi)\left|\bar{\mathbf{D}}_V\frac{d\hat{\boldsymbol{Y}}}{d\psi}\right.\right\rangle + \mathrm{i}q_a\beta_{\psi\chi}(\psi,\chi)(\boldsymbol{e}(\chi)|\mathbf{D}_V\boldsymbol{Y}\rangle + \frac{dY_0}{d\psi}. \tag{5.106}$$

Here we introduce the following vectors and matrices for later use:

$$\hat{\boldsymbol{b}} = \oint b(\chi)|\hat{\boldsymbol{e}}(\chi))d\chi, \tag{5.107}$$

$$\mathbf{B} = \oint |\hat{\boldsymbol{e}}(\chi))b(\chi)(\hat{\boldsymbol{e}}(\chi)|d\chi, \tag{5.108}$$

$$\boldsymbol{h} = \oint [(-\mathrm{i})b(\chi)\beta_{\psi\chi}(\chi)]|\boldsymbol{e}(\chi))d\chi, \tag{5.109}$$

$$\mathbf{H} = \oint |\hat{\boldsymbol{e}}(\chi))[\mathrm{i}b(\chi)\beta_{\psi\chi}(\chi)](\boldsymbol{e}(\chi)|d\chi, \tag{5.110}$$

and

$$\hat{\boldsymbol{b}}_{\mathrm{f}} = \oint |\hat{\boldsymbol{e}}(\chi))b(\chi)f(\chi)d\chi = \left|\mathbf{B}\bar{\mathbf{D}}_V\left|\frac{d\hat{\boldsymbol{Y}}}{d\psi}\right.\right\rangle + \frac{dY_0}{d\psi}\hat{\boldsymbol{b}} + q_a|\mathbf{H}\mathbf{D}_V|\boldsymbol{Y}\rangle. \tag{5.111}$$

5.4.3 Minimization with respect to V_0 and Φ_m

We first minimize with respect to V_0 the integral (5.105), which can be written in a quadratic form for V_0,

$$\mathcal{F}(V_0) = (nq_a)^2\langle b\rangle|V_0|^2 + (nq_a)(V_0^*\alpha + \alpha^*V_0) + \kappa. \tag{5.112}$$

Here the coefficients α and κ are given by

$$\begin{aligned}\alpha &= \oint d\chi b(\chi)\left[\left(\hat{\boldsymbol{e}}(\chi)\left|\mathrm{Diag}\left(\frac{nq_a}{m}\right)\hat{\boldsymbol{\Phi}}\right.\right\rangle + f(\chi)\right]\\ &= \left\langle\hat{\boldsymbol{b}}\left|\mathrm{Diag}\left(\frac{nq_a}{m}\right)\hat{\boldsymbol{\Phi}}\right.\right\rangle + \langle b(\chi)f(\chi)\rangle,\end{aligned} \tag{5.113}$$

$$\langle b(\chi)f(\chi)\rangle = \left\langle\hat{\boldsymbol{b}}\left|\bar{\mathbf{D}}_V\left|\frac{d\hat{\boldsymbol{Y}}}{d\psi}\right.\right.\right\rangle + \langle b\rangle\frac{dY_0}{d\psi} + q_a\langle\boldsymbol{h}|\mathbf{D}_V|\boldsymbol{Y}\rangle, \tag{5.114}$$

and

$$\begin{aligned}\kappa = &\oint d\chi\left[\left\langle\hat{\boldsymbol{\Phi}}\mathrm{Diag}\left(\frac{nq_a}{l}\right)\right|\hat{\boldsymbol{e}}(\chi)\right) + f^*(\chi)\right]\\ &\times b(\chi)\left[\left(\hat{\boldsymbol{e}}(\chi)\left|\mathrm{Diag}\left(\frac{nq_a}{m}\right)\hat{\boldsymbol{\Phi}}\right.\right\rangle + f(\chi)\right].\end{aligned} \tag{5.115}$$

By applying Eq. (5.76), we obtain the minimum of $\mathcal{F}$ with respect to V_0

$$\min\mathcal{F} = -\frac{1}{\langle b\rangle}|\alpha|^2 + \kappa. \tag{5.116}$$

Next, we express Eq. (5.116) in a quadratic form with respect to $\hat{\mathbf{\Phi}}$. We obtain for Eq. (5.113)

$$
\begin{aligned}
|\alpha|^2 = (nq_a)^2 \left\langle \hat{\mathbf{\Phi}} \left| \mathrm{Diag}\left(\frac{1}{m}\right) \hat{\boldsymbol{b}} \otimes \hat{\boldsymbol{b}}^* \mathrm{Diag}(\frac{1}{m}) \right| \hat{\mathbf{\Phi}} \right\rangle + |\langle b(\chi) f(\chi) \rangle|^2 \\
+ \; nq_a \langle b(\chi) f(\chi) \rangle^* \left\langle \hat{\boldsymbol{b}} \left| \mathrm{Diag}\left(\frac{1}{m}\right) \right| \hat{\mathbf{\Phi}} \right\rangle \\
+ \; nq_a \left\langle \hat{\mathbf{\Phi}} \left| \mathrm{Diag}\left(\frac{1}{m}\right) \right| \hat{\boldsymbol{b}} \right\rangle \langle b(\chi) f(\chi) \rangle,
\end{aligned} \tag{5.117}
$$

and for Eq. (5.115)

$$
\begin{aligned}
\kappa = (nq_a)^2 \left\langle \hat{\mathbf{\Phi}} \left| \mathrm{Diag}\left(\frac{1}{m}\right) \mathbf{B} \mathrm{Diag}\left(\frac{1}{m}\right) \right| \hat{\mathbf{\Phi}} \right\rangle + nq_a \left\langle \hat{\mathbf{\Phi}} \left| \mathrm{Diag}\left(\frac{1}{m}\right) \right| \hat{\boldsymbol{b}}_{\mathrm{f}} \right\rangle \\
+ \; nq_a \left\langle \hat{\boldsymbol{b}}_{\mathrm{f}} \left| \mathrm{Diag}\left(\frac{1}{m}\right) \right| \hat{\mathbf{\Phi}} \right\rangle + \langle b(\chi) | f(\chi) |^2 \rangle,
\end{aligned} \tag{5.118}
$$

where $|\hat{\boldsymbol{b}}_{\mathrm{f}}\rangle$ is defined in Eq. (5.111). Let us notice that

$$
\frac{\langle b(\chi) f(\chi) \rangle}{\langle b \rangle} |\hat{\boldsymbol{b}}\rangle = \frac{1}{\langle b \rangle} \left| \hat{\boldsymbol{b}} \otimes \hat{\boldsymbol{b}}^* \right| \bar{\mathbf{D}}_V \frac{d\hat{\boldsymbol{Y}}}{d\psi} \right\rangle + q_a \frac{1}{\langle b \rangle} |\hat{\boldsymbol{b}} \otimes \boldsymbol{b}^* | \mathbf{D}_V \boldsymbol{Y} \rangle + \frac{dY_0}{d\psi} |\hat{\boldsymbol{b}}\rangle. \tag{5.119}
$$

Here we use Eq. (5.54). Then $\min \mathcal{F}$ in Eq. (5.116) is rewritten as

$$
\begin{aligned}
\min \mathcal{F} = (nq_a)^2 \left\langle \hat{\mathbf{\Phi}} \left| \mathrm{Diag}\left(\frac{1}{l}\right) \bar{\mathbf{B}} \mathrm{Diag}\left(\frac{1}{l}\right) \right| \hat{\mathbf{\Phi}} \right\rangle + nq_a \left\langle \hat{\mathbf{\Phi}} \left| \mathrm{Diag}\left(\frac{1}{l}\right) \right| \bar{\boldsymbol{b}}_{\mathrm{f}} \right\rangle \\
+ \; nq_a \left\langle \bar{\boldsymbol{b}}_{\mathrm{f}} \left| \mathrm{Diag}\left(\frac{1}{l}\right) \right| \hat{\mathbf{\Phi}} \right\rangle + \langle b(\chi) | f(\chi) |^2 \rangle - \frac{|\langle b(\chi) f(\chi) \rangle|^2}{\langle b \rangle},
\end{aligned} \tag{5.120}
$$

where

$$
\bar{\mathbf{B}} = \mathbf{B} - \frac{1}{\langle b \rangle} \hat{\boldsymbol{b}} \otimes \hat{\boldsymbol{b}}^*, \tag{5.121}
$$

$$
\bar{\boldsymbol{b}}_{\mathrm{f}} = \hat{\boldsymbol{b}}_{\mathrm{f}} - \frac{\langle b(\chi) f(\chi) \rangle}{\langle b \rangle} \hat{\boldsymbol{b}} = \left| \bar{\mathbf{B}} \bar{\mathbf{D}}_V \left| \frac{d\hat{\boldsymbol{Y}}}{d\psi} \right\rangle + q_a |\mathbf{H}_B \mathbf{D}_V | \boldsymbol{Y} \right\rangle, \tag{5.122}
$$

$$
\mathbf{H}_B = \mathbf{H} - \frac{1}{\langle b \rangle} \hat{\boldsymbol{b}} \otimes \boldsymbol{h}^*. \tag{5.123}
$$

In Eq. (5.120) the term including $dY_0/d\psi$ has been canceled out.

When we use Eqs. (5.99) and (5.120), we obtain a quadratic form with respect to $\hat{\mathbf{\Phi}}$ generated from Eqs. (5.87) and (5.88)

$$
\begin{aligned}
\mathcal{L}_V = \oint c(\chi) \left| \frac{\partial V}{\partial \chi} + \frac{\partial Y}{\partial \psi_V} \right|^2 d\chi + \oint b(\chi) \left| \frac{\partial Y}{\partial \psi} + \mathrm{i} n q_a V + q_a \beta_{\psi\chi} \mathcal{D}_\chi(Y) \right|^2 d\chi \\
= \langle \hat{\mathbf{\Phi}} | \mathbf{P} | \hat{\mathbf{\Phi}} \rangle + \langle \boldsymbol{d} | \hat{\mathbf{\Phi}} \rangle + \langle \hat{\mathbf{\Phi}} | \boldsymbol{d} \rangle + \langle c(\chi) \rangle \left| \frac{dY_0}{d\psi} \right|^2 + \bar{e}.
\end{aligned} \tag{5.124}
$$

Here $\mathbf{P}$, $\boldsymbol{d}$ and $\bar{e}$ are given by

$$\mathbf{P} = \mathbf{C} + \mathrm{Diag}\left(\frac{nq_a}{l}\right)\bar{\mathbf{B}}\mathrm{Diag}\left(\frac{nq_a}{l}\right), \tag{5.125}$$

$$\boldsymbol{d} = \frac{dY_0}{d\psi}\boldsymbol{c} + \mathrm{Diag}\left(\frac{nq_a}{l}\right)\bar{\boldsymbol{b}}_f, \tag{5.126}$$

and

$$\bar{e} = \langle b(\chi)|f(\chi)|^2\rangle - \frac{|\langle b(\chi)f(\chi)\rangle|^2}{\langle b\rangle}. \tag{5.127}$$

Now, it is easy to minimize $\mathcal{L}_V$ with respect to $\hat{\mathbf{\Phi}}$, and we obtain

$$\min \mathcal{L}_V = -\langle \boldsymbol{d}|\mathbf{P}^{-1}|\boldsymbol{d}\rangle + \langle c(\chi)\rangle\left|\frac{dY_0}{d\psi}\right|^2 + \bar{e}. \tag{5.128}$$

5.4.4 Quadratic form with respect to $\boldsymbol{Y}$

Let us first express $\bar{e}$ in a quadratic form with respect to $\boldsymbol{Y}$. From Eq. (5.106),

$$\begin{aligned}
|f(\psi,\chi)|^2 = &\left\langle \frac{d\hat{\boldsymbol{Y}}}{d\psi}\left|\bar{\mathbf{D}}_V\right|\hat{\boldsymbol{e}}(\chi))(\hat{\boldsymbol{e}}(\chi)|\left.\bar{\mathbf{D}}_V\right|\frac{d\hat{\boldsymbol{Y}}}{d\psi}\right\rangle \\
&+ q_a^2\left|\beta_{\psi,\chi}\right|^2\langle \boldsymbol{Y}|\mathbf{D}_V|\boldsymbol{e}(\chi))(\boldsymbol{e}(\chi)|\mathbf{D}_V|\boldsymbol{Y}\rangle + \left|\frac{dY_0}{d\psi}\right|^2 \\
&+ \mathrm{i}q_a\beta_{\psi,\chi}\left\langle \frac{d\boldsymbol{Y}}{d\psi}\left|\bar{\mathbf{D}}_V\right|\hat{\boldsymbol{e}}(\chi)\right\rangle(\boldsymbol{e}(\chi)\,|\mathbf{D}_V|\,\boldsymbol{Y}\rangle \\
&- \mathrm{i}q_a\beta_{\psi,\chi}\,\langle \boldsymbol{Y}\,|\mathbf{D}_V|\,\boldsymbol{e}(\chi))\left(\hat{\boldsymbol{e}}(\chi)\left|\bar{\mathbf{D}}_V\right|\frac{d\hat{\boldsymbol{Y}}}{d\psi}\right\rangle \\
&+ \frac{dY_0^*}{d\psi}\left\langle \hat{\boldsymbol{e}}(\chi)\left|\bar{\mathbf{D}}_V\right|\frac{d\hat{\boldsymbol{Y}}}{d\psi}\right\rangle + \left\langle \frac{d\hat{\boldsymbol{Y}}}{d\psi}\left|\bar{\mathbf{D}}_V\right|\hat{\boldsymbol{e}}(\chi)\right\rangle\frac{dY_0}{d\psi} \\
&+ \mathrm{i}q_a\beta_{\psi,\chi}\frac{dY_0^*}{d\psi}(\boldsymbol{e}(\chi)|\mathbf{D}_V|\boldsymbol{Y}\rangle - \mathrm{i}q_a\beta_{\psi,\chi}\langle \boldsymbol{Y}|\mathbf{D}_V|\boldsymbol{e}(\chi))\frac{dY_0}{d\psi}.
\end{aligned} \tag{5.129}$$

Consequently, we have

$$\begin{aligned}
\langle b(\psi,\chi)\,|f(\psi,\chi)|^2\rangle = &\left\langle \frac{d\hat{\boldsymbol{Y}}}{d\psi}\left|\bar{\mathbf{D}}_V\mathbf{B}\bar{\mathbf{D}}_V\right|\frac{d\hat{\boldsymbol{Y}}}{d\psi}\right\rangle + q_a^2\langle \boldsymbol{Y}|\mathbf{D}_V\mathbf{H}_2\mathbf{D}_V|\boldsymbol{Y}\rangle + \langle b\rangle\left|\frac{dY_0}{d\psi}\right|^2 \\
&+ q_a\left\langle \frac{d\boldsymbol{Y}}{d\psi}\left|\bar{\mathbf{D}}_V\mathbf{H}\mathbf{D}_V\right|\boldsymbol{Y}\right\rangle + q_a\left\langle \boldsymbol{Y}\left|\mathbf{D}_V\mathbf{H}^\dagger\bar{\mathbf{D}}_V\right|\frac{d\hat{\boldsymbol{Y}}}{d\psi}\right\rangle \\
&+ \frac{dY_0^*}{d\psi}\left\langle \hat{\boldsymbol{b}}\left|\bar{\mathbf{D}}_V\right|\frac{d\hat{\boldsymbol{Y}}}{d\psi}\right\rangle + \left\langle \frac{d\hat{\boldsymbol{Y}}}{d\psi}\left|\bar{\mathbf{D}}_V\right|\hat{\boldsymbol{b}}\right\rangle\frac{dY_0}{d\psi} \\
&+ q_a\frac{dY_0^*}{d\psi}\langle \boldsymbol{h}\,|\mathbf{D}_V|\,\boldsymbol{Y}\rangle + q_a\langle \boldsymbol{Y}|\mathbf{D}_V|\boldsymbol{h}\rangle\frac{dY_0}{d\psi}.
\end{aligned} \tag{5.130}$$

Here $\boldsymbol{b}$, $\mathbf{B}$, $\boldsymbol{h}$ and $\mathbf{H}$ are given from Eqs. (5.107)-(5.110);$\mathbf{H}_2$ is defined by

$$\mathbf{H}_2 = \oint |\boldsymbol{e}(\chi))[b(\chi)\left|\beta_{\psi\chi}\right|^2](\boldsymbol{e}(\chi)|d\chi. \tag{5.131}$$

Similarly,

$$\langle b(\psi,\chi)f(\psi,\chi)\rangle = \left\langle \hat{\boldsymbol{b}} \left| \bar{\mathbf{D}}_V \right| \frac{d\hat{\boldsymbol{Y}}}{d\psi} \right\rangle + q_a \langle \boldsymbol{h}|\mathbf{D}|\boldsymbol{Y}\rangle + \langle b\rangle \frac{dY_0}{d\psi}, \tag{5.132}$$

then we obtain

$$\begin{aligned}
|\langle b(\psi,\chi)f(\psi,\chi)\rangle|^2 = {} & \left\langle \frac{d\hat{\boldsymbol{Y}}}{d\psi} \left| \bar{\mathbf{D}}_V \hat{\boldsymbol{b}} \otimes \hat{\boldsymbol{b}}^* \bar{\mathbf{D}}_V \right| \frac{d\hat{\boldsymbol{Y}}}{d\psi} \right\rangle \\
& + q_a^2 \langle \boldsymbol{Y}|\mathbf{D}_V \boldsymbol{h} \otimes \boldsymbol{h}^* \mathbf{D}_V|\boldsymbol{Y}\rangle + |\langle b\rangle|^2 \left| \frac{dY_0}{d\psi} \right|^2 \\
& + q_a \left\langle \boldsymbol{Y} \left| \mathbf{D}_V \boldsymbol{h} \otimes \hat{\boldsymbol{b}}^* \bar{\mathbf{D}}_V \right| \frac{d\hat{\boldsymbol{Y}}}{d\psi} \right\rangle \\
& + q_a \left\langle \frac{d\bar{\boldsymbol{Y}}}{d\psi} \left| \bar{\mathbf{D}}_V \hat{\boldsymbol{b}} \otimes \boldsymbol{h}^* \mathbf{D}_V \right| \boldsymbol{Y} \right\rangle \\
& + q_a \langle b\rangle \left\{ \langle \boldsymbol{Y}|\mathbf{D}_V|\boldsymbol{h}\rangle \frac{dY_0}{d\psi} + \frac{dY_0^*}{d\psi} \langle \boldsymbol{h}|\mathbf{D}_V|\boldsymbol{Y}\rangle \right\} \\
& + \langle b\rangle \left\{ \frac{dY_0^*}{d\psi} \left\langle \hat{\boldsymbol{b}} \left| \bar{\mathbf{D}}_V \right| \frac{d\hat{\boldsymbol{Y}}}{d\psi} \right\rangle + \left\langle \frac{d\hat{\boldsymbol{Y}}}{d\psi} \left| \bar{\mathbf{D}}_V \right| \hat{\boldsymbol{b}} \right\rangle \frac{dY_0}{d\psi} \right\}.
\end{aligned} \tag{5.133}$$

By substituting Eqs. (5.130) and (5.133) into Eq. (5.127), we obtain

$$\begin{aligned}
\bar{e} = {} & \left\langle \frac{d\hat{\boldsymbol{Y}}}{d\psi} \left| \bar{\mathbf{D}}_V \bar{\mathbf{B}} \bar{\mathbf{D}}_V \right| \frac{d\hat{\boldsymbol{Y}}}{d\psi} \right\rangle + q_a^2 \langle \boldsymbol{Y}|\mathbf{D}_V \bar{\mathbf{H}}_2 \mathbf{D}_V|\boldsymbol{Y}\rangle \\
& + q_a \left\langle \frac{d\boldsymbol{Y}}{d\psi} \left| \bar{\mathbf{D}}_V \mathbf{H}_B \mathbf{D}_V \right| \boldsymbol{Y} \right\rangle + q_a \left\langle \boldsymbol{Y} \left| \mathbf{D}_V \mathbf{H}_B^\dagger \bar{\mathbf{D}}_V \right| \frac{d\hat{\boldsymbol{Y}}}{d\psi} \right\rangle,
\end{aligned} \tag{5.134}$$

where

$$\bar{\mathbf{H}}_2 = \mathbf{H}_2 - \frac{1}{\langle b\rangle} \boldsymbol{h} \otimes \boldsymbol{h}^*. \tag{5.135}$$

Next, by using Eq. (5.126) for the first term in Eq. (5.128) we have

$$\begin{aligned}
\langle \boldsymbol{d}|\mathbf{P}^{-1}|\boldsymbol{d}\rangle = {} & \left| \frac{dY_0}{d\psi} \right|^2 \langle \boldsymbol{c}|\mathbf{P}^{-1}|\boldsymbol{c}\rangle \\
& + \left(\frac{dY_0}{d\psi} \right)^* \left\langle \boldsymbol{c} \left| \mathbf{P}^{-1} \mathrm{Diag}\left(\frac{nq_a}{l} \right) \right| \bar{\boldsymbol{b}}_f \right\rangle \\
& + \left(\frac{dY_0}{d\psi} \right) \left\langle \bar{\boldsymbol{b}}_f \left| \mathrm{Diag}\left(\frac{nq_a}{l} \right) \mathbf{P}^{-1} \right| \boldsymbol{c} \right\rangle \\
& + \left\langle \bar{\boldsymbol{b}}_f \left| \mathrm{Diag}\left(\frac{nq_a}{l} \right) \mathbf{P}^{-1} \mathrm{Diag}\left(\frac{nq_a}{l} \right) \right| \bar{\boldsymbol{b}}_f \right\rangle.
\end{aligned} \tag{5.136}$$

When we use Eq. (5.122) for $\bar{\boldsymbol{b}}_f$, we obtain

$$\begin{aligned}
& \left\langle \boldsymbol{c} \left| \mathbf{P}^{-1} \mathrm{Diag}\left(\frac{nq_a}{l} \right) \right| \bar{\boldsymbol{b}}_f \right\rangle \\
& = \left\langle \boldsymbol{c} \left| \mathbf{P}^{-1} \mathrm{Diag}\left(\frac{nq_a}{l} \right) \bar{\mathbf{B}} \bar{\mathbf{D}}_V \right| \frac{d\hat{\boldsymbol{Y}}}{d\psi} \right\rangle + q_a \left\langle \boldsymbol{c} \left| \mathbf{P}^{-1} \mathrm{Diag}\left(\frac{nq_a}{l} \right) \mathbf{H}_B \mathbf{D}_V \right| \boldsymbol{Y} \right\rangle,
\end{aligned} \tag{5.137}$$

and

$$\begin{aligned}
&\left\langle \bar{\boldsymbol{b}}_f \left| \mathrm{Diag}\left(\frac{nq_a}{l}\right)\mathbf{P}^{-1}\mathrm{Diag}\left(\frac{nq_a}{m}\right)\right| \bar{\boldsymbol{b}}_f \right\rangle \\
&= \left\langle \frac{d\hat{\boldsymbol{Y}}}{d\psi}\left|\bar{\mathbf{D}}_V\bar{\mathbf{B}}^{\dagger}\mathbf{R}\bar{\mathbf{B}}\bar{\mathbf{D}}_V\right|\frac{d\hat{\boldsymbol{Y}}}{d\psi}\right\rangle + q_a\left\langle \boldsymbol{Y}\left|\mathbf{D}_V\mathbf{H}_B^{\dagger}\mathbf{R}\bar{\mathbf{B}}\bar{\mathbf{D}}_V\right|\frac{d\hat{\boldsymbol{Y}}}{d\psi}\right\rangle \\
&\quad + q_a\left\langle \frac{d\hat{\boldsymbol{Y}}}{d\psi}\left|\bar{\mathbf{D}}_V\bar{\mathbf{B}}^{\dagger}\mathbf{R}\mathbf{H}_B\mathbf{D}_V\right|\boldsymbol{Y}\right\rangle + q_a^2\left\langle \boldsymbol{Y}\left|\mathbf{D}_V\mathbf{H}_B^{\dagger}\mathbf{R}\mathbf{H}_B\mathbf{D}_V\right|\boldsymbol{Y}\right\rangle,
\end{aligned} \tag{5.138}$$

where

$$\mathbf{R} := \mathrm{Diag}\left(\frac{nq_a}{l}\right)\mathbf{P}^{-1}\mathrm{Diag}\left(\frac{nq_a}{l}\right). \tag{5.139}$$

Finally, we have

$$\oint a(\psi,\chi)|\mathcal{D}_\theta(\boldsymbol{Y})|^2 d\chi = \langle \boldsymbol{Y}|\mathbf{D}_V\mathbf{A}\mathbf{D}_V|\boldsymbol{Y}\rangle, \tag{5.140}$$

$$\mathbf{A} := \oint |\boldsymbol{e})a(\psi,\chi)(\boldsymbol{e}|d\chi. \tag{5.141}$$

From these transformations, we obtain the potential energy density in the vacuum$\mathcal{L}_V$ as

$$\begin{aligned}
\mathcal{L}_V = \mathcal{M}_0 &+ \left[\langle c(\psi,\chi)\rangle - \langle \boldsymbol{c}|\mathbf{P}^{-1}|\boldsymbol{c}\rangle\right]\left|\frac{dY_0}{d\psi}\right|^2 \\
&+ \left\langle \frac{d\hat{\boldsymbol{Y}}}{d\psi}\left|\bar{\mathbf{D}}_V\left(\bar{\mathbf{B}} - \bar{\mathbf{B}}^{\dagger}\mathbf{R}\bar{\mathbf{B}}\right)\bar{\mathbf{D}}_V\right|\frac{d\hat{\boldsymbol{Y}}}{d\psi}\right\rangle \\
&+ q_a\left\langle \boldsymbol{Y}\left|\mathbf{D}_V\mathbf{H}_B^{\dagger}\left(\mathbf{I} - \mathbf{R}\bar{\mathbf{B}}\right)\bar{\mathbf{D}}_V\right|\frac{d\hat{\boldsymbol{Y}}}{d\psi}\right\rangle \\
&+ q_a\left\langle \frac{d\hat{\boldsymbol{Y}}}{d\psi}\left|\bar{\mathbf{D}}_V\left(\mathbf{I} - \bar{\mathbf{B}}^{\dagger}\mathbf{R}\right)\mathbf{H}_B\mathbf{D}_V\right|\boldsymbol{Y}\right\rangle \\
&+ \left\langle \boldsymbol{Y}\left|\mathbf{D}_V\left(q_a^2\left(\bar{\mathbf{H}}_2 - \mathbf{H}_B^{\dagger}\mathbf{R}\mathbf{H}_B\right) + \mathbf{A}\right)\mathbf{D}_V\right|\boldsymbol{Y}\right\rangle,
\end{aligned} \tag{5.142}$$

where

$$\begin{aligned}
\mathcal{M}_0 = &- q_a\frac{dY_0^*}{d\psi}\left\langle \boldsymbol{c}\left|\mathbf{P}^{-1}\mathrm{Diag}\left(\frac{nq_a}{l}\right)\mathbf{H}_B\mathbf{D}_V\right|\boldsymbol{Y}\right\rangle \\
&- q_a\left\langle \boldsymbol{Y}\left|\mathbf{D}_V\mathbf{H}_B^{\dagger}\mathrm{Diag}\left(\frac{nq_a}{l}\right)\mathbf{P}^{-1}\right|\boldsymbol{c}\right\rangle\frac{dY_0}{d\psi} \\
&- \frac{dY_0^*}{d\psi}\left\langle \boldsymbol{c}\left|\mathbf{P}^{-1}\mathrm{Diag}\left(\frac{nq_a}{l}\right)\bar{\mathbf{B}}\bar{\mathbf{D}}_V\right|\frac{d\hat{\boldsymbol{Y}}}{d\psi}\right\rangle \\
&- \left\langle \frac{d\hat{\boldsymbol{Y}}}{d\psi}\left|\bar{\mathbf{D}}_V\bar{\mathbf{B}}^{\dagger}\mathrm{Diag}\left(\frac{nq_a}{l}\right)\mathbf{P}^{-1}\right|\boldsymbol{c}\right\rangle\frac{dY_0}{d\psi}.
\end{aligned} \tag{5.143}$$

The MARG2D code was extended for analyzing high$n$ external modes by expressing the energy integral in the vacuum region as Eqs. (5.87) and (5.142) with the lowest order finite hybrid element method.

5.5 Benchmark tests

We execute benchmark tests between the MARG2D code and the ERATOJ code [32], and show the validity of the result with MARG2D.

5.5.1 Stability of $n = 2$ ideal external kink mode

We first investigate the stability of $n = 2$ ideal external kink mode in the cylinder-like (the aspect ratio $A = 100$) equilibrium, whose cross section is nearly circular (the ellipticity $\kappa = 1.0$, and the triangularity $\delta = 0.0$), with the MARG2D code and the ERATOJ code. The equilibria in this paper are obtained by solving Grad-Shafranov equation numerically [48]. Figure 5.1 shows the contour of $\psi = const.$, and the profiles of the average current density parallel to the magnetic field $\boldsymbol{B}$, $j_\parallel(s)$, and the safety factor $q(s)$ ($s = \sqrt{\psi}$); in this equilibrium, the poloidal beta β_p defined in Eq. (2.33) is 0.01. The average parallel current density $j_\parallel$ is defined in Eq. (4.22); we again write

$$j_\parallel \equiv \frac{\langle \boldsymbol{J}\cdot\boldsymbol{B}\rangle_f}{\langle B^2\rangle_f} = -\frac{F}{\langle B^2\rangle_f}\frac{dp}{d\psi} - \frac{1}{\mu_0}\frac{dF}{d\psi}, \tag{5.144}$$

where F is the toroidal field function, μ_0 is the magnetic permeability in vacuum, $\langle X\rangle_f$ is the flux surface average defined in Eq. (2.18). The safety factor at the magnetic axis q_0 and that at the plasma surface q_a are 1.32 and 2.89, and $j_\parallel|_a/\langle j_\parallel\rangle = 0.21$, where $j_\parallel|_a = j_\parallel(s = 1)$, $\langle j_\parallel\rangle$ is the average current density (the ratio of total toroidal current to the poloidal cross-sectional area of the plasma), and a is the plasma minor radius.

The mesh numbers in the MARG2D code and the ERATOJ code are determined by confirming the convergence of the eigenvalues. Since the ERATOJ code is based on the two-dimensional finite element method with the lowest order elements, it needs at least four times mesh numbers in the poloidal direction as many as the MARG2D code, based on the Fourier harmonics in the poloidal direction [31]. For computing the eigenvalue of the $n = 2$ external kink mode, we set for the MARG2D code the radial mesh number in the plasma region $NPSI_{M2D} = 1200$, that in the vacuum region $NV_{M2D} = 120$, and select the poloidal Fourier harmonics $-32 \le m \le 32$; which is to say that the Fourier harmonics number $M_{M2D} = 32$ around the middle harmonic $M_{peak} = 0$. For the ERATOJ code, we used the radial mesh number in the plasma $NPSI_{ERT} = 800$, that in the vacuum $NV_{ERT} = 80$, and the mesh number in the poloidal direction $NCHI_{ERT} = 256$ are used; these are enough to converge the eigenvalues.

In the cylinder equilibrium case, the energy integral of the perturbed magnetic field in the vacuum region can be written as

$$W_V = \pi\left[r^2F^2\Lambda\right]_a\xi_a^2, \tag{5.145}$$

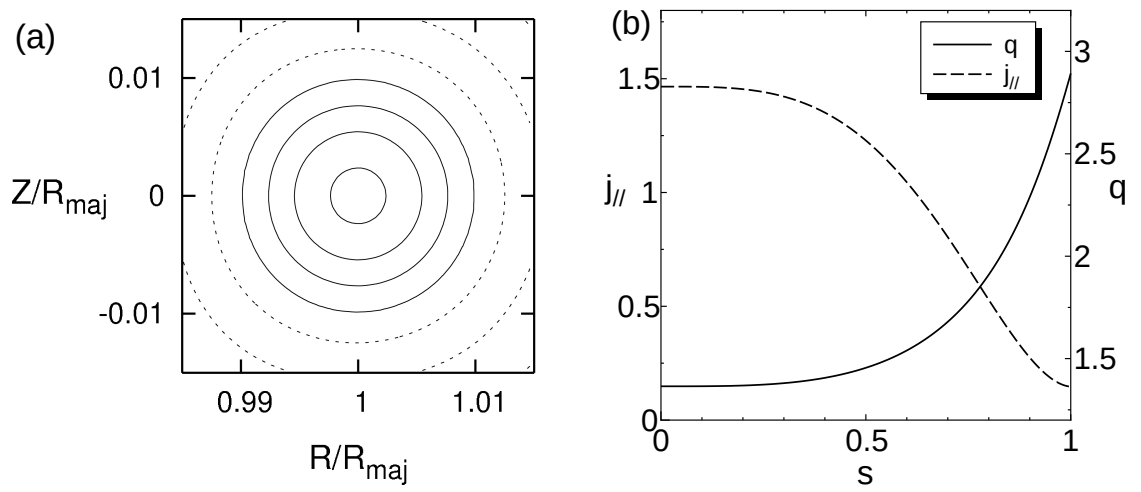

Figure 5.1: Equilibrium whose parameters are$A = 100$, $\kappa = 1.0$, $\delta = 0.0$, and $\beta_p = 0.001$. (a) Contours of ψ (magnetic surfaces). Solid lines are for $\psi \leq 0$ (plasma region), and broken lines are for $\psi > 0$ (vacuum region). The outermost solid line shows the plasma surface. (b) Profiles of the safety factor q (solid line) and the parallel current density $j_\parallel$ (dashed line), where $s = \sqrt{\psi}$. The values of the safety factor at the magnetic axis q_0 and that at the plasma surface q_a are 1.32 and 2.89, and $j_\parallel|_a/\langle j_\parallel\rangle_a$, where $j_\parallel|_a = j_\parallel(s = 1)$ and $\langle j_\parallel\rangle_a$ is the average current density, is 0.21, respectively.

where

$$\Lambda = -\frac{\mathcal{K}_a}{ka\mathcal{K}_a'}\left[\frac{1-(\mathcal{K}_b'\mathcal{I}_a)/(\mathcal{I}_b'\mathcal{K}_a)}{1-(\mathcal{K}_b'\mathcal{I}_a')/(\mathcal{I}_b'\mathcal{K}_a')}\right], \tag{5.146}$$

$\mathcal{I}_z = \mathcal{I}_m(kz)$ ($z = a$ or b), $\mathcal{K}_z = \mathcal{K}_m(kz)$, $\mathcal{I}_m$, $\mathcal{K}_m$ are m-th order modified Bessel functions, m corresponds to the poloidal mode number, k is the toroidal wave number, and b is the minor radius of the conducting wall, respectively [42]. Since the equilibrium shown in Fig. 5.1 is like a cylinder ($A = 100$), we can use Eq. (5.145) to estimate W_V, and compare the results obtained by three methods; one is the method with the MARG2D code that W_V is calculated by Eq. (5.87) (MARG2D-V.P.), second is that with the MARG2D code that W_V is obtained by Eq. (5.145) (MARG2D-Bessel), and the last is that with the ERATOJ code.

We investigate the stability of $n = 2$ ideal external kink modes in the $(b/a, \lambda_0)$ plane, where λ_0 is the minimum eigenvalue calculated by the MARG2D code (λ_{0-M2D}) or ERATOJ code (λ_{0-ERT}). Figure 5.2 shows the dependence of λ_0 on b/a in the equilibrium shown in Fig. 5.1. The solid line denotes λ_{0-M2D} obtained by MARG2D-V.P., the dashed line shows λ_{0-M2D} computed by MARG2D-Bessel, and the dotted line is for λ_{0-ERT}, respectively. Ideal external modes are marginally stable when λ_0 equals to zero. From this figure, the results computed by these three methods are almost same as each other, and these results represent that b/a

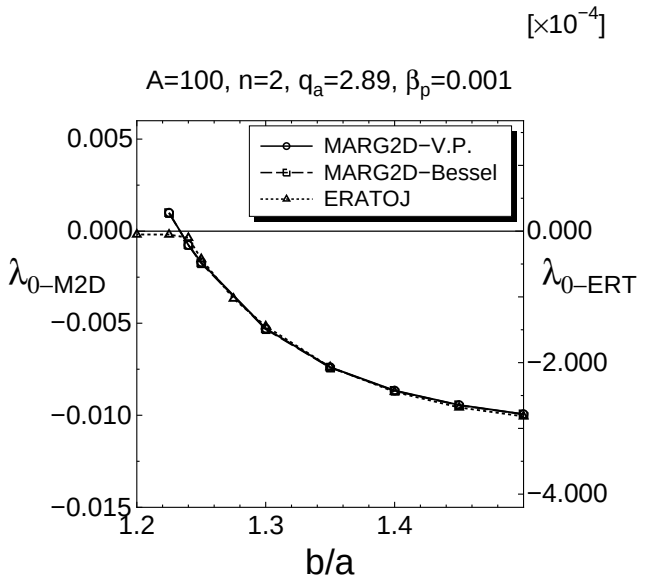

Figure 5.2: Dependence of the minimum eigenvalues λ_0 on b/a in the equilibrium shown in Fig. 5.1; the value of n is 2. The label λ_{0-M2D} denotes the minimum eigenvalue obtained by the MARG2D code, and λ_{0-ERT} is that calculated by ERATOJ (dotted line), respectively. The method for obtaining the energy integral in the vacuum region is changed in the MARG2D code; one is calculated by Eq. (5.87) (MARG2D-V.P., solid line), the other is computed by Eq. (5.145) (MARG2D-Bessel, dashed line). Each result obtained by these three methods are almost same as each other, and the b/a value when ideal external modes are marginally stable is 1.23.

when ideal external modes are marginally stable is $(b/a)_{mgl} = 1.23$.

We also compare the eigenfunctions belonging to λ_0 when $b/a = 1.24$ which is close to $(b/a)_{mgl}$; all minimum eigenvalues are negative. As shown in Fig. 5.3, since $n = 2$ and $q_a = 2.89$, it is well-known that the surface modes with the dominant harmonic $(m, n) = (6, 2)$ appears as ideal external kink modes [31, 65], and each poloidal Fourier harmonic of these eigenfunctions obtained by (a) MARG2D-V.P. ($\lambda_{0-M2D} = -7.51 \times 10^{-4}$), (b) MARG2D-Bessel ($\lambda_{0-M2D} = -7.52 \times 10^{-4}$), and (c) ERATOJ ($\lambda_{0-ERT} = -1.02 \times 10^{-5}$) is nearly identical to each other.

5.5.2 Stability of $n = 5$ ideal external modes

We next investigate the stability of $n = 5$ external modes in the (β_p, λ_0) plane. The common parameters of the analyzed equilibria are $A = 3.3$, $\kappa = 1.8$, and $\delta = 0.45$. The functional

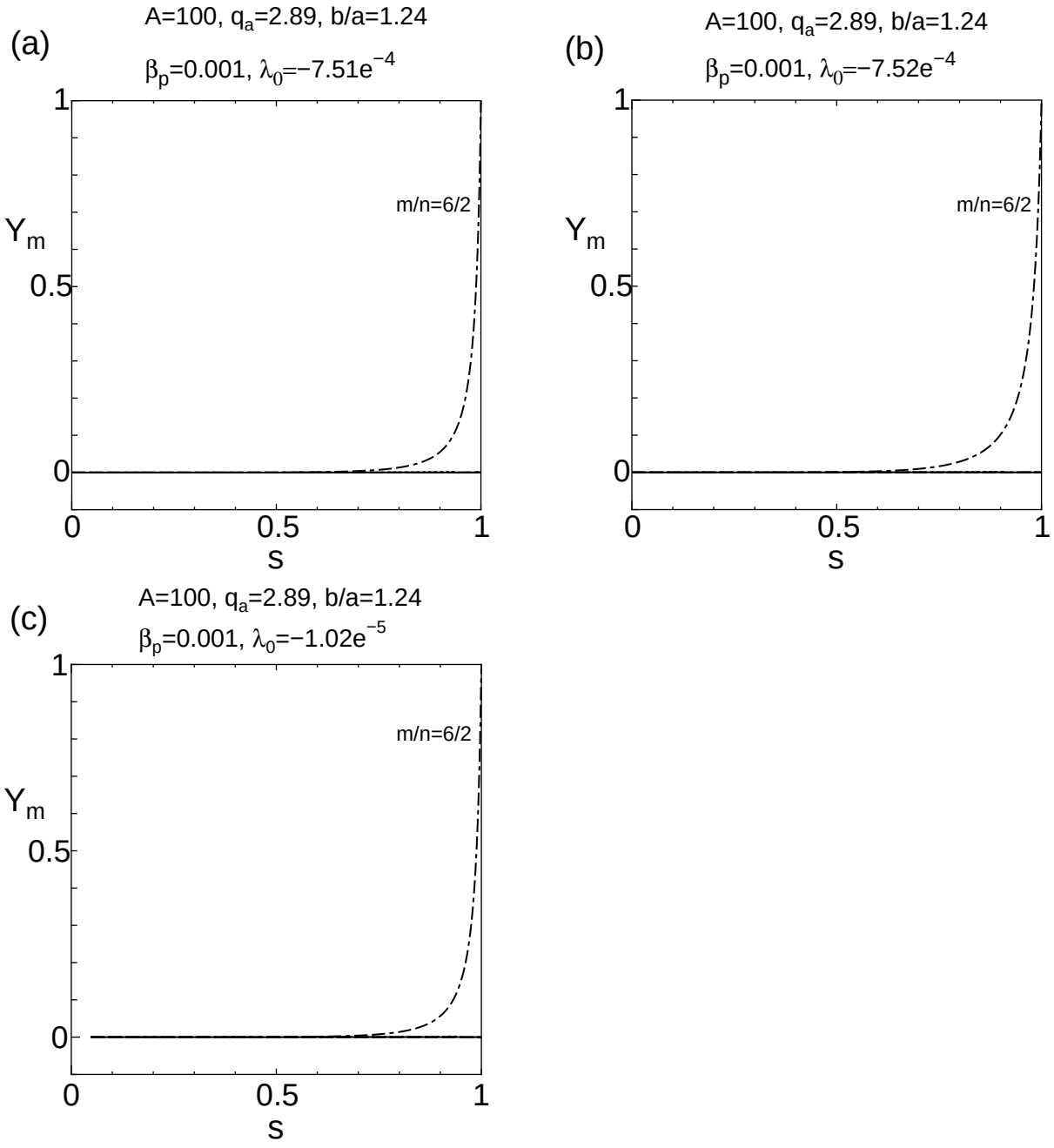

Figure 5.3: Poloidal Fourier harmonics of the eigenfunctions belonging toλ_0 when $n = 2$, $q_a = 2.89, \beta_p = 0.001$, and $b/a = 1.24$. These are obtained by (a) MARG2D-V.P. ($\lambda_{0-M2D} = -7.51 \times 10^{-4}$), (b) MARG2D-Bessel ($\lambda_{0-M2D} = -7.52 \times 10^{-4}$), and (c) ERATOJ ($\lambda_{0-ERT} = -1.02 \times 10^{-5}$). The harmonics Y_m obtained by three methods are nearly identical to each other, and these show typical surface modes with the dominant harmonic$(m, n) = (6, 2)$.

β_p	CF_1	CF_2	α_F	ν_F	σ_F
1.4	5.0	1.58	0.260	0.0	10.0
1.5	5.0	1.56	0.250	0.0	10.0
1.6	5.0	1.55	0.250	0.0	10.0
1.7	5.0	1.45	0.242	0.0	10.0
1.8	5.0	1.40	0.229	0.0	10.0
2.0	5.0	1.20	0.200	0.0	5.0
2.2	5.0	1.20	0.210	0.0	5.0

Table 5.1: Parameters in Eq. (5.148) for each β_p equilibrium for investigating $n = 5$ stability.

forms of $p(\psi)$ and $j(\psi)$ are given as

$$\frac{dp}{d\psi} = -\beta_{p0}\left(\left(1-\psi^5\right)^{1.2}\right), \tag{5.147}$$

$$\frac{dF}{d\psi} = -\left(1-\psi^{CF_1}\right)^{CF_2}\cdot\exp\left(-4\psi\right) + \alpha_F \exp\left(-\frac{(\psi-\nu_F)^2}{2\sigma_F^2}\right), \tag{5.148}$$

where β_{p0} is the current poloidal beta at the magnetic axis defined as

$$\beta_{p0} \equiv \frac{2\mu_0 p_0}{B_{pa}^2}, \tag{5.149}$$

p_0 is the plasma pressure at the magnetic axis and and B_{pa} is the average poloidal magnetic field at the plasma edge defined in Eq. (2.34). Since the stability of current driven external modes mostly depends on the q profile near the plasma surface and $j_\parallel|_a$, the q profile near the surface and $j_\parallel|_a/\langle j_\parallel\rangle$ value are nearly fixed as $j_\parallel|_a/\langle j_\parallel\rangle = 0.18$ by modifying the parameters of Eq. (5.148) as shown in Tab. 5.1 when we change the β_p value; one of them whose $\beta_p = 1.5$ is shown in Fig. 5.4. Figure 5.4(a) shows the contour of $\psi = const.$, and the profiles of $j_\parallel(s)$ and $q(s)$, and those of $p(s)$ and the pressure gradient to ψ, $dp/d\psi(s)$, are shown in Figs.5.4(b) and 4(c), respectively. The values of q_0 and q_a are 1.52 and 4.35.

To converge the eigenvalues, we used the parameters for MARG2D (afterward, MARG2D means MARG2D-V.P.) as $NPSI_{M2D} = 1200$, $NV_{M2D} = 120$, and select the poloidal Fourier harmonics $-44 \le m \le 84$; in fact, $M_{M2D} = 64$ around $M_{peak} = 20$. We also set the parameters for ERATOJ as $NPSI_{ERT} = 1200$, $NV_{ERT} = 120$, and $NCHI_{ERT} = 384$; in this case, we use the eikonal transformation in the ERATOJ code [66].

Figure 5.5 shows the dependence of λ_0 on β_p when $n = 5$, $q_a = 4.35$ and $b/a = 1.25$. In this figure, since the dashed line obtained with ERATOJ closes in on the $\lambda_{0-ERT} = 0$ line asymptotically, we are hard to determine the β_p limit, $\beta_{p,cr}$, for $n = 5$ MHD modes; $\beta_{p,cr}$ is the β_p value that the analyzed MHD modes are marginally stable. In contrast, the solid line

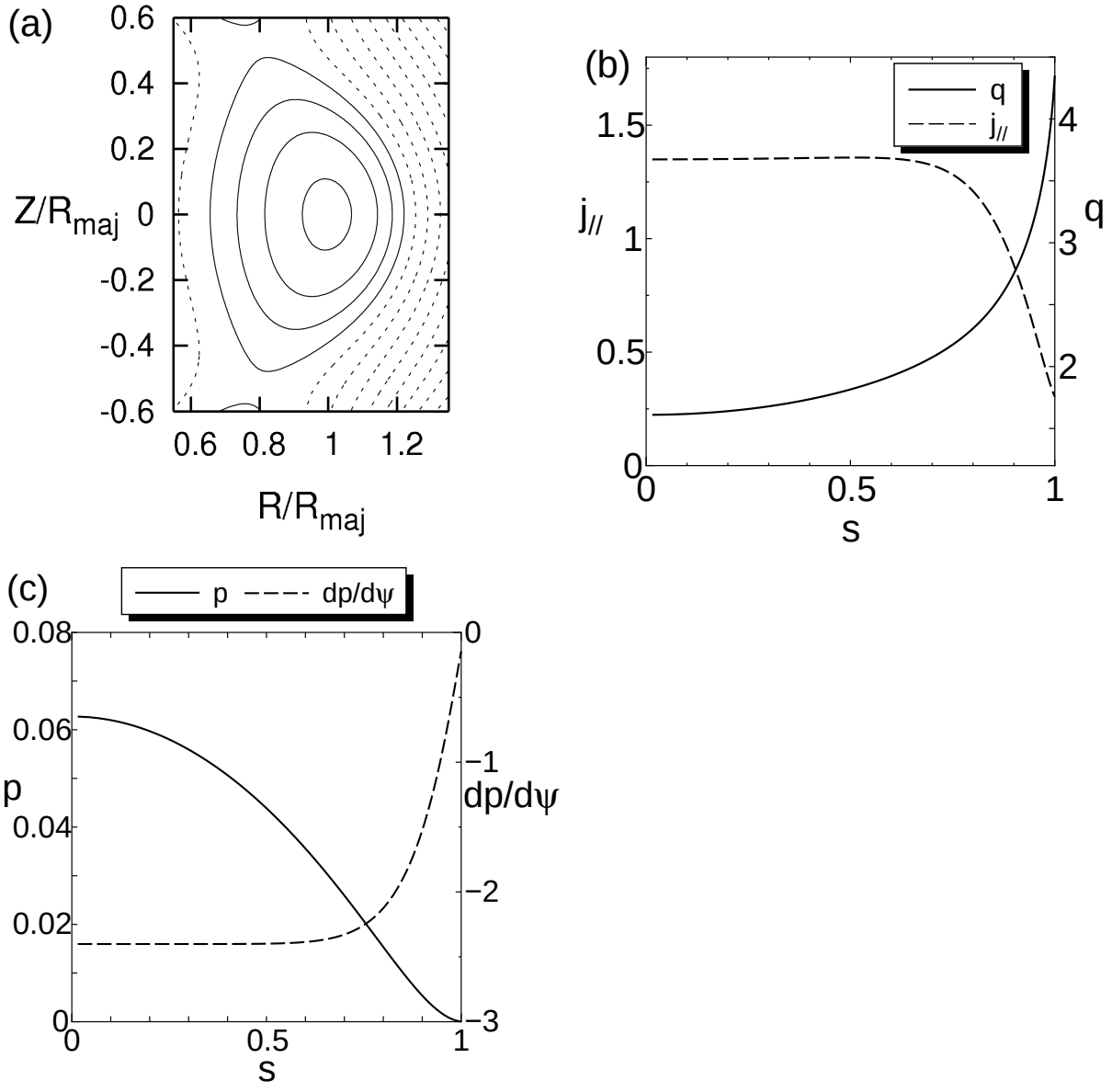

Figure 5.4: Equilibrium whose parameters are $A = 3.3$, $\kappa = 1.8$, $\delta = 0.45$, and $\beta_p = 1.5$. (a) Contours of ψ (magnetic surfaces). The outermost solid line shows the plasma surface. (b) Profiles of q (solid line) and $j_\parallel$ (dashed line). The values of q_0 and q_a are 1.52 and 4.35, and $j_\parallel|_a/\langle j_\parallel\rangle_a = 0.18$, respectively. (c) Profiles of the pressure p (solid line) and the pressure gradient $dp/d\psi$ (dashed line).

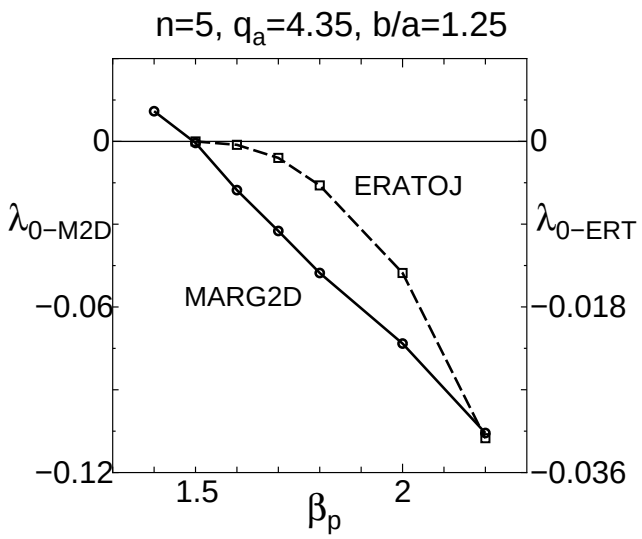

Figure 5.5: Dependence of λ_0 on β_p when $n = 5$, $q_a = 4.35$ and $b/a = 1.25$; one of the equilibria is shown in Fig. 5.4. Though the dotted line obtained with ERATOJ closes toward the $\lambda_{0-ERT} = 0$ line asymptotically, the solid line computed with MARG2D crosses the $\lambda_{0-M2D} = 0$ line, and reveals the β_p limit $\beta_{p,cr}$ for $n = 5$ modes as 1.5.

obtained with MARG2D can cross the $\lambda_{0-M2D} = 0$ line, and clarifies $\beta_{p,cr}$ for $n = 5$ modes as 1.5.

The poloidal Fourier harmonics of the eigenfunction belonging to λ_0 are shown in Figs.5.6 ($\beta_p = 1.5$) and 5.8 ($\beta_p = 2.2$); to obtain the eigenfunction, we set $NCHI_{ERT} = 1024$ to converge the eigenvalue without the eikonal transformation for the ERATOJ code. When $\beta_p = 1.5$ shown in Fig. 5.6, the Fourier harmonics structures obtained by (a) the MARG2D code ($\lambda_{0-M2D} = -5.55 \times 10^{-4}$) and (b) the ERATOJ code ($\lambda_{0-ERT} = -8.83 \times 10^{-6}$) are similar to each other, and the dominant harmonic is $(m, n) = (22, 5)$ peaking at the plasma surface.

Figure 5.7 shows the contours of ψ and the constant-height surface of $Y_0(r, \theta)$ when $\beta_p = 1.5$, where $Y_0(r, \theta)$ is defined as

$$Y_0(r, \theta) = \mathrm{Re}\left[\sum_{m=M_{min}}^{M_{max}} (\boldsymbol{Y}_0(r))_m \exp(\mathrm{i}m\theta)\right], \tag{5.150}$$

$\boldsymbol{Y}_0$ is the eigenfunction belonging to λ_{0-M2D}, M_{min} and M_{max} are the minimum and the maximum poloidal mode numbers; in this $n = 5$ case, $M_{min} = -44$ and $M_{max} = 84$. The constant-height surface in Fig. 5.7(a) is drawn in $-0.6 \le Y_0 \le 0.6$ range, where $Y_0(r, \theta)$ is normalized as $\max(Y_0) = 1$ and the region where $|Y_0| \ge 0.6$ is blacked out. Since the $(m, n) = (22, 5)$ component peaking at the plasma surface is the dominant component of $\boldsymbol{Y}_0$ as shown in Fig. 5.6(a), the mode structure localized at the plasma surface can be shown. Figure 5.7(b) shows

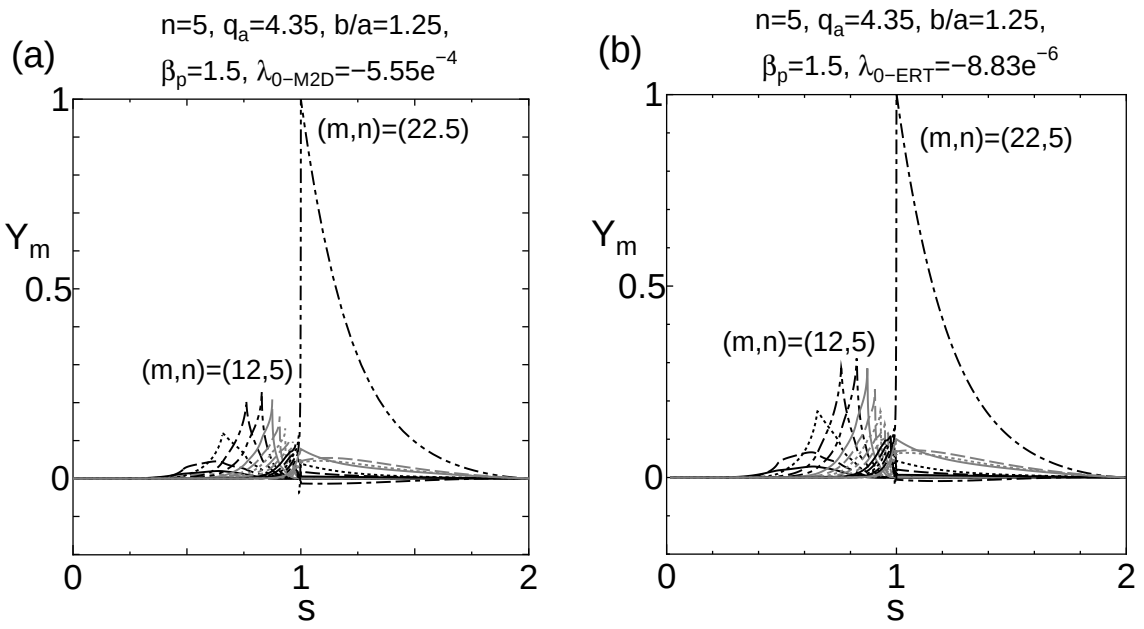

Figure 5.6: Poloidal Fourier harmonics of the eigenfunctions belonging toλ_0 when $n = 5$, $q_a = 4.35, \beta_p = 1.5$ and $b/a = 1.25$. These are obtained with (a) MARG2D ($\lambda_{0-M2D} = -5.55 \times 10^{-4}$) and (b) ERATOJ ($\lambda_{0-ERT} = -8.83 \times 10^{-6}$). The harmonics Y_m obtained by these methods are similar to each other; the (22,5) harmonic peaking at the plasma surface is dominant in these eigenfunctions.

the constant-height surface in the range from -0.3 to 0.3 and contours ofψ; the ballooning mode like structure is emphasized in the outboard bad curvature region. From Figs. 5.6 and 5.7, the most unstable eigenfunction is revealed that consists mainly of a peeling structure with a secondary ballooning structure.

On the other hand, when$\beta_p = 2.2$ in Fig. 5.8, the Fourier harmonics obtained with (a) MARG2D ($\lambda_{0-M2D} = -0.106$) are far from those obtained with (b) ERATOJ ($\lambda_{0-ERT} = -4.13 \times 10^{-2}$). The Fourier harmonics structure shown in Fig. 5.8(a) is more similar to that shown in Fig. 5.6(a); these are obtained with MARG2D. However, the harmonics structures shown in Figs.5.6(b) and 5.8(b), which are computed with ERATOJ, are different from each other. In Fig. 5.8(b), the $5 \leq m \leq 21$ Fourier harmonics in the plasma ($s \leq 1.0$) have finite amplitudes and construct the envelope peaking at$s \simeq 0.82$; this is an edge ballooning mode and is prominent part of the eigenfunction.

From figures obtained with ERATOJ, we understand that the mode structure of the eigenfunction belonging toλ_0 changes from the 'edge ballooning dominant' structure to the 'peeling dominant' structure asβ_p decreases. However, the mode structure shown in Fig. 5.8(a) is different from that in Fig. 5.8(b), but is similar to that in Fig. 5.6(a). The reason is thought

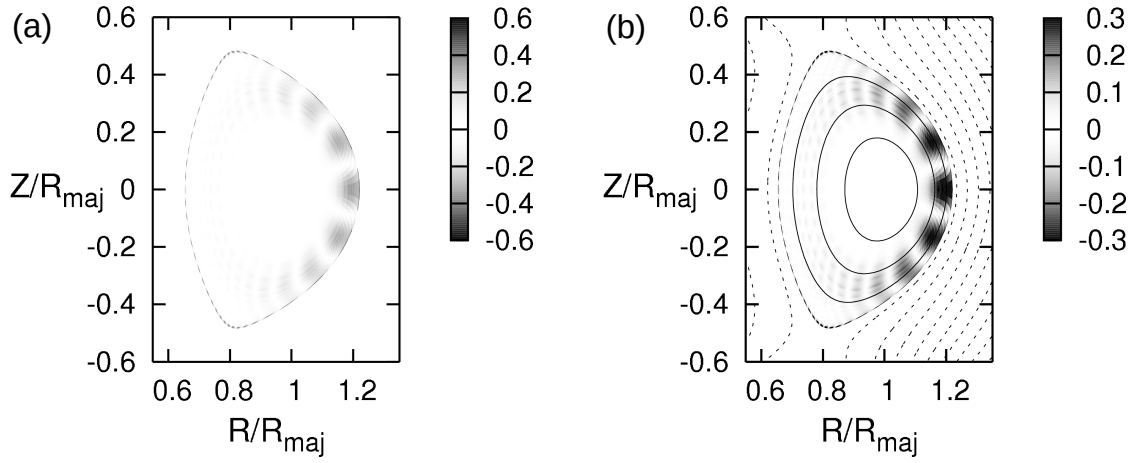

Figure 5.7: Constant-height surfaces of $Y_0(r,\theta)$ when $n = 5$, $q_a = 4.35$, $\beta_p = 1.5$, and $b/a = 1.25$; $Y_0(r,\theta)$ is defined as Eq. (5.150) and normalized $\max(Y_0(r,\theta))$ as unity. (a) Range of the constant-height surface is set as $-0.6 \le Y_0 \le 0.6$; regions where $|Y_0(r,\theta)| > 0.6$ are blacked out. Since the peeling component peaking at the plasma surface is prominent as shown in Fig. 5.6(a), the mode structure localized at the plasma surface appears. (b) Range of the constant-height surface is set as $-0.3 \le Y_0 \le 0.3$. Contours of ψ are also shown; solid lines show $\psi = -0.8$ (innermost contour), -0.5, and -0.2 contours, and broken lines are for $\psi \ge 0.2$ contours. A ballooning mode like structure in the outboard bad curvature region is emphasized.

as that the mode structure of the eigenfunction belonging to non-zero λ_0 is tied to that of the marginally stable ($\lambda_0 = 0$) eigenfunction, because the MARG2D code solves the eigenvalue problem associated with the Newcomb equation

$$\mathcal{N}\boldsymbol{Y} = -\lambda \mathrm{Diag}(\rho)\boldsymbol{Y}, \tag{5.151}$$

which is already derived in Chapter 3 as Eqs. (3.123) and (3.124), and this eigenvalue problem is physically correct when the eigenvalue $\lambda = 0$.

5.5.3 Stability of high-n external modes

A high-β equilibrium often has a steep pressure gradient, called a pedestal structure, and a large bootstrap current [47, 49, 50] near the plasma surface; this is called as an 'ELMy-H operation'. In such an equilibrium, edge localized modes (ELMs) tend to become unstable; ELMs are constructed with a high-n external kink mode, called a peeling mode, a high-n ballooning mode localized near the plasma surface, and both of them. We investigate the stabilities of high-n external modes in the equilibria with a pedestal structure in this subsection.

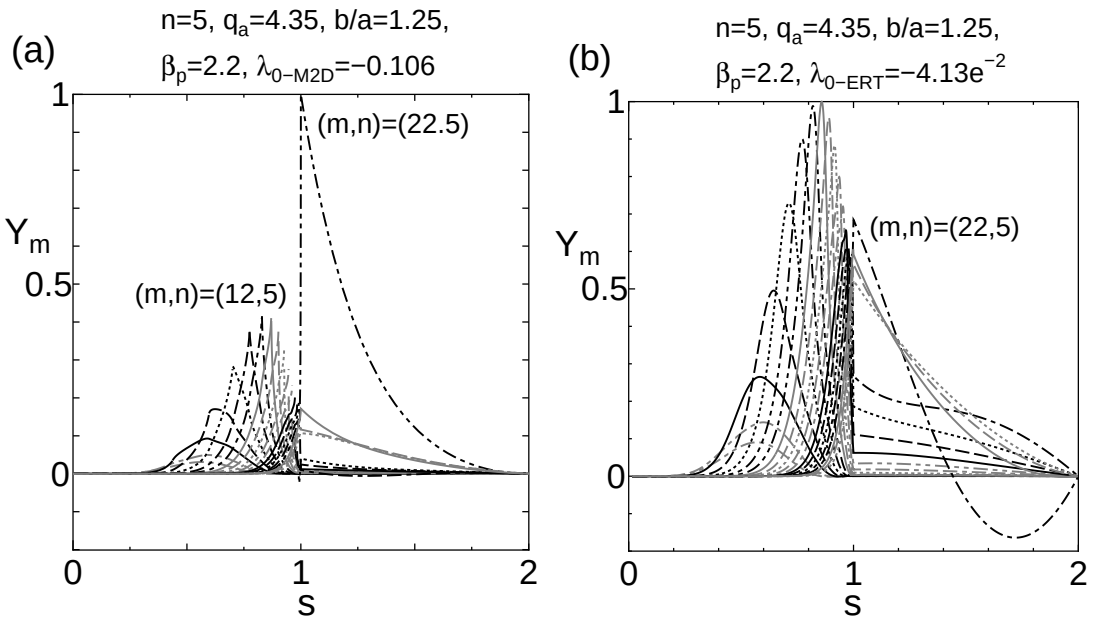

Figure 5.8: Poloidal Fourier harmonics of the eigenfunctions belonging toλ_0 when $n = 5$, $q_a = 4.35, \beta_p = 2.2$ and $b/a = 1.25$. These are obtained with (a) MARG2D ($\lambda_{0-M2D} = -0.106$) and (b) ERATOJ ($\lambda_{0-ERT} = -4.13 \times 10^{-2}$). These are apparently different from each other. In Fig. 5.8(b), an edge ballooning mode whose envelope peaks at$s \simeq 0.82$ is dominant, but in Fig. 5.8(a), the (22,5) harmonic peaking at the plasma surface is dominant like in Fig. 5.6(a) ($\beta_p = 1.5$). The reason is that since the MARG2D code solves the Newcomb equation Eq. (5.151), the mode structure obtained by the MARG2D code is tied to the mode structure of the marginally stable eigenfunction (Fig. 5.6(a)).

The common parameters of the equilibria are$A = 3.3$, $\kappa = 1.8$, and $\delta = 0.45$. Since A, κ, and δ is same as those of the equilibrium shown in Fig. 5.4, the contour of$\psi = const.$ is almost same as that shown in Fig. 5.4. The functional form of$j(\psi)$ is given as Eq. (5.148), and that of $p(\psi)$ is

$$\frac{dp}{d\psi} = -\beta_{p0}\left(1 + 15 \cdot \exp\left(-\frac{(\psi - 0.91)^2}{2 \cdot (0.03)^2}\right)\right). \tag{5.152}$$

As in the previous subsection, we modify the parameters of Eq. (5.148) as shown in Tab. 5.2 to fix the q profile near the surface and $j_\parallel|_a/\langle j_\parallel\rangle$ value as 0.135 when theβ_p value is changed. Figure 5.9 shows the $j_\parallel$, q, p, and $dp/d\psi$ profiles when$\beta_p = 1.2$. The values of q_0 and q_a are 1.7 and 4.27, and the $j_\parallel|_a$ value is finite to make a peeling mode unstable.

In these equilibria, we investigate the stability of the$n = 40$ external modes; the parameters in MARG2D are$NPSI_{M2D} = 2800$, $NV_{M2D} = 280$, $M_{M2D} = 90$, and $M_{peak} = 130$. Figure 5.10 is the poloidal Fourier harmonics of the eigenfunction belonging toλ_{0-M2D} when $n = 40$, $q_a = 4.27, \beta_p = 1.4$, and $b/a = 1.2$; the eigenvalue is nearly equal to zero ($\simeq -7.77 \times 10^{-3}$).

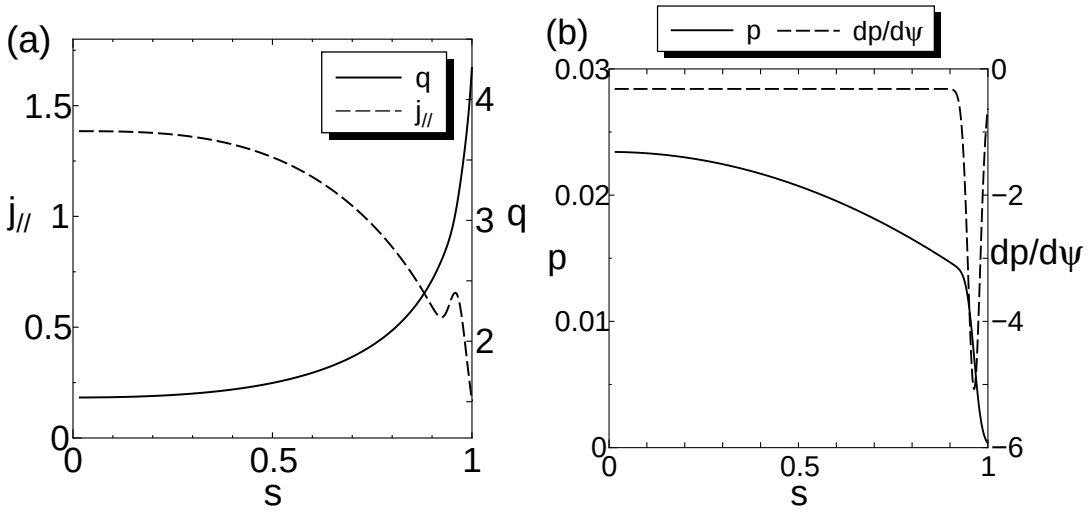

Figure 5.9: Equilibrium whose parameters are $A = 3.3$, $\kappa = 1.8$, $\delta = 0.45$, and $\beta_p = 1.2$. (a) Profiles of q (solid line) and $j_{\|}$ (dashed line). The values of q_0 and q_a are 1.7 and 4.27, and $j_{\|}|_a / \langle j \rangle_a = 0.135$, respectively. (b) Profiles of p (solid line) and $dp/d\psi$ (dashed line).

β_p	CF_1	CF_2	α_F	ν_F	σ_F
0.1	1.12	0.7	3.06×10^{-2}	0.999	1.0
0.2	1.15	0.7	3.15×10^{-2}	0.0	20.0
0.3	1.17	0.7	3.25×10^{-2}	0.0	20.0
0.4	1.20	0.7	3.30×10^{-2}	0.0	20.0
0.5	1.24	0.7	7.00×10^{-2}	0.926	0.041
0.6	1.30	0.7	0.100	0.916	0.041
0.8	1.35	0.7	0.116	0.913	0.041
1.0	1.44	0.7	0.122	0.913	0.041
1.2	1.50	0.7	0.216	0.911	0.036
1.4	1.57	0.7	0.214	0.911	0.036
1.6	1.62	0.7	0.303	0.909	0.035
2.0	2.06	0.7	0.330	0.909	0.034

Table 5.2: Parameters in Eq. (5.148) for each β_p equilibrium that we investigate high-n stability.

n	M_{M2D}	M_{peak}
1	64	0
5	64	20
10	64	40
20	72	60
40	90	130

Table 5.3: Parameters in the MARG2D code for checking a convergence property.

As shown in Fig. 5.10(a) (the length used in the transverse axis is s), the mode structure of this eigenfunction is localized near the plasma surface. To analyze such a high n localized mode, we apply nq as the length of the transverse axis in Fig. 5.10(b); this is because nq is more suitable to pick the discrete Fourier harmonics up in detail than s. In these figures, the Fourier harmonic whose poloidal mode number is 171, that is the minimum but larger than $nq_a(= 170.8)$ integer, is dominant; this is a peeling mode. Moreover, an edge ballooning mode constructing the envelope whose maxima is $nq \simeq 150$ appears. The constant-height surfaces shown in Fig. 5.11 also indicate such an edge localized structure comprised of a peeling mode and an edge ballooning mode.

To check a convergence property of the MARG2D code, we investigate a convergence study for the same equilibrium shown in Fig. 5.9 with different values of n (=1, 5, 10, 20, 40) when $b/a = 1.1$; the poloidal mode numbers in calculations are set as shown in Tab. 5.3, total radial mesh number $NPSI_{M2D} + NV_{M2D}$ changes from 880 to 3960, and the ratio of $NPSI_{M2D}$ to NV_{M2D} is 10 : 1 in each calculation. Figure 5.12 shows the result of this study, where the variable $d\lambda_{0-M2D}$ is the difference of λ_{0-M2D} from that computed with the mesh number $NPSI = 800, NV = 80$. A well quadratic convergence is observed for all n values.

On the basis of this convergence check, we set the parameters in the MARG2D code to investigate the stability of $n = 1, 5, 10, 15, 20, 30$, and 40 ideal modes as shown in Tab. 5.4.

Figure 5.13 shows the λ_{0-M2D} dependence on β_p for the different n (=5, 10, 15, 20, 30, 40) cases when $q_a = 4.27$ and $b/a = 1.2$; one of the equilibria is shown in Fig. 5.9. The $n = \infty$ ballooning stability is checked by solving the ballooning equation [67] and we compute $\beta_{p,cr}$ for $n = \infty$ ballooning mode is 0.22, and the $n = 1$ ideal mode is always stable under this $q_a = 4.27$ and $b/a = 1.2$ condition. In this figure, the $n = 5$ ideal mode (black solid line) becomes unstable when $\beta_p \geq 0.62$; $\beta_{p,cr}$ for $n = 5$ modes is 0.62. In the same way, $\beta_{p,cr}$ for each n are clarified as 0.45 ($n = 10$, black dashed line), 0.375 ($n = 15$, black dotted line), 0.37 ($n = 20$, gray solid lines), 0.34 ($n = 30$, gray dashed line). In the $n = 40$ case, ideal mode is unstable when $\beta_p \geq 0.32$ but are stable in the region $0.61 \leq \beta_p \leq 1.22$. The reason of

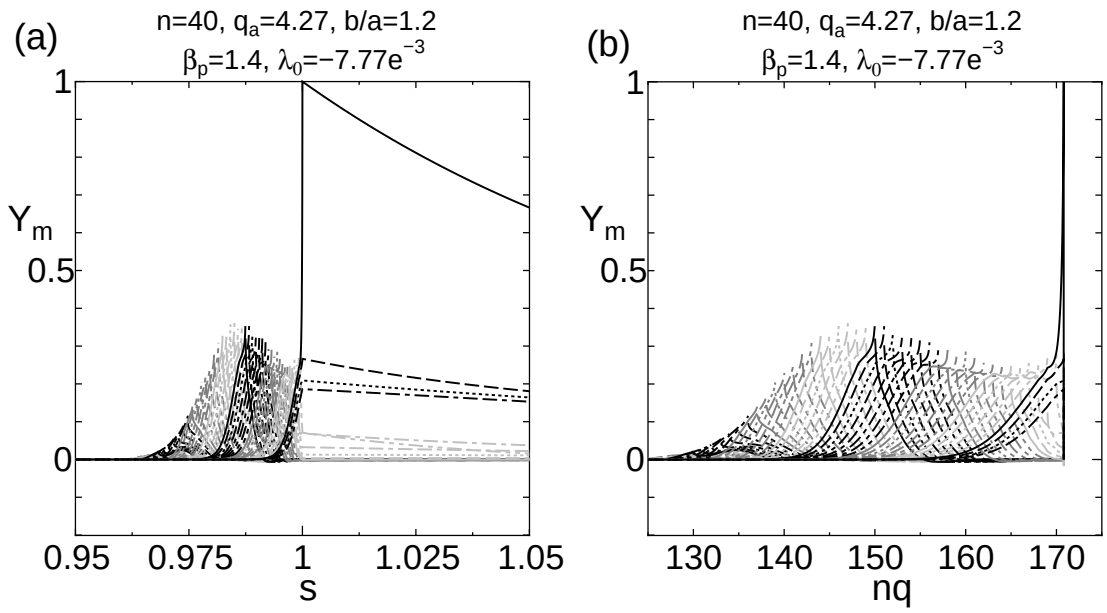

Figure 5.10: Poloidal Fourier harmonics of the eigenfunction belonging to λ_{0-M2D} ($= -7.77 \times 10^{-3}$) when $n = 40$, $q_a = 4.27$, $\beta_p = 1.4$, and $b/a = 1.2$. Since the mode structure is localized near the plasma surface as shown in Fig. 5.10(a) (the length used in the transverse axis is s), we apply nq instead of s as the transverse axis in Fig. 5.10(b). In these figures, a peeling mode whose m is 171 and an edge ballooning mode constructing the envelope whose maxima is $nq \simeq 150$ appear.

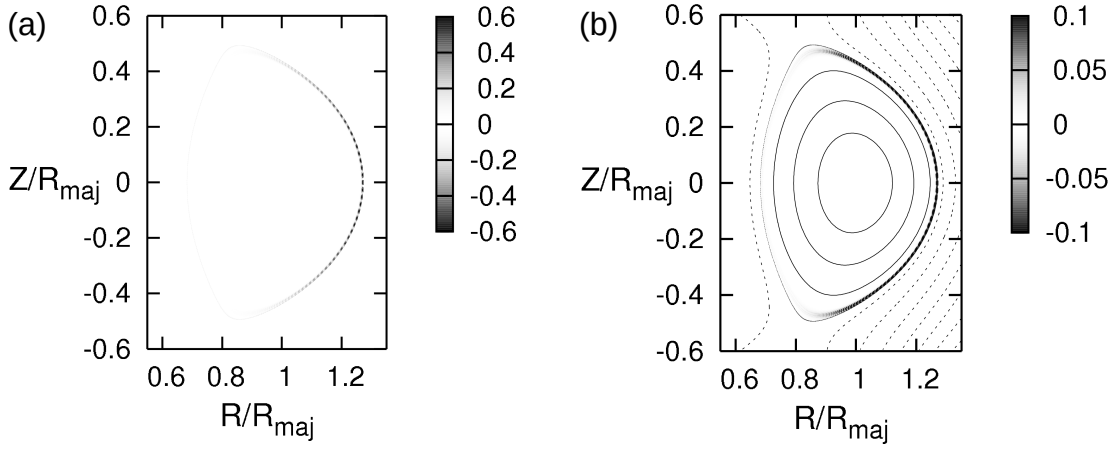

Figure 5.11: Constant-height surfaces of $Y_0(r, \theta)$ when $n = 40$, $q_a = 4.27$, $\beta_p = 1.4$, and $b/a = 1.2$. (a) Range of the constant-height surface is set as $-0.6 \leq Y_0 \leq 0.6$; regions where $|Y_0(r, \theta)| > 0.6$ are blacked out. An edge ballooning structure appears in the outboard bad curvature region. (b) Range is set as $-0.1 \leq Y_0 \leq 0.1$. Contours of ψ are also shown; solid lines show $\psi = -0.8$ (innermost contour), -0.5, and -0.2 contours, and broken lines are for $\psi \geq 0.2$ contours. A peeling component is emphasized at the plasma surface, especially at the top and bottom of the surface.

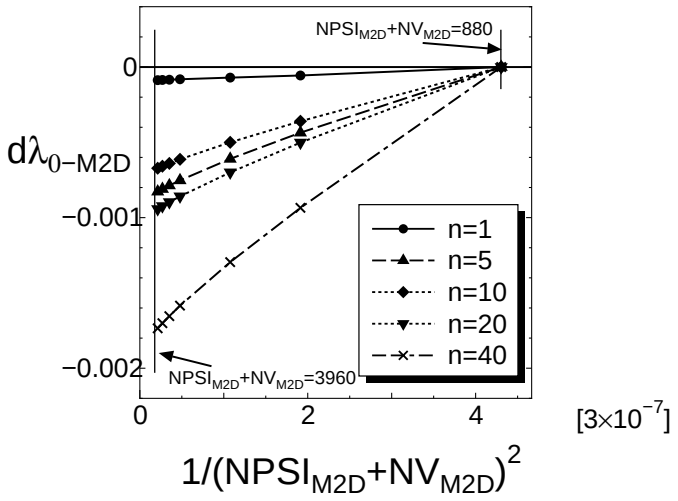

Figure 5.12: Dependence of $d\lambda_{0-M2D}$ on the reciprocal of the square of total radial mesh number ($NPSI_{M2D} + NV_{M2D}$) in the equilibrium shown in Fig. 5.9; $d\lambda_{0-M2D}$ is the difference of λ_{0-M2D} from that computed with the mesh number $NPSI_{M2D} + NV_{M2D} = 880$. The $NPSI_{M2D}+NV_{M2D}$ value changes from 880 to 3960. A well quadratic convergence is observed for all values of n (= 1, 5, 10, 20, 40).

n	$NPSI_{M2D}$	NV_{M2D}	M_{M2D}	M_{peak}
1	800	80	64	0
5	1200	120	64	20
10	1200	120	64	40
15	1600	160	64	50
20	1600	160	72	60
30	2400	240	72	100
40	2800	280	90	130

Table 5.4: Parameters in the MARG2D code for each$n$ stability analysis.

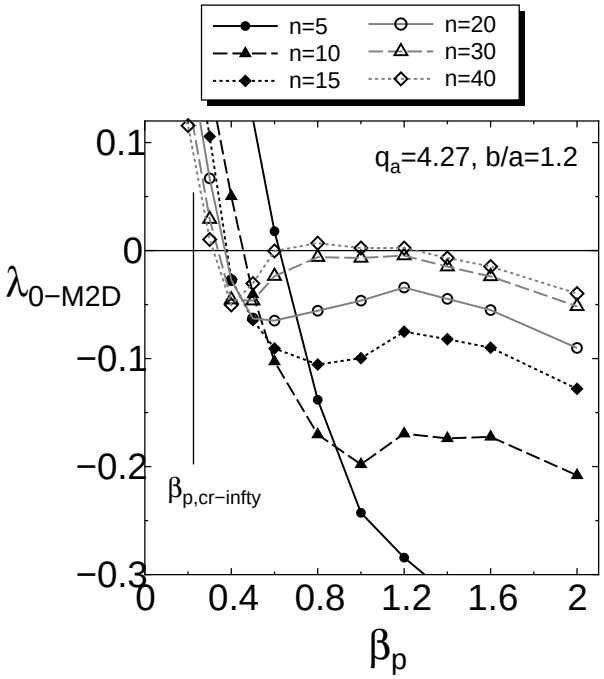

Figure 5.13: Dependence of λ_{0-M2D} on β_p for the different n values; one of the equilibria is shown in Fig. 5.9. The $n = \infty$ ballooning mode is unstable when $\beta_p \geq \beta_{p,cr-infty} = 0.22$, and the $n = 1$ mode is always stable under the $q_a = 4.27$ and $b/a = 1.2$ condition. The values of the β_p limit $\beta_{p,cr}$ for each n ideal MHD mode are clarified as 0.62 ($n = 5$, black solid line), 0.45 ($n = 10$, black dashed line), 0.375 ($n = 15$, black dotted line), 0.37 ($n = 20$, gray solid lines), and 0.34 ($n = 30$, gray dashed line). In the $n = 40$ case, ideal mode are unstable when $\beta_p \geq 0.32$ but are stable in the region $0.61 \leq \beta_p \leq 1.22$. This stabilization is made by the Shafranov shift that enforces the shape stabilizing effect.

this stabilization is that the Shafranov shift [68] makes the shape effect (an ellipticity and a triangularity) strong on the stability of the $n = 40$ edge ballooning mode. As shown in this figure, the MARG2D code can analyze the stabilities of the wide n range ideal MHD modes.

5.6 Validity of the MARG2D formulation for high-n external mode analysis

The formulation of W_V used in the MARG2D code, Eq. (5.87), needs the assumption that the conducting wall surrounds the system; in other words, the no-wall limit ($b/a \to \infty$) analysis cannot be executed. However, as can be appreciated from Eq. (5.145) in the cylinder equilibrium case, the stabilizing effect of the conducting wall decreases as n of the analyzed mode

increases. Hence the position of the conducting wall is no longer the important factor to discuss the stability of high-n external modes stability.

To confirm this fact in high-β_p toroidal equilibria with the MARG2D code, we investigate the stability of $n = 1, 10, 20$, and 40 ideal MHD modes in the equilibria used in the subsection 5.5.3 shown in Fig. 5.9. The mesh numbers are also same as used in the previous subsection.

Figure 5.14 shows the dependence of λ_{0-M2D} on β_p for the different b/a cases. In the $n = 1$ case shown in Fig. 5.14(a), ideal MHD modes are stable when $b/a = 1.2$; λ_{0-M2D} is always positive in $0.1 \leq \beta_p \leq 2.0$. However, in $b/a = 1.4$ case, external modes become unstable when $\beta_p \geq 1.81$, and the $\beta_{p,cr}$ values when $b/a = 1.6$, 1.8 and 2.0 are found as 1.30, 1.13 and 1.08, respectively. This result shows that the wall position is one of the important factors to stabilize $n = 1$ external modes.

Next, in the $n = 10$ case shown in Fig. 5.14(b), MHD modes when $b/a = 1.0$ (solid line) and 1.02 (dashed line) are stable. On the other hand, when $b/a = 1.1$ (dotted line), external modes become unstable in $0.52 \leq \beta_p$, and when $b/a = 1.2$ (dot 2-dashed line), 1.3 (dot dashed line) and 1.4 (2-dot dashed line), external modes are unstable in $0.45 \leq \beta_p$. The dot dashed line ($b/a = 1.3$) approaches the 2-dot dashed line ($b/a = 1.4$) asymptotically; this means that the conducting wall situated outside $b/a = 1.3$ has little effect on the stability of $n = 10$ external modes.

When $n = 20$ shown in Fig. 5.14(c), fixed boundary mode ($b/a = 1.0$) is still stable, but external modes when $b/a = 1.02$ becomes unstable in $0.41 \leq \beta_p \leq 0.63$. When $b/a \geq 1.1$, $n = 20$ external modes are unstable in $\beta_p \geq 0.37$, and the dot 2-dashed line ($b/a = 1.15$) approaches to the the dot dashed line ($b/a = 1.2$); the stability of $n = 20$ external modes are hardly affected by the conducting wall outside $b/a = 1.15$. In the same way, in the $n = 40$ case shown in Fig. 5.14(d), we must place the conducting wall inside $b/a = 1.07$ to influence the stability of external modes; this is a impractical position to design the experiments. From these results, we show numerically that the position of the conducting wall must be close to the plasma surface to affect the stability of high-n external modes. Since the wall position cannot be so close to the plasma surface in the design of the fusion reactor, b/a is not the important factor to be discussed in the study of high-n external modes stability, and the assumption that the conduction wall surrounds the system in Eq. (5.87) is negligible for high-n mode analysis.

5.7 Parallel computing with the Scalapack library

As already mentioned, the MARG2D code can numerically identify the stability of ideal MHD modes even when these modes are stable. With this property, we intend to realize the stability analysis in the intervals of experiments, and in future times, the real-time stability study

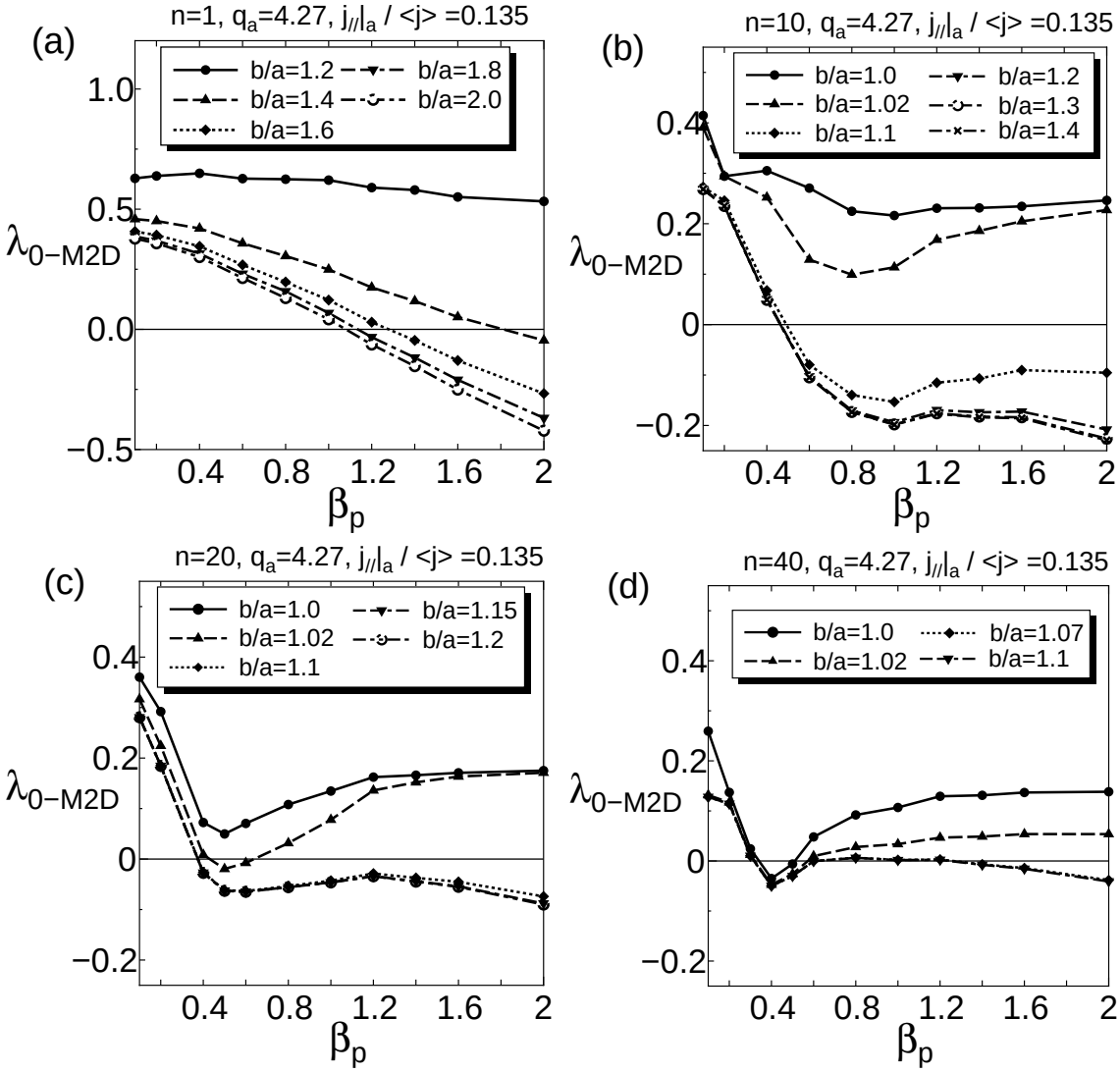

Figure 5.14: Dependence of λ_{0-M2D} on β_p for the different b/a cases. In (a) the $n = 1$ case, ideal MHD modes are stable when $b/a = 1.2$ (solid line). However, when $b/a = 1.4$ (dashed line), external modes become unstable in $\beta_p \geq 1.81$, and in $b/a = 1.6$ (dotted line), 1.8 (dot 2-dashed line), and 2.0 (dot dashed line) cases, the $\beta_{p,cr}$ values are 1.30, 1.13 and 1.08, respectively. In (b) the $n = 10$ case, ideal modes are stable when $b/a = 1.0$ (solid line) and 1.02 (dashed line) in $0.1 \leq \beta_p \leq 2.0$. However, when $b/a = 1.1$ (dotted line), external modes become unstable when $\beta_p \geq 0.52$, and when $b/a = 1.2$ (dot 2-dashed line), 1.3 (dot dashed line) and 1.4 (2-dot dashed line), the $\beta_{p,cr}$ value is 0.45; in particular, the dot dashed line becomes identical with the 2-dot dashed line asymptotically. Similarly, in (c) the $n = 20$ case, the dot 2-dashed line ($b/a = 1.15$) is almost same as the dot dashed line ($b/a = 1.2$), and the dotted line ($b/a = 1.07$) is approximately identical to the dot 2-dashed line ($b/a = 1.1$) in (d) the $n = 40$ case, respectively. These results show that the conducting wall is laid out close to the plasma surface to stabilize high-n MHD modes.

during an experiment.

To achieve these experimental analyses, the computation time need to be reduced, in particular, for realizing the real-time study, we must compute in time shorter than the characteristic time of which the MHD equilibrium is changed by the heat and particle transports; the measure of this characteristic time is about one second. We develop the MARG2D code as the parallel computing code with the message passing interface (MPI) [36] and the ScaLAPACK library [37] to shorten the computation time, and to free up the memory restriction of high-n mode stability analysis, which needs many mesh numbers for exact study as shown in Fig. 5.12.

We execute benchmark tests about the parallelization of the MARG2D code in two cases; one is the low-n (=1) case, the other is the high-n (=30) case. The parameters ($NPS\,I_{M2D}$, NV_{M2D}, M_{M2D}, M_{peak}) are (800, 80, 64, 0) for the $n = 1$ case, and (2400, 240, 72, 100) for the $n = 30$ case, respectively. The parallelization efficiency C_{eff} is defined as

$$C_{eff}(n_{PE}) := \frac{(\text{computation time when } n_{PE} = 2) \times 2}{(\text{computation time with } n_{PE}) \times n_{PE}}, \tag{5.153}$$

where n_{PE} is the number of processors; this C_{eff} is normalized with the result when $n_{PE} = 2$.

The computation system for these tests is the JAERI Origin3800 system [69], which is the scalar parallel system with 768 processors. The peak computing speed of a single processor, MIPS 500MHz processor, is 1 GFLOPs and that of this system is 768 GFLOPs. We use a part of this system for benchmark tests; the maximum processor number is 128.

The MARG2D code is composed of two processes; one is to make the matrices of $\mathcal{N}$ and $\mathcal{R}$ in Eq. (5.151), that is parallelized with MPI (Process 1), and the other is to solve Eq. (5.151) by the LU factorization and the inverse iteration method with the ScaLAPACK library (Process 2); this numerical method for linear equations is a direct method.

Figure 5.15 shows the dependence of the computation time and C_{eff} on n_{PE} in (a) the low-n case and (b) the high-n case; the equilibrium is same as shown in Fig. 5.9 and $b/a = 1.2$. The counts of the inverse iteration are set as 20 in both cases. In this figure, the black bar graph denotes the computation time for Process 1 and the gray bar graph shows that for Process 2, and C_{eff} are shown with the dashed line (Process 1), the dotted line (Process 2), and the solid line (total calculation).

In the low-n case shown in Fig. 5.15(a), the total computation time is shortened from 325.79 seconds(s) to 13.27s as n_{PE} increases from 2 to 128, and C_{eff} of total calculation is over 50% when $n_{PE} \leq 64$ and is 38.4% with $n_{PE} = 128$. This is not enough fast to achieve aforesaid experimental analyses, but C_{eff} is adequate at such a short time calculation. From these results, we deduce that the MARG2D code has potential for reducing the computation time to few seconds with the latest computation system.

In the high-n case shown in Fig. 5.15(b), the calculation time is cut down from 1279s to 36.88s, and C_{eff} of total calculation is over 60% ($n_{PE} \leq 64$) and is 54.2% ($n_{PE} = 128$). As in

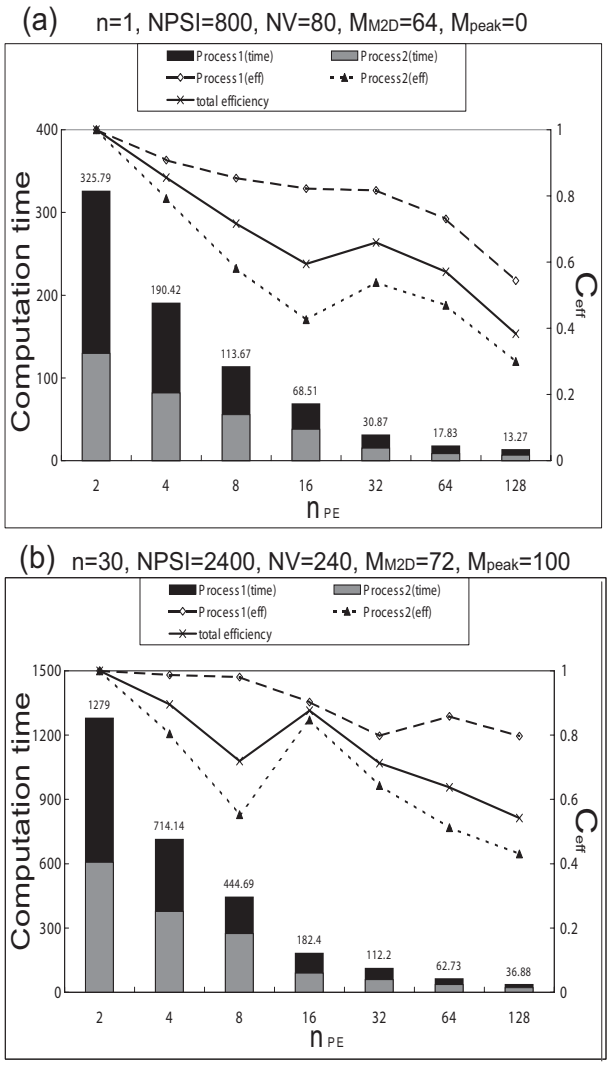

Figure 5.15: Dependence of the computation time and the parallelization efficiency C_{eff} on the number of processors n_{PE} in (a) the $n = 1$ case and (b) the $n = 30$ case; the computer system is the JAERI Origin3800 system. The numerical parameters are shown above each figure. The black bar graph denotes the computation time for Process 1 and the gray bar graph shows that for Process 2, and C_{eff} are shown with the dashed line (Process 1), the dotted line (Process 2), and the solid line (total calculation). From the results that the computation time and C_{eff} are (a) 13.27s and 38.4%, and (b) 36.88s and 54.2% when $n_{PE} = 128$, we deduce that the MARG2D code has potential for realizing the analysis in the intervals of experiments with the latest computer system.

the low-n case, the calculation time will become several seconds with the latest system, and is also enough short to the experiments interval analysis.

5.8 Summary

I have applied the approach consists of representing the plasma potential energy integral to describe the vacuum energy integral by introducing a solenoidal vector field, and have implemented this approach to a code MARG2D, which is the linear MHD stability code for a two-dimensional toroidal geometry. This approach has the advantage that the numerical accuracy in the vacuum region is kept at the same that in the plasma region, and enables us to perform the stability analysis of high-n ideal external modes. I have determined the validity of this extended MARG2D code by benchmark tests compared with the ERATOJ code, and show the beauty of the analytical model of MARG2D for identifying the stability of high$n$ external modes.

This approach restricts that a plasma and a vacuum region must be surrounded by a conducting wall. I have confirmed that the stabilizing effect of the conducting wall decreases as n of the analyzed mode increases, and the position of the conducting wall becomes meaningless for high-n external mode analysis, unlike in the low$n$ case.

The MARG2D code was developed as a parallel computing code towards the integrated simulation with the transport analyzing code, and the experimental analysis in the intervals of experiments. From results of the performance tests, this code has potential for realizing these objectives. The analysis of edge phenomena with this stability code will be reported near future.

To perform the real-time stability study during an experiment, we must reduce the calculation time more by the optimization of this code to the computation system and employing or developing the new numerical algorithm. This also will be reported near future.

Chapter 6

Summary

In this thesis, magnetohydrodynamic (MHD) external instabilities in an axisymmetric toroidal plasma have been studied on the basis of the analytical model with the property of the two-dimensional Newcomb equation.

In Chapters 2 and 3, the ideal MHD model and the two-dimensional Newcomb equation have been introduced. The theory for the linear ideal MHD stability analysis, called the Energy Principle, is efficient and intuitive method of determining plasma stability. On the basis of this theory, I introduced the two-dimensional Newcomb equation in Chapter 3; this equation describes the marginally stable state against the ideal MHD instability in a plasma. The stability of a plasma against the ideal MHD motion in a tokamak can be discriminated by solving the eigenvalue problem associated with the two-dimensional Newcomb equation. In the formulation of the eigenvalue problem, the weight functions (kinetic energy integral) and the boundary conditions at rational surfaces were chosen such that the spectra of the eigenvalue problem are comprised of only real and denumerable eigenvalues (discrete spectra). Therefore, this eigenvalue problem identifies the ideal MHD stable states, as well as the unstable states. The numerical code (MARG2D) was developed to solve the associated eigenvalue problem numerically by using the lowest order finite hybrid element method and a direct method with the LU factorization and the inverse iteration method.

In Chapter 3, the theory based on the Newcomb equation was applied to the stability analysis of low-n external MHD modes in a toroidal plasma, and the stability matrix method has been developed, where n is the toroidal mode number. With this method, the change of plasma potential energy due to the plasma displacement is expressed by a quadratic form with the boundary values of the displacement. The MARG2D-SM code was implemented this stability matrix method to identify the external mode stability.

Chapter 4 has been devoted to the application of the analysis with the stability matrix method by using the MARG2D-SM code. I have studied the spectral structure of $n = 1$ ideal external modes, especially, the spectral gaps induced by the poloidal coupling originated

from the finite aspect ratio effect in the stable region were clarified. It has been also shown that the finite poloidal beta (β_p) effect makes these gaps broaden, where β is a ratio of the plasma pressure to the magnetic pressure. Though the spectral gaps were predicted analytically, our calculations confirmed clearly these predictions.

The stability matrix method enables us to implement deeper analysis of external modes by combining with the eigenvalue problem associated with the Newcomb equation, presented in Chapter 3. I have clarified numerically and analytically the effect of stable ideal internal modes on the stability of ideal external modes when internal modes approach to the marginal stability. A stable internal mode couples with an external mode and makes an impact on the external mode stability. This coupling changes the mode structure of external modes from a surface mode to a global mode. The effect of internal modes on the external modes stability also explains the difference of stability against external modes between a normal shear tokamak and a reversed shear tokamak. This result denotes that the distinction of the safety factor profile in the plasma core region affects the external mode stability.

The property of the MARG2D and MARG2D-SM codes, the facility to identify marginal stability in short time, is effective to survey appropriate parameters of the MHD equilibrium for designing experiments and for optimizing operations. As an example, I have analyzed an effect of the aspect ratio on the stability of ideal external modes with the stability matrix method, and revealed that $n = 1$ external modes are stabilized when the aspect ratio is made small. The eigenfunction of the most unstable external mode in a high-β tokamak has a global mode structure as shown in the circular equilibrium case. Such a global mode is dangerous for tokamak operations, and the aspect ratio is supposed to be optimized for stabilizing low-n external modes.

Chapter 5 is devoted to the extension of the analytical model with the Newcomb equation for the high-n external modes stability analysis. I have applied the formulating technique, mentioned in Chapter 3, to represent the vacuum energy contribution by introducing a solenoidal vector field; this approach is called the vector potential method. This approach has the advantage that a numerical accuracy in the vacuum region is kept at the same that in the plasma region. The MARG2D code was improved with this model, and enables us to perform the stability analysis of high-n ideal external modes. Though this approach restricts that a plasma and a vacuum region must be surrounded by a conducting wall, I confirmed that the stabilizing effect of the conducting wall decreases as the n value of the analyzed mode increases, and the position of the conducting wall is negligible for high-n external mode analysis, unlike in the low-n mode analysis case.

The numerical code based on this extended model also has an advantage that a computation time for the high-n mode stability analysis becomes short, because this model is obtained by solving partly the full MHD model analytically; this is clearly shown in Chapter 3. I have developed the MARG2D as a parallel computing code to make use of this advantage,

and have shown the potential of this code enough fast for realizing numerical analyses of experimental results in the intervals of experiments.

The numerical codes MARG2D and MARG2D-SM developed and improved in this thesis realize two numerical methods for the stability analysis of external MHD modes; one is the stability matrix method, the other is solving the eigenvalue problem associated with the Newcomb equation. With these methods, the analysis of the resistive wall mode based on the quadratic form formulation, and that of the edge localized modes, especially the relation between MHD instabilities and transport phenomena, will be realized.

Appendix A

Self-adjointness of the operator $\boldsymbol{F}$

In this appendix, we show the self-adjointness of the force operator $\boldsymbol{F}$ defined in Eq. (2.42); that is

$$\int \boldsymbol{\xi} \cdot \boldsymbol{F}(\boldsymbol{\eta})\, dV = \int \boldsymbol{\eta} \cdot \boldsymbol{F}(\boldsymbol{\xi})\, dV, \tag{A.1}$$

where V is the plasma volume, $\boldsymbol{\xi}$ and $\boldsymbol{\eta}$ are two arbitrary vectors. The integrand in Eq. (A.1) can be written as

$$\boldsymbol{\eta} \cdot \boldsymbol{F}(\boldsymbol{\xi}) = \boldsymbol{\eta} \cdot \left[\frac{1}{\mu_0} \left((\nabla \times \boldsymbol{B}_0) \times \boldsymbol{Q} + (\nabla \times \boldsymbol{Q}) \times \boldsymbol{B}_0 \right) + \nabla (\boldsymbol{\xi} \cdot \nabla p_0 + \gamma p_0 \nabla \cdot \boldsymbol{\xi}) \right], \tag{A.2}$$

where $\boldsymbol{Q} = \nabla \times (\boldsymbol{\xi} \times \boldsymbol{B}_0)$. By rewriting Eq. (A.2) as

$$\begin{aligned} \boldsymbol{\eta} \cdot \boldsymbol{F}(\boldsymbol{\xi}) = {} & \nabla \cdot \left[\boldsymbol{\eta} (\boldsymbol{\xi} \cdot \nabla p_0 + \gamma p_0 \nabla \cdot \boldsymbol{\xi}) + \frac{1}{\mu_0} (\boldsymbol{\eta} \times \boldsymbol{B}_0) \times \boldsymbol{Q} \right] \\ & - \nabla \cdot \boldsymbol{\eta} (\boldsymbol{\xi} \cdot \nabla p_0 + \gamma p_0 \nabla \cdot \boldsymbol{\xi}) - \frac{1}{\mu_0} \boldsymbol{Q} \cdot \boldsymbol{R} - \frac{1}{\mu_0} (\nabla \times \boldsymbol{B}_0) \cdot (\boldsymbol{\eta} \times \boldsymbol{Q}), \end{aligned} \tag{A.3}$$

we derive

$$\int \boldsymbol{\eta} \cdot \boldsymbol{F}(\boldsymbol{\xi})\, dV = \int_{S_p} \left(\boldsymbol{\xi} \cdot \nabla p_0 + \gamma p_0 \nabla \cdot \boldsymbol{\xi} - \frac{1}{\mu_0} \boldsymbol{B}_0 \cdot \boldsymbol{Q} \right) (\boldsymbol{\eta} \cdot \boldsymbol{n}) dS - W_{pv}(\boldsymbol{\xi}, \boldsymbol{\eta}), \tag{A.4}$$

$$\begin{aligned} W_{pv}(\boldsymbol{\xi}, \boldsymbol{\eta}) = {} & \int \left[\gamma p_0 (\nabla \cdot \boldsymbol{\eta})(\nabla \cdot \boldsymbol{\xi}) + \frac{1}{\mu_0} \boldsymbol{Q} \cdot \boldsymbol{R} \right. \\ & \left. + \quad (\nabla \cdot \boldsymbol{\eta})(\boldsymbol{\xi} \cdot \nabla p_0) + \frac{1}{\mu_0} (\nabla \times \boldsymbol{B}_0) \cdot (\boldsymbol{\eta} \times \boldsymbol{Q}) \right] dV, \end{aligned} \tag{A.5}$$

where $\boldsymbol{R} = \nabla \times (\boldsymbol{\eta} \times \boldsymbol{B}_0)$, $\boldsymbol{n}$ is the unit normal to the plasma surface. Here the surface integral in Eq. (A.4) is done on the plasma surface S_p. With the boundary condition relating $\boldsymbol{\xi}$ and $\acute{\boldsymbol{A}}$ ($\acute{\boldsymbol{A}}$ is the vacuum vector potential as defined in Eq. (2.56))

$$-\gamma p_0 \nabla \cdot \boldsymbol{\xi} + \frac{1}{\mu_0} \boldsymbol{B}_0 \cdot \boldsymbol{Q} = \frac{1}{\mu_0} \acute{\boldsymbol{B}}_0 \cdot (\nabla \times \acute{\boldsymbol{A}}) + \frac{1}{2\mu_0} (\boldsymbol{\xi} \cdot \nabla)(\acute{\boldsymbol{B}}_0^2 - \boldsymbol{B}_0^2), \tag{A.6}$$

which is same as Eq. (2.57), the surface integral term in Eq. (A.4) can be transformed as

$$\begin{aligned}
&\int_{S_p}\left[\boldsymbol{\eta}(\boldsymbol{\xi}\cdot\nabla p_0+\gamma p_0\nabla\cdot\boldsymbol{\xi}-\frac{1}{\mu_0}\boldsymbol{B}_0\cdot\boldsymbol{Q})\right]\cdot\boldsymbol{n}dS\\
&=\int_{S_p}(\boldsymbol{n}\cdot\boldsymbol{\eta})(\boldsymbol{n}\cdot\boldsymbol{\xi})\left[\left[\nabla\left(p_0+\frac{B^2}{2\mu_0}\right)\right]\right]_a\cdot\boldsymbol{n}dS\\
&\quad-\frac{1}{\mu_0}\int_{S_p}(\boldsymbol{n}\cdot\boldsymbol{\eta})(\acute{\boldsymbol{B}}_0\cdot(\nabla\times\acute{\boldsymbol{A}}))\,dS,
\end{aligned}\tag{A.7}$$

where $[[X]]_a$ is the increment in any quantity X across the boundary in the direction $\boldsymbol{n}$. Here, since $[[p_0+B^2/2\mu_0]]_a=0$ as shown in Eq. (2.51), the tangential component of the jump of the derivative vanishes. By introducing one more vacuum vector potential as $\acute{\boldsymbol{R}}=\nabla\times\acute{\boldsymbol{C}}$ and the boundary condition

$$\boldsymbol{n}\times\acute{\boldsymbol{C}}=-(\boldsymbol{n}\cdot\boldsymbol{\eta})\acute{\boldsymbol{B}}_0,\tag{A.8}$$

which is same as Eq. (2.58), the last term in Eq. (A.7) is rewritten as

$$\begin{aligned}
-\frac{1}{\mu_0}\int_{S_p}(\boldsymbol{n}\cdot\boldsymbol{\eta})(\acute{\boldsymbol{B}}_0\cdot(\nabla\times\acute{\boldsymbol{A}}))\,dS&=\frac{1}{\mu_0}\int_{S_p}(\boldsymbol{n}\times\acute{\boldsymbol{C}})\cdot(\nabla\times\acute{\boldsymbol{A}})\,dS\\
&=-\frac{1}{\mu_0}\int_{S_p}\left[(\nabla\times\acute{\boldsymbol{A}})\times\acute{\boldsymbol{C}}\right]\cdot\boldsymbol{n}\,dS\\
&=\frac{1}{\mu_0}\int\nabla\cdot\left[(\nabla\times\acute{\boldsymbol{A}})\times\acute{\boldsymbol{C}}\right]dV\\
&=-\frac{1}{\mu_0}\int(\nabla\times\acute{\boldsymbol{A}})\cdot(\nabla\times\acute{\boldsymbol{C}})\,dV,
\end{aligned}\tag{A.9}$$

where we assume that a perfect conducting wall surrounds a plasma and use the boundary condition at a wall $(\boldsymbol{n}\cdot\acute{\boldsymbol{R}})_{wall}=0$. This is obviously symmetric.

Next, we show the self-adjointness of volume integral term Eq. (A.5). The first two terms in Eq. (A.5) are obviously symmetric, and the last two terms can be rewritten as

$$\begin{aligned}
dW_p(\boldsymbol{\xi},\boldsymbol{\eta})&\equiv(\nabla\cdot\boldsymbol{\eta})(\boldsymbol{\xi}\cdot\nabla p_0)+\boldsymbol{J}\cdot(\boldsymbol{\eta}\times\boldsymbol{Q})\\
&=-\boldsymbol{\eta}\cdot[\boldsymbol{J}\times\boldsymbol{Q}+\nabla(\boldsymbol{\eta}\cdot\nabla p_0)]-\nabla\cdot(\boldsymbol{\eta}(\boldsymbol{\xi}\cdot\nabla p_0)),
\end{aligned}\tag{A.10}$$

where $\boldsymbol{J}=\nabla\times\boldsymbol{B}_0/\mu_0$. The first two terms in Eq. (A.10) can be transformed as

$$\begin{aligned}
\boldsymbol{\eta}\cdot[\nabla(\boldsymbol{\xi}\cdot\nabla p_0)+\boldsymbol{J}\times\boldsymbol{Q}]&=[\boldsymbol{B}_0\times((\boldsymbol{J}\cdot\nabla)\boldsymbol{\xi}-(\boldsymbol{\xi}\cdot\nabla)\boldsymbol{J})+(\nabla p_0-\boldsymbol{J}\times\boldsymbol{B}_0)\nabla\cdot\boldsymbol{\xi}\\
&\quad+\boldsymbol{\xi}\cdot\nabla\nabla p_0-\boldsymbol{\xi}\cdot\nabla(\boldsymbol{J}\times\boldsymbol{B}_0)]\cdot\boldsymbol{\eta}\\
&=-[\boldsymbol{B}_0\times(\nabla\times(\boldsymbol{J}\times\boldsymbol{\xi}))-\nabla p_0\nabla\cdot\boldsymbol{\xi}]\cdot\boldsymbol{\eta},
\end{aligned}\tag{A.11}$$

where we use the relation

$$\begin{aligned}
\nabla(\boldsymbol{\xi}\cdot\nabla p_0)&=(\nabla p_0\times\nabla)\times\boldsymbol{\xi}+\nabla p_0\nabla\cdot\boldsymbol{\xi}+\boldsymbol{\xi}\cdot\nabla\nabla p_0\\
&=\boldsymbol{B}_0\times((\boldsymbol{J}\cdot\nabla)\boldsymbol{\xi})-\boldsymbol{J}\times((\boldsymbol{B}_0\cdot\nabla)\boldsymbol{\xi})+\nabla p_0\nabla\cdot\boldsymbol{\xi}+\boldsymbol{\xi}\cdot\nabla\nabla p_0,
\end{aligned}\tag{A.12}$$

$$\boldsymbol{J}\times\boldsymbol{Q}=\boldsymbol{J}\times((\boldsymbol{B}_0\cdot\nabla)\boldsymbol{\xi})-(\boldsymbol{J}\times\boldsymbol{B}_0)(\nabla\cdot\boldsymbol{\xi})-\boldsymbol{\xi}\cdot\nabla(\boldsymbol{J}\times\boldsymbol{B}_0)-\boldsymbol{B}_0\times((\boldsymbol{\xi}\cdot\nabla)\boldsymbol{J}).\tag{A.13}$$

The relation

$$\begin{aligned} -\boldsymbol{\eta}\cdot[\boldsymbol{B}_0\times(\nabla\times(\boldsymbol{J}\times\boldsymbol{\xi}))] &= -(\boldsymbol{J}\times\boldsymbol{\xi})\cdot\nabla\times(\boldsymbol{\eta}\times\boldsymbol{B}_0)+\nabla\cdot[(\boldsymbol{\eta}\times\boldsymbol{B}_0)\times(\boldsymbol{J}\times\boldsymbol{\xi})] \\ &= -(\boldsymbol{J}\times\boldsymbol{\xi})\cdot\boldsymbol{R}+\nabla\cdot[(\boldsymbol{\eta}\times\boldsymbol{B}_0)\times(\boldsymbol{J}\times\boldsymbol{\xi})], \end{aligned} \tag{A.14}$$

transforms Eq. (A.11) as

$$\begin{aligned} [\nabla(\boldsymbol{\xi}\cdot\nabla p_0)+\boldsymbol{J}\times\boldsymbol{Q}]\cdot\boldsymbol{\eta} &= -(\boldsymbol{J}\times\boldsymbol{\xi})\cdot\boldsymbol{R}+\nabla\cdot[(\boldsymbol{\eta}\times\boldsymbol{B}_0)\times(\boldsymbol{J}\times\boldsymbol{\xi})]-(\boldsymbol{\eta}\cdot\nabla p_0)\nabla\cdot\boldsymbol{\xi} \\ &= [\nabla(\boldsymbol{\eta}\cdot\nabla p_0)+\boldsymbol{J}\times\boldsymbol{R}]\cdot\boldsymbol{\xi}+\nabla\cdot[((\boldsymbol{\xi}\times\boldsymbol{\eta})\cdot\boldsymbol{B}_0)\,\boldsymbol{J}]. \end{aligned} \tag{A.15}$$

By using Eq. (A.15), we can express as

$$\begin{aligned} dW_p(\boldsymbol{\xi},\boldsymbol{\eta})-dW_p(\boldsymbol{\eta},\boldsymbol{\xi}) &= \nabla\cdot[((\boldsymbol{\eta}\times\boldsymbol{\xi})\cdot\boldsymbol{B}_0)\boldsymbol{J}]+\nabla\cdot[(\boldsymbol{\eta}(\boldsymbol{\xi}\cdot\nabla p_0))-(\boldsymbol{\xi}(\boldsymbol{\eta}\cdot\nabla p_0))] \\ &= \nabla\cdot[((\boldsymbol{\eta}\times\boldsymbol{\xi})\cdot\boldsymbol{J})\boldsymbol{B}_0], \end{aligned} \tag{A.16}$$

and as the result,

$$\begin{aligned} W_{pv}(\boldsymbol{\xi},\boldsymbol{\eta})-W_{pv}(\boldsymbol{\eta},\boldsymbol{\xi}) &= \int\nabla\cdot[(\boldsymbol{\eta}\times\boldsymbol{\xi})\cdot\boldsymbol{J}]\,\boldsymbol{B}_0 dV \\ &= \int[(\boldsymbol{\eta}\times\boldsymbol{\xi})\cdot\boldsymbol{J}]\,(\boldsymbol{B}_0\cdot\boldsymbol{n})dS \\ &= 0, \end{aligned} \tag{A.17}$$

where the normal component of $\boldsymbol{B}_0$ vanishes on the plasma-vacuum surface. Thus with Eqs. (A.9) and (A.17), we prove the symmetric property of the operator $\boldsymbol{F}$ as Eq. (A.1).

Appendix B

One-dimensional Newcomb equation

In this appendix, we introduce the eigenvalue problem associated with the one-dimensional Newcomb equation by choosing the appropriate weight function and the natural boundary condition at a rational surface. With this procedure, the spectrum of the eigenvalue problem comprises real and denumerable eigenvalues. For simplicity, the fixed boundary condition, $\boldsymbol{\xi}(r) = 0$ at plasma surface, is assumed.

B.1 One-dimensional Newcomb equation

In an one-dimensional cylindrical coordinate system(r, θ, ϕ), a perturbation displacement is expressed as

$$\boldsymbol{\xi} = \bar{\boldsymbol{\xi}} \exp(\mathrm{i}m\theta - \mathrm{i}n\phi), \tag{B.1}$$

where m, n are the poloidal and the toroidal mode numbers, respectively. By taking the plasma minor radius a and the magnetic field at the magnetic axis B_0 as the normalized parameters, the potential energy integral W_p is written as

$$W_p(Y, Y) = \int_0^1 \mathcal{L} dx = \int_0^1 \left\{ f(x) \left| \frac{dY}{dx} \right|^2 + g(x) |Y|^2 \right\} dx, \tag{B.2}$$

$$f(x) = xF^2 \left(\frac{n}{m} - \frac{1}{q} \right)^2 \frac{m^2}{m^2 + n^2 \epsilon^2 x^2}, \tag{B.3}$$

$$g(x) = \frac{F^2}{x} \left[A + N + E + \left(\frac{n}{m} - \frac{1}{q} \right) M_1 + M_2 \right], \tag{B.4}$$

where $Y = r\bar{\boldsymbol{\xi}} \cdot \nabla r$, $x = r/a$, $\epsilon = a/R_0$, F is the normalized toroidal field, and A, N, E, M_1, M_2 in Eq. (B.4) are given as

$$A = \left(\frac{m}{q} - n\right)^2, \tag{B.5}$$

$$N = \left(\frac{2}{q}\right)^2 \frac{m^2}{m^2 + n^2\epsilon^2 x^2}, \tag{B.6}$$

$$E = \frac{2}{q^2 + \epsilon^2 x^2}\left\{\frac{x}{F^2}\frac{dp}{dx} - \left(2 - \frac{x}{q}\frac{dq}{dx}\right)\right\}, \tag{B.7}$$

$$M_1 = \frac{2}{q}\frac{m^2}{m^2 + n^2\epsilon^2 x^2}\left\{\frac{1}{q}\frac{dq}{dx} + \frac{2n^2\epsilon^2 x}{m^2 + n^2\epsilon^2 x^2} + \frac{1}{F^2}\frac{2q^2}{q^2 + \epsilon^2 x^2}\left[\frac{dp}{dx} + \left(\frac{\epsilon F x}{q}\right)^2\left(\frac{2}{x} - \frac{1}{q}\frac{dq}{dx}\right)\right]\right\}, \tag{B.8}$$

$$M_2 = \frac{2x}{q}\frac{d}{dx}\left(\frac{1}{q}\right)\frac{m^2}{m^2 + n^2\epsilon^2 x^2}. \tag{B.9}$$

The Euler-Lagrange equation obtained with Eq. (B.2) is written as

$$\frac{d}{dx}\left(f(x)\frac{dY}{dx}\right) - g(x)Y = 0. \tag{B.10}$$

We consider the eigenvalue problem associated with Eq. (B.10) as

$$\mathcal{N}Y \equiv \frac{d}{dx}\left(f(x)\frac{dY}{dx}\right) - g(x)Y = -\lambda\rho(x)Y, \tag{B.11}$$

where $\rho(x)$ is the weight function. When a plasma is marginally stable, the eigenvalue $\lambda = 0$.

B.2 Elimination of the singularity

Since the energy integral obtained by Eq. (B.11) is expressed as

$$W_p(Y, Y) = \lambda \int_0^1 \rho(x)|Y|^2 dx, \tag{B.12}$$

the sign of λ indicate the stability against the ideal MHD perturbation; when λ is negative (positive), a plasma is unstable (stable).

However, since the LHS of Eq. (B.10) can be Taylor expanded around rational surfaces $q(x_s) = m/n$ as

$$f(x) = w(x)\left(\frac{n}{m} - \frac{1}{q}\right)^2 = f_0 (x - x_s)^2 + f_1 (x - x_s)^3 + \cdots, \tag{B.13}$$

$$w(x) = F^2\frac{m^2 x}{m^2 + n^2\epsilon^2 x^2}, \tag{B.14}$$

$$g(x) = g_0 + g_1 (x - x_s) + \cdots, \tag{B.15}$$

where f_0, f_1, g_0, and g_1 are Taylor coefficients, and x_s is the location of a rational surface, $x = 0$ and x_s are obviously regular singular points of Eq. (B.10). To eliminate the singularity induced by the former singular point $x = 0$, the regularity condition has to be imposed at $x = 0$ as

$$Y = 0 \quad \text{at } x = 0. \tag{B.16}$$

The singularity at $x = x_s$, however, is more complicated, and is the cause that Eq. (B.11) has continuous spectra when $\rho(x = x_s) > 0$. In such cases, the eigenvalue corresponding to the marginally stable state cannot be numerically singled out among these continua.

When a plasma is marginally stable, Eq. (B.10) has a nontrivial solution which is square integrable and satisfies the fixed boundary conditions $Y(0) = Y(1) = 0$. Since $q(x_s) = m/n$ is a regular singular point, the region [0,1] can be separated into the left side region $[0,x_s)$ and the right side region $(x_s,1]$ [28], and two fundamental solutions of Eq. (B.10) can be expressed by the Frobenius series around $q(x_s)$ as

$$Y = (t_p)^{-1/2+\mu_{suy}} \left(1 + \sum_{j=1}^{\infty} Y_j \left(\frac{m}{q} - n \right)^j \right), \quad p = L, R, \tag{B.17}$$

where

$$t_L \equiv |x - x_s|_L = \begin{cases} (x_s - x) & \text{for } x < x_s, \\ 0 & \text{for } x > x_s, \end{cases} \tag{B.18}$$

$$t_R \equiv |x - x_s|_R = \begin{cases} 0 & \text{for } x < x_s, \\ (x - x_s) & \text{for } x > x_s. \end{cases} \tag{B.19}$$

Here the Suydam index μ_{suy} is

$$\mu_{suy} = \sqrt{\frac{1}{4} + \frac{g_0}{f_0}}, \tag{B.20}$$

and we assume that the Suydam stability condition

$$\frac{1}{4} + \frac{g_0}{f_0} > 0, \tag{B.21}$$

is satisfied. Since the square integrable solution given by Eq. (B.17) is only the solution with the power $-1/2 + \mu_{suy}$, called the "small solution", $\rho(x)$ is chosen in Eq. (B.11) that all eigenfunctions behave as the small solution near $x = x_s$, and the proper boundary condition is imposed at $x = x_s$. For this purpose, we introduce first $\rho(x)$ as

$$\rho(x) = F^2 \left(\frac{m}{q} - n \right)^2, \tag{B.22}$$

and the boundary condition at $x = x_s$ is obtained as follows. The bilinear form corresponding to Eq. (B.2) is given by

$$W(\eta, \xi) = \int_0^1 \left(f \frac{d\eta^*}{dx} \frac{d\xi^*}{dx} + g\eta^* \xi \right) dx, \tag{B.23}$$

where the script $*$ denotes the complex conjugate, and the bilinear concomitant is given by

$$\eta^* \mathcal{N}\xi - \xi(\mathcal{N}\eta)^* = \frac{d}{dx}\left(f(x)\left(\eta^* \frac{d\xi}{dx} - \xi\frac{d\eta^*}{dx}\right)\right). \tag{B.24}$$

The boundary condition for ξ and η at $x = x_s$ is obtained from Eq. (B.24) to make the operator $\mathcal{N}$ self-adjoint. Since the singularity of ξ and η is at most $|x - x_s|^{-1/2+\mu_{suy}}$, we get the relations

$$\lim_{x\to x_s} f(x)\eta^* \frac{d\xi}{dx} = 0, \tag{B.25}$$

and

$$\int_0^1 \eta^* \mathcal{N}\xi dx = \int_0^1 \mathcal{N}\eta\xi dx. \tag{B.26}$$

Equation (B.26) means that the operator $\mathcal{N}$ is self-adjoint without boundary conditions for ξ and η. Thus the natural boundary condition for ξ should be imposed at $x = x_s$.

By choosing $\rho(x)$ and the natural boundary condition at rational surfaces $x = x_s$, all eigenfunctions behave as the small solution near the point $x = x_s$, and the spectrum of Eq. (B.11) comprises real and denumerable eigenvalues. This means that we can obtain numerically not only negative discrete eigenvalues but also positive ones, and identify the marginally stable condition of a plasma against the ideal MHD motion.

Appendix C

Green's function technique for calculating the vacuum energy contribution

In this appendix, we introduce the numerical method for calculating the vacuum energy contribution with a Green's function technique. The wall surrounding the plasma and the vacuum is assumed as the perfect conducting wall.

C.1 Basic equation

In the straight field line coordinate (ψ, θ, ϕ), the Jacobian $\sqrt{g(\psi,\theta)}$ is expressed as

$$\sqrt{g(\psi,\theta)} = \frac{1}{(\nabla\phi \cdot (\nabla\psi \times \nabla\theta))} = \frac{1}{(\boldsymbol{B}_0 \cdot \nabla\theta)}, \tag{C.1}$$

where ψ is the poloidal magnetic flux function defined in Eq. (2.12),θ and ϕ are the poloidal and toroidal angle, $\boldsymbol{B}$ is the magnetic field in the cylindrical coordinate system (R, ϕ, Z) as

$$\boldsymbol{B} = \nabla\phi \times \nabla\psi + F(\psi)\nabla\phi, \tag{C.2}$$

and $F(\psi)$ is the toroidal field function; these are same as those defined in Section 2.2. With the safety factor $q(\psi)$

$$q(\psi) = \frac{\boldsymbol{B} \cdot \nabla\phi}{\boldsymbol{B} \cdot \nabla\theta}, \tag{C.3}$$

$\sqrt{g(\psi,\theta)}$ is transformed as

$$\sqrt{g(\psi,\theta)} = \frac{q(\psi)}{F} R^2. \tag{C.4}$$

By expressing the perturbed magnetic field in the vacuum region $\acute{\boldsymbol{Q}}$ with the scalar potential Φ as

$$\acute{\boldsymbol{Q}} = \nabla\Phi, \tag{C.5}$$

the potential energy integral in the vacuum reads

$$W_V = \frac{1}{2}\int_V |\nabla\Phi|^2\, dV, \tag{C.6}$$

where dV is the volume element. We introduce the boundary condition forΦ on the perfect conducting wall as

$$\nabla\Phi \cdot \boldsymbol{n}_w = 0, \tag{C.7}$$

and that on the plasma surface as

$$\boldsymbol{Q} \cdot \nabla\psi|_a = \nabla\Phi \cdot \nabla\psi|_a, \tag{C.8}$$

where $\boldsymbol{n}_w$ is the unit normal to the wall surface, $\boldsymbol{Q}$ is the perturbed magnetic field in the plasma, and $X|_a$ means the value of X at the plasma surface. Since$\boldsymbol{Q}$ can be written with the plasma displacement$\boldsymbol{\xi}$ as

$$\boldsymbol{Q} = \nabla \times (\boldsymbol{\xi} \times \boldsymbol{B}), \tag{C.9}$$

which is same as that in Section 2.3,$\boldsymbol{Q} \cdot \nabla\psi$ can be written as

$$\boldsymbol{Q} \cdot \nabla\psi = \frac{F}{\sqrt{g}}\mathcal{D}_\theta(\hat{\xi}), \tag{C.10}$$

where

$$\hat{\xi} = \frac{q}{F}\boldsymbol{\xi} \cdot \nabla\psi, \tag{C.11}$$

and the operator $\mathcal{D}_\theta(X)$ for the perturbation $X(\psi, \theta, \phi) \propto \exp(-\mathrm{i}n\phi)$ is

$$\mathcal{D}_\theta(X) = \frac{1}{q}\frac{\partial X}{\partial\theta} - \mathrm{i}nX. \tag{C.12}$$

By substituting Eq. (C.10) into Eq. (C.8), we obtain

$$\frac{F}{\sqrt{g}}\mathcal{D}_\theta = \frac{\partial\Phi}{\partial\boldsymbol{n}}\,|\nabla\Phi|_a\,. \tag{C.13}$$

The scalar potentialΦ satisfies the Laplace equation

$$\nabla^2\Phi = 0. \tag{C.14}$$

With the vector identity

$$|\nabla\Phi|^2 = \nabla \cdot (\Phi\nabla\Phi) - \Phi\nabla^2\Phi, \tag{C.15}$$

W_V is transformed as

$$W_V = \frac{1}{2}\int_a \Phi\nabla\Phi \cdot \boldsymbol{n}dS, \tag{C.16}$$

where $\int_a$ is the surface integral on the plasma surface. SinceΦ can be expressed by using the real and symmetric kernel of integral $Q(\theta, \theta')$ as

$$\Phi(\theta) = \int_0^{2\pi} Q(\theta, \theta')N(\theta')d\theta', \tag{C.17}$$

$$N(\theta') = [F\mathcal{D}_\theta(\hat{\xi})](\theta'), \tag{C.18}$$

Eq. (C.15) reads

$$W_V = \pi \int_0^{2\pi} d\theta \int_0^{2\pi} d\theta' Q(\theta, \theta') N(\theta) N(\theta'). \tag{C.19}$$

By transforming from Eq. (C.6) to Eq. (C.19), W_V is calculated with the kernel of integral $Q(\theta, \theta')$.

C.2 Integral equation

We introduce a Green's theorem

$$\int (u\nabla^2 v - v\nabla^2 u) dV = \int \left(u \frac{\partial v}{\partial \boldsymbol{n}} - v \frac{\partial u}{\partial \boldsymbol{n}} \right) dS, \tag{C.20}$$

and a Green's function satisfying

$$\nabla^2 G(\boldsymbol{x}, \boldsymbol{x}') = \delta(\boldsymbol{x} - \boldsymbol{x}'). \tag{C.21}$$

Here in Eq. (C.20), u and v are arbitrary scalar functions, and in Eq. (C.21), $\delta(\boldsymbol{x} - \boldsymbol{x}')$ is a Dirac's delta function, $\boldsymbol{x}$ and $\boldsymbol{x}'$ are the integration variable and a point on the boundary surfaces. By substituting $u = \Phi$ and $v = G(\boldsymbol{x}, \boldsymbol{x}')$ into Eq. (C.20), we obtain

$$\begin{aligned} \Phi(\boldsymbol{x}) = & \frac{1}{2\pi} \int_a \left(\Phi(\boldsymbol{x}') \frac{\partial G(\boldsymbol{x}, \boldsymbol{x}')}{\partial \boldsymbol{n}} - G(\boldsymbol{x}, \boldsymbol{x}') \frac{\partial \Phi(\boldsymbol{x}')}{\partial \boldsymbol{n}} \right) dS' \\ & - \frac{1}{2\pi} \int_b \left(\Phi(\boldsymbol{x}') \frac{\partial G(\boldsymbol{x}, \boldsymbol{x}')}{\partial \boldsymbol{n}} \right) dS', \end{aligned} \tag{C.22}$$

where $\int_b$ expresses the surface integral on the wall. A Green's function of Eq. (C.14) is

$$G(\boldsymbol{x}, \boldsymbol{x}') = \frac{1}{|\boldsymbol{x} - \boldsymbol{x}'|}, \tag{C.23}$$

and the identities for $G(\boldsymbol{x}, \boldsymbol{x}')$ can be obtained as

$$\int_a \frac{\partial}{\partial \boldsymbol{n}'} G(\boldsymbol{x}, \boldsymbol{x}'_a) dS' = \begin{cases} -2\pi & \text{for } \boldsymbol{x} = \boldsymbol{x}_a, \\ 0 & \text{for } \boldsymbol{x} = \boldsymbol{x}_b, \end{cases} \tag{C.24}$$

$$\int_b \frac{\partial}{\partial \boldsymbol{n}'} G(\boldsymbol{x}, \boldsymbol{x}'_b) dS' = \begin{cases} -4\pi & \text{for } \boldsymbol{x} = \boldsymbol{x}_a, \\ -2\pi & \text{for } \boldsymbol{x} = \boldsymbol{x}_b, \end{cases} \tag{C.25}$$

where $\partial / \partial \boldsymbol{n}'$ is the normal derivative relating the argument with prime (). With Eqs. (C.24) and (C.25), Eq. (C.22) is transformed as

$$\begin{aligned} 2\Phi(\boldsymbol{x}_a) = & \frac{1}{2\pi} \left\{ \int_a [\Phi(\boldsymbol{x}'_a) - \Phi(\boldsymbol{x}_a)] \frac{\partial}{\partial \boldsymbol{n}'} G(\boldsymbol{x}_a, \boldsymbol{x}'_a) dS' \right. \\ & \left. - \int_a G(\boldsymbol{x}_a, \boldsymbol{x}'_a) \frac{\partial}{\partial \boldsymbol{n}'} \Phi(\boldsymbol{x}'_a) dS' - \int_b \Phi(\boldsymbol{x}'_b) \frac{\partial}{\partial \boldsymbol{n}'} G(\boldsymbol{x}_a, \boldsymbol{x}'_b) dS' \right\}, \end{aligned} \tag{C.26}$$

$$\begin{aligned} 0 = & \frac{1}{2\pi} \left\{ \int_a \Phi(\boldsymbol{x}'_a) \frac{\partial}{\partial \boldsymbol{n}'} G(\boldsymbol{x}_b, \boldsymbol{x}'_a) dS' - \int_a G(\boldsymbol{x}_b, \boldsymbol{x}'_a) \frac{\partial}{\partial \boldsymbol{n}'} \Phi(\boldsymbol{x}'_a) dS' \right. \\ & \left. - \int_b [\Phi(\boldsymbol{x}'_b) - \Phi(\boldsymbol{x}_b)] \frac{\partial}{\partial \boldsymbol{n}'} G(\boldsymbol{x}_b, \boldsymbol{x}'_b) dS' \right\}. \end{aligned} \tag{C.27}$$

This transformation is essential to remove the singularities when $\boldsymbol{x}'_a = \boldsymbol{x}_a$ and $\boldsymbol{x}'_b = \boldsymbol{x}_b$, and these singularities are treated in Section C.4.

C.3 Definition of the poloidal angle on the wall

We express the shape of the conducting wall as $((R_W)_j, (Z_W)_j)$ with $2K + 1$ numbers of point, where

$$(R_W)_{2K+1} = (R_W)_1, \quad (Z_W)_{2K+1} = (Z_W)_1. \tag{C.28}$$

By introducing the discrete point η_j as

$$\eta_j = \pi \frac{j-1}{K}, \quad j = 1, \cdots, 2K+1, \tag{C.29}$$

$(R_W)_j$ and $(Z_W)_j$ can be treated as the function of η_j, $R_W(\eta_j) = (R_W)_j$ and $Z_W(\eta_j) = (Z_W)_j$, where $\eta \in [0, 2\pi]$. The location on the wall is specified by (η, ϕ), and the outward normal derivative of the scalar function $f(\eta, \phi)$ on the wall is

$$\frac{\partial f}{\partial \boldsymbol{n}} dS = R_W \left[\frac{\partial Z_W}{\partial \eta} \frac{\partial f}{\partial R_W} - \frac{\partial R_W}{\partial \eta} \frac{\partial f}{\partial Z_W} \right] d\eta d\phi, \tag{C.30}$$

where dS is the area element on the wall. The outer normal derivative on the plasma surface can be obtained by changing from η to θ. By using Eq. (C.30), Eqs. (C.23) and (C.24) are rewritten as

$$\begin{aligned} 2\Phi_a(\theta) = \frac{1}{2\pi} \Bigg\{ & \int_0^{2\pi} d\theta' R'(\theta') \left[\Phi_a(\theta') DG^n(\theta, \theta') - \Phi_a(\theta) DG^0(\theta, \theta') \right] \\ & - \int_0^{2\pi} d\theta' N(\theta') G^n(\theta, \theta') - \int_0^{2\pi} d\eta' R'(\eta') \Phi_b(\eta') DG^n(\theta, \eta') \Bigg\}, \end{aligned} \tag{C.31}$$

$$\begin{aligned} 0 = \frac{1}{2\pi} \Bigg\{ & \int_0^{2\pi} d\theta' R'(\theta') \Phi_a(\theta') DG^n(\eta, \theta') - \int_0^{2\pi} d\theta' N(\theta') G^n(\eta, \theta') \\ & - \int_0^{2\pi} d\eta' R'(\eta') \left[\Phi_b(\eta') DG^n(\eta, \eta') - \Phi_b(\eta) DG^0(\eta, \eta') \right] \Bigg\}. \end{aligned} \tag{C.32}$$

Here $\Phi_a(\theta)$ and $\Phi_b(\eta)$ are the scalar potential on the plasma surface and that on the wall, respectively, and

$$G^n(\boldsymbol{x}, \boldsymbol{x}') = \int_0^{2\pi} \frac{\exp(-in(\phi - \phi'))}{|\boldsymbol{x} - \boldsymbol{x}'|} d\phi, \tag{C.33}$$

$$DG^n(\alpha, \beta') = \left[\frac{\partial Z'}{\partial \beta'} \frac{\partial}{\partial R'} - \frac{\partial R'}{\partial \beta'} \frac{\partial}{\partial Z'} \right] G^n(\boldsymbol{x}(\alpha), \boldsymbol{x}'(\beta')), \tag{C.34}$$

where α, β are θ or η, and

$$\boldsymbol{x} = (R, Z, \phi), \quad \boldsymbol{x}' = (R', Z', \phi'). \tag{C.35}$$

C.4 Elimination of the singularity

By introducing the modified elliptic integral K^n

$$K^n(\zeta) = \int_0^{\pi/2} \frac{\cos(2n\phi)}{[1-(1-\zeta)\sin^2\phi]^{1/2}} d\phi, \tag{C.36}$$

$$\zeta = \frac{(R'-R)^2 + (Z'-Z)^2}{(R'+R)^2 + (Z'-Z)^2}, \tag{C.37}$$

$G^n(\boldsymbol{x}, \boldsymbol{x}')$ can be written as

$$G^n(\boldsymbol{x}, \boldsymbol{x}') = \frac{4K^n(\zeta) \times (-1)^n}{[(R'+R)^2 + (Z'-Z)^2]^{1/2}}. \tag{C.38}$$

The integral K^n as well as its derivative $dK^n/d\zeta$ exhibit singularities at $\zeta = 0$ as

$$K^n(\zeta) = (-1)^{n+1} \frac{\ln \zeta}{2} + \cdots, \tag{C.39}$$

$$\frac{dK^n(\zeta)}{d\zeta} = (-1)^{n+1} \frac{1}{2\zeta} + \cdots. \tag{C.40}$$

From these equations, all the integrals containing DG^n in Eqs. (C.31) and (C.32) are now regular. The integrals including G, however, still show logarithmic singularities, and we cannot treat these integrals numerically. To avoid such singularities, $\hat{G}^n(\theta, \theta')$ is rewritten as

$$G^n(\theta, \theta') = G_{reg} + G_{anal}, \tag{C.41}$$

$$G_{reg} = G^n(\theta, \theta') + \frac{2}{R(\theta)} \log|\theta' - \theta|, \tag{C.42}$$

$$G_{anal} = -\frac{2}{R(\theta)} \log|\theta' - \theta|, \tag{C.43}$$

where the integrals containing G_{reg} are regular integrals. Since the singular part in Eq. (C.41), G_{anal}, can be treated analytically as

$$\int_{\theta_j}^{\theta_{j+1}} d\theta \int_{\theta_j}^{\theta_{j+1}} d\theta' \log|\theta' - \theta| = h^2 \log h - \frac{3}{2}h^2, \tag{C.44}$$

$$h \equiv |\theta_{j+1} - \theta_j|, \tag{C.45}$$

we can integrate numerically Eqs. (C.31) and (C.32).

C.5 Vacuum energy matrix

We divide the poloidal angle on the plasma surface, θ, and that on the wall, η, by $N+1$ and $M+1$ as

$$\theta_1 = \eta_1 = 0, \quad \theta_{N+1} = \eta_{M+1} = 2\pi. \tag{C.46}$$

With the step function introduced as ($\zeta = \theta$ or η)

$$e^{j+1/2}(\zeta) = \begin{cases} 1 & \text{for } \zeta \in [\zeta_j, \zeta_{j+1}], \\ 0 & \text{for } \zeta \notin [\zeta_j, \zeta_{j+1}], \end{cases} \tag{C.47}$$

the potentials are expanded as

$$\Phi_a(\theta) = \sum_{j=1}^{N} b_j e^{j+1/2}(\theta), \tag{C.48}$$

$$\Phi_b(\eta) = \sum_{k=1}^{M} c_k e^{k+1/2}(\eta). \tag{C.49}$$

By substituting Eq. (C.48) into Eq. (C.31), multiplying $e^{j+1/2}(\theta)$, and integrating from 0 to 2π, we obtain the linear equation

$$2\boldsymbol{b} = \mathbf{A} \cdot \boldsymbol{b} - \mathbf{C} \cdot \boldsymbol{c} - \mathbf{B} \cdot \boldsymbol{a}. \tag{C.50}$$

Here $\boldsymbol{b}$ and $\boldsymbol{c}$ are the vectors constructed with the coefficients in Eqs. (C.48) and (C.49) as

$$\boldsymbol{b} = (b_1, \cdots, b_N)^t, \quad \boldsymbol{c} = (c_1, \cdots, c_N)^t, \tag{C.51}$$

$\boldsymbol{a}$ is written as

$$\boldsymbol{a} = (a_1, \cdots, a_N)^t, \tag{C.52}$$

$$a_j = N(\theta_{j+1/2}), \quad \theta_{j+1/2} = \frac{\theta_j + \theta_{j+1}}{2}, \quad j = 1, \cdots, N, \tag{C.53}$$

and the matrices $\mathbf{A}$, $\mathbf{B}$, and $\mathbf{C}$ are given by

$$A_{j,k} = R_a^{k+1/2} \mathcal{G}^n_{a,a'}(j,k) - \delta_{j,k} \sum_{m=1}^{N} R_a^{m+1/2} \mathcal{G}^0_{a,a'}(j,m), \tag{C.54}$$

$$B_{j,k} = \mathcal{S}_{a,a'}(j,k), \tag{C.55}$$

$$C_{j,k} = R_b^{k+1/2} \mathcal{G}^n_{a,b'}(j,k), \tag{C.56}$$

$$\mathcal{G}^n_{\alpha,\beta'}(j,k) = \frac{1}{2\pi(\alpha_{j+1} - \alpha_j)} \int_{\alpha_j}^{\alpha_{j+1}} d\alpha \int_{\beta_k}^{\beta_{k+1}} d\beta' DG^n(\alpha, \beta'), \tag{C.57}$$

$$\mathcal{S}_{\alpha,a'}(j,k) = \frac{1}{2\pi(\alpha_{j+1} - \alpha_j)} \int_{\alpha_j}^{\alpha_{j+1}} d\alpha \int_{\theta_k}^{\theta_{k+1}} d\theta' G^n(\alpha, \theta'), \tag{C.58}$$

where we substitute $\alpha = \theta$ (or η) in the RHS of Eqs. (C.57) and (C.58) when $\alpha = a$ (or b) in the LHS, $\delta_{j,k}$ is a Kronecker's δ symbol

$$\delta_{j,k} = \begin{cases} 1 & \text{for } j = k, \\ 0 & \text{for } j \neq k, \end{cases} \tag{C.59}$$

and

$$R_a^{k+1/2} = R(\theta_{k+1/2}), \quad R_b^{k+1/2} = R(\eta_{k+1/2}). \tag{C.60}$$

To do likewise for Eq. (C.32), we also obtain the equation

$$0 = \mathbf{D} \cdot \boldsymbol{b} - \mathbf{F} \cdot \boldsymbol{c} - \mathbf{E} \cdot \boldsymbol{a}, \tag{C.61}$$

where

$$D_{j,k} = R_a^{k+1/2} \mathcal{G}_{b,a'}^n(j,k), \tag{C.62}$$

$$E_{j,k} = \mathcal{S}_{b,a'}(j,k), \tag{C.63}$$

$$F_{j,k} = R_b^{k+1/2} \mathcal{G}_{b,b'}^n(j,k) - \delta_{j,k} \sum_{m=1}^{M} R_b^{m+1/2} \mathcal{G}_{b,b'}^0(j,m). \tag{C.64}$$

By solving Eqs. (C.50) and (C.61) for $\boldsymbol{b}$, we obtain

$$\boldsymbol{b} = \mathbf{Q} \cdot \boldsymbol{a}, \tag{C.65}$$

where the $N \times N$ real matrix $\mathbf{Q}$ is the approximated matrix of the kernel of integral in Eq. (C.19) and is expressed as

$$\mathbf{Q} = (2\mathbf{I} - \mathbf{A} + \mathbf{C}\mathbf{F}^{-1}\mathbf{D})^{-1}(\mathbf{C}\mathbf{F}^{-1}\mathbf{E} - \mathbf{B}), \tag{C.66}$$

and $\mathbf{I}$ is the unit matrix.

With the matrix $\mathbf{Q}$, we obtain W_V in Eq. (C.19) as a quadratic form

$$W_V = \pi \sum_{j,k=1}^{N} (\theta_{j+1} - \theta_j)(\theta_{k+1} - \theta_k) N_{k+1/2} Q_{j,k} N_{j+1/2} \tag{C.67}$$

$$= \left\langle \boldsymbol{a} \left| \hat{\mathbf{Q}} \right| \boldsymbol{a} \right\rangle, \tag{C.68}$$

$$\hat{Q}_{j,k} = \pi(\theta_{j+1} - \theta_j)(\theta_{k+1} - \theta_k) Q_{j,k}. \tag{C.69}$$

Bibliography

[1] K. Miyamoto, *Plasma Physics for Nuclear Fusion* (MIT Press, Cambridge, 1980) Chap. 16.

[2] N. J. Peacock *et al.*, Nature **224**, 488 (1969).

[3] T. Fujita *et al.*, Nucl. Fusion **39**, 1627 (1999).

[4] V. A. Chuyanov, Nucl. Fusion **40**, 495 (2000).

[5] D. Pfirsch and H. Tasso, Nucl. Fusion **11**, 259 (1971).

[6] A. Bondeson and D. J. Ward, Phys. Rev. Lett. **72**, 2709 (1994).

[7] D. J. Ward and A. Bondeson, Phys. Plasmas **2**, 1570 (1995).

[8] M. S. Chu *et al.*, Phys. Plasmas **2**, 2236 (1995).

[9] R. Fitzpatrick and A. Y. Aydemir, Nucl. Fusion **36**, 11 (1996).

[10] A. H. Boozer, Phys. Plasmas **5**, 3350 (1998).

[11] J. Bialek, A. H. Boozer, M. E. Mauel and G. A. Navratil, Phys. Plasmas **8**, 2170 (2001).

[12] M. S. Chance, M. S. Chu, M. Okabayashi and A. D. Turnbull, Nucl. Fusion **42**, 295 (2002).

[13] M. S. Chu, M. S. Chance, A. H. Glasser and M. Okabayashi, Nucl. Fusion **43**, 441 (2003).

[14] A. M. Garofalo *et al.*, Nucl. Fusion **40**, 1491 (2000).

[15] M. Okabayashi *et al.*, Phys. Plasmas **8**, 2071 (2001).

[16] A. H. Glasser and M. S. Chance, Bull. Am. Phys. Soc. **42**, 1848 (1997).

[17] M. S. Chance, Phys. Plasmas **4**, 2161 (1997).

[18] D. Lortz, Nucl. Fusion **18**, 97 (1978).

[19] J. W. Connor, R. J. Hastie, H. R. Wilson and R. L. Miller, Phys. Plasmas **5**, 2687 (1998).

[20] F. Wagner *et al.*, Phys. Rev. Lett. **49**, 1408 (1982).

[21] H. R. Wilson *et al.*, Phys. Plasmas **6**, 1925 (1999).

[22] H. R. Wilson, P. B. Snyder, G. T. A. Huysmans and R. L. Miller, Phys. Plasmas **9**, 1277 (2002).

[23] P. B. Snyder *et al.*, Phys. Plasmas **9**, 2037 (2002).

[24] A. B. Mikhailovskii, G. T. A. Huysmans, S. E. Sharapov and W. Kerner, Plasma Phys. Rep. **23**, 844 (1997).

[25] G. T. A. Huysmans, S. E. Sharapov, A. B. Mikhailovskii and W. Kerner, Phys. Plasmas **8**, 4292 (2001).

[26] T. Onjun *et. al.*, Phys. Plasmas **11**, 3006 (2004).

[27] W. A. Newcomb, Ann. Phys. **10**, 232 (1960).

[28] A. Pletzer and R. L. Dewar, J. Plasma Phys. **45**, 427 (1991).

[29] S. Tokuda and T. Watanabe, Phys. Plasmas **6**, 3012 (1999).

[30] S. Tokuda and T. Watanabe, J. Plasma Fusion Res. **73**, 1141 (1997).

[31] N. Aiba, S. Tokuda, T. Ishizawa and M. Okamoto, Plasma Phys. Control. Fusion **46**, 1699 (2004).

[32] R. Gruber *et al.*, Comput. Phys. Commun. **21**, 323 (1981).

[33] O. P. Pogutse and E. I. Yurchenko, *Reviews of Plasma Physics (Ed. Leontovich M A)* (Consultants Bureau, New York, 1986) Vol. 11, Chap. 2.

[34] N. Aiba, S. Tokuda, T. Ishizawa and M. Okamoto, J. Plasma Fusion Res. Series **6**, (2004, to be published).

[35] R. Gruber *et al.*, Comput. Phys. Commun. **24**, 363 (1981).

[36] W. Gropp, E. Lusk and A. Skjellum, *Using MPI second edition* (MIT Press, Cambridge, 1999).

[37] L. S. Blackford *et al.*, *ScaLAPACK Users' Guide* (SIAM, Philadelphia, 1996).

[38] Yu. L. Klimontovich, *The Statistical Theory of Non-equilibrium Processes in a Plasma* (MIT, Cambridge, 1967).

[39] J. D. Jackson, *Classical Electrodynamics third edition* (Wiley, New York, 1999).

[40] A. A. Vlasov, J. Phys. (USSR)**9**, 25 (1945).

[41] D. R. Nicholson, *Introduction to Plasma Theory*(Wiley, New York, 1983).

[42] J. P. Freidberg, *Ideal Magnetohydrodynamics*(Plenum Press, New York, 1987).

[43] H. Grad and H. Rubin, "Hydromagnetic Equilibria and Force-free Fields", in*United Nations Conference on the Peaceful Uses of Atomic Energy, Geneva, 1958*Vol. 31, p. 190.

[44] V. D. Shafranov, Sov. Phys. JETP**6**, 545 (1958).

[45] R. Lüst and A. Shulüter, Z. Naturforsch.**129**, 850 (1957).

[46] L. S. Solovev and V. D. Shafranov, *Reviews of Plasma Physics (Ed. Leontovich M A)*(Consultants Bureau, New York, 1966) Vol. 5, Chap. 1.

[47] S. P. Hirshman, Phys. Fluids**21**, 1295 (1978).

[48] T. Takeda and S. Tokuda, J. Comput. Phys.**93**, 1 (1991).

[49] F. L. Hinton and R. D. Hazeltine, Rev. Mod. Phys.**48**, 239 (1976).

[50] S. P. Hirshman and D. J. Sigmar, Nucl. Fusion**21**, 1079 (1981).

[51] F. Troyon, R. Gruber, H. Saurenmann, S. Semenzato and S. Succi, Plasma Phys. Control. Fusion **26**, 209 (1984).

[52] I. B. Bernstein, E. A. Frieman, M. D. Kruskal and R. M. Kulsrud, Proc. Roy. Soc.**A244**, 17 (1958).

[53] J. P. Goedbloed and S. Poedts, *Principles of Magnetohydrodynamics*, (Cambridge, New York, 2004).

[54] A. E. Lifschitz, *Magnetohydrodynamics and Spectral Theory*(Kluwer, Dordrecht, 1989).

[55] R. A. Horn and C. R. Johnson, *Matrix Analysis*(Cambridge University Press, Cambridge, 1985).

[56] M. N. Bussac, R. Pellat, D. Edery and J. L. Soule, Phys. Rev. Lett.**35**, 1638 (1975).

[57] R. C. Grimm, R. L. Dewar and J. Manickam, J. Comput. Phys.**49**, 94 (1983).

[58] R. L. Dewar and A. Pletzer, J. Plasma Phys.**43**, 291 (1990).

[59] J. W. Connor *et al.*, Phys. Fluids **31**, 577 (1988).

[60] C. M. Bender and S. A. Orszag, *Advanced Mathematical Methods for Scientists and Engineers* (McGraw-Hill, New York, 1978) pp.61.

[61] O. C. Zienkiewicz and R. L. Taylor, *The Finite Element Method fourth edition* (McGraw-Hill, New York, 1991) Vol. 1.

[62] W. H. Press, B. P. Flannery, S. A. Teukolsky and W. T. Vetterling, *Numerical Recipes* (Cambridge, New York, 1986).

[63] R. Courant and D. Hilbert, *Methods of Mathematical Physics* (Interscience, New York, 1953) Vol. 1.

[64] F. Troyon, L. C. Bernard and R. Gruber, Comput. Phys. Commun. **19**, 161 (1980).

[65] V. D. Shafranov, Sov. Phys. - Tech. Phys. **15**, 175 (1970).

[66] R. Gruber, F. Troyon and T. Tsunematsu, Plasma Phys. **25**, 207 (1983).

[67] J. W. Connor, R. J. Hastie and J. B. Taylor, Phys. Rev. Lett. **40**, 396 (1978).

[68] V. D. Shafranov, *Reviews of Plasma Physics (Ed. Leontovich M A)* (Consultants Bureau, New York, 1966) Vol. 2, Chap. 2.

[69] Y. Idomura, M. Adachi, K. Gorai, Y. Suzuki and X. Wang, J. Plasma Fusion Res. **79**, 172 (2003).